International Relativistic Astrophysics PhD
IRAP Ph.D.

Relativistic plasma and transparency in Gamma-Ray Bursts and equilibrium self-gravitating systems of fermions

Thesis Advisor
Dr. Gregory Vereshchagin

Ph.D. Student
Ivan Siutsou

Academic Year 2009–2013

Contents

Abbreviations

GRB	Gamma-ray burst
P-GRB	Proper GRB
DM	Dark matter
WIMP	Weakly interacting massive particle
CMB	Cosmic microwave background
GR	General relativity
QED	Quantum electrodynamics
RHS	Right hand side
PhE	Photospheric Equitemporal Surface

Introduction

Gamma-ray bursts (GRB) are flashes of electromagnetic radiation observed at an average rate of a few per day throughout the Universe, up to redshifts of 9 [1]. Their maximum luminosity can surpass the luminosity of all the visible objects in the Universe, they are the brightest sources of electromagnetic radiation known so far. Until 1997 they were detected only in gamma-rays with poor angular resolution and there was no direct information about the distance from them and the energy involved. From early 1997 the Beppo-SAX satellite started to detect theoretically predicted X-ray afterglows of GRBs. These X-ray measurements yielded positions of GRBs on the sky sufficiently accurate to allow the follow up by large ground-based optical telescopes. These latter observations identified host galaxies of GRBs thus proving their cosmological origin. The energy output estimated assuming isotropic energy release was found to range from 10^{48} up to 10^{54} ergs. The duration of GRBs ranges from milliseconds up to thousands of seconds.

The only known source of such large energy released on such a short time scale is the gravitational energy. A theorem [2] shows that both Coulomb and rotational energy of a black hole are in principle extractable, giving respectively up to 50% and up to 29% of the total mass-energy. As simulations show, large amount of gravitational energy (of the order of a solar rest mass) can be released in a very short time (seconds or less) in a very small region (tens of kilometers or so) by a core collapse of a massive star or by a merger of two compact objects, e.g. neutron stars and/or black holes [3–5].

The gravitational energy, released in the source of GRB, must be ultimately converted into electromagnetic energy detected by distant observer. The electromagnetic model of GRBs [6] assumes that the energy in the source of GRB is converted first into the energy of electromagnetic field, which is transported out of the source in the form of a Poynting flux. Only later this energy is dissipated in the form of electromagnetic radiation. Most of proposed models, however, focus

on another possibility. Within the fireball model ([7, 8] and references therein) and the fireshell model ([9] and references therein) it is assumed that the energy in the source of the GRB is converted into relativistic optically thick plasma. Such plasma expands driven by radiative pressure until it becomes transparent to photons transported together with the plasma. The first electromagnetic signal from GRBs is expected to come from this transparency event. The spectrum characterizing emission from transparency is expected in the literature to be nearly black body [10–13]. Pure black body spectra were never found in GRBs. Within the fireball model the observed nonthermal spectra are assumed to originate from relativistic shocks [7]. Within the fireshell model such nonthermal spectra are assumed to originate as a result of convolution over Equitemporal Surfaces [14] and integration over time [5]. However, the transparency emission, referred to as the Proper GRB, remain a key ingredient of the fireshell model. Both its energy and time separation from the extended afterglow peak emission are predicted and tested with observations [5].

Recent observations with unprecedented spectrum and time resolution by *Fermi Gamma-ray Space Telescope satellite* indicate that subdominant thermal component is present in many, if not all observed GRB spectra, see e.g. [15–19]. In the literature such thermal component is accounted for by the so-called photospheric models [12, 20–26]. All these works based essentially on the steady wind model of Paczynski [27] show that observed spectrum of the photospheric emission is broader than the Planck function. However, the relativistic outflows expected to originate from energy release in GRB sources are by definition finite in time and in space. These finiteness effects were never studied in the literature, except the work [23] where the switching off relativistic wind was considered. Before considering the theory of photospheric emission from relativistic outflows, which is the central topic of this thesis, in Chapter 1 we consider relativistic degeneracy of electron-positron-photon plasma.

Observations indicate that plasma in the sources of GRBs is relativistic, i.e. average energy per particle is comparable to or may exceed their rest-mass energy. Such plasma, that may be created out of equilibrium, is shown to relax to thermal equilibrium on a time scale much shorter than its dynamical time [28, 29]. However, the effects of relativistic degeneracy were neglected in previous works: particles were assumed to follow Boltzmann statistics. Besides, the three-particle interactions were taken into account approximately, assuming that plasma reaches kinetic equilibrium before they become relevant. This

last approximation is justified in mildly relativistic plasma, but fails for higher energy densities, as rates of three-particle interactions become comparable to two-particle ones. Therefore, in Chapter 1 we revised the issue of thermalization in relativistic degenerate plasma. In the collision integrals of relativistic Boltzmann equations we take into account the Pauli blocking and the Bose enhancement factors of all two-particle and three-particle interactions in plasma. As in previous works [28, 30] two-particle interactions are described by exact quantum electrodynamics (QED) matrix elements. In addition, all three-particle interactions are now described by QED matrix elements as well. Relaxation time scales are computed and compared with previous ones of [31].

Provided that relativistic plasma in the sources of GRBs reaches thermal equilibrium prior to its expansion, relativistic thermodynamics and hydrodynamics can be applied to description of such a plasma. A brief review of GRB hydrodynamics is given in Chapter 2. Particular attention is given to initial and boundary conditions for relativistic hydrodynamic equations. Two popular models in the literature, namely relativistic steady wind and relativistically expanding thin shell, are recalled. We propose a new hydrodynamic model of relativistic outflow, which represents steady wind and thin shell in corresponding limiting cases. We also discuss the hydrodynamic spreading [32, 33] due to possible Lorentz factor gradient. In addition we consider another mechanism of radial spreading due to thermal velocity dispersion in expanding plasma.

In Chapter 3 we consider the optical depth of relativistically moving medium. On simple examples we show the appearance of several asymptotic solutions for the optical depth. The hydrodynamic model proposed in Chapter 2 is used to compute the optical depth and corresponding transparency radius of relativistic outflows. The new notions of photon thick and photon thin outflows are introduced for illustration of corresponding asymptotic expressions of optical depth.

In Chapter 4 we focus on light curves and spectra of the emission originating from transparency of relativistic outflows. Our method is based on the solutions of the radiative transfer equation. For photon thick outflows light curves and spectra are computed using "fuzzy photosphere" approximation, which accounts for the emission from different regions of the outflow by the corresponding probability density function introduced in [23], see also [25]. For photon thin outflows radiative diffusion is found to play important role, in contrast with the photon thick case, photons are decoupled from plasma from the boundaries of the outflow, where they are transported to by diffusion.

In a different field of astrophysics and cosmology since the pioneering works of Zwicky [34, 35], observations of galaxies and clusters of galaxies have shown that the orbital velocities in these systems are around several hundreds km/s, which implies that the ratio between the total mass and the luminous mass is ten times higher than expected for a galaxy containing only luminous matter. This problem did not receive much attention from astrophysicists, who thought it to be a measurement problem, until the 1970s, when more accurate observations were shown that the orbital velocities tend to a constant value far away from the center of the galaxies, implying that there was some amount of non-luminous matter present, see e.g. [36, 37]. This non-luminous matter was dubbed Dark Matter (DM). More recently, using gravitational lensing and Cosmic Microwave Background (CMB) probes like COBE and WMAP, DM was shown to be present also in clusters of galaxies and at cosmological scales. Using CMB data and constraints from the Big Bang Nucleosynthesis, it also appears that this matter in not baryonic, i.e., not composed of three quarks like protons and neutrons [38]. What is actually DM made of and how it is distributed in the galaxies is still unknown.

The aim of the Chapter 5 is to present a unified approach in modeling of the dark matter distribution in the galactic halos and also in the galactic center. We model the DM as fermionic noninteracting particles. The semidegenerate configurations of fermionic DM in equilibrium were studied in [39–41] in Newtonian gravity and in General Relativity. We extend these studies, comparing the rotational curves of such configurations to the phenomenological models of DM distributions in Galaxies. We also obtain the limits on the configuration parameters that follows from the law of constant DM surface density [42–45].

Chapter 1

Relativistic degeneracy in nonequilibrium electron-positron plasma

The description of processes involving electron-positron plasma is required in many phenomena in physics and astrophysics [5]. The standard cosmological model includes lepton era with electron-positron plasma at high temperature and initially in thermal equilibrium, see e.g. [46]. Strong electromagnetic fields are generated in laser experiments aiming at production of electron-positron pairs [47, 48]. When electromagnetic field invariants $\mathbf{E}^2 - \mathbf{H}^2$ and $\mathbf{E} \cdot \mathbf{H}$ approach critical value, vacuum breakdown is predicted [49] to lead to copious pair production, ultimately forming electron-positron plasma [50]. Strong electromagnetic fields are thought to occur in astrophysical conditions, near such compact objects as black holes [51], hypothetical strange stars [52, 53] and possibly neutron stars [54].

Pair production by vacuum breakdown or by laser beam interactions is in principle the out of equilibrium process. Relaxation of electron-positron plasma to thermal equilibrium has been considered in [28, 30]. There relativistic Boltzmann equations with exact QED collision integrals taking into account all relevant two-particle (Bhabha scattering, Møller scattering, Compton scattering, pair creation and annihilation) and three-particle (relativistic bremsstrahlung, three photon annihilation, double Compton scattering, and radiative pair production) interactions were solved numerically. It was confirmed that a metastable state called *"kinetic equilibrium"* [55] exists in such plasma, which is characterized by the same temperature of all particles, but nonnull chemical potentials. Such state

occurs when the detailed balance of all two-particle reactions is established. It was pointed out that direct and inverse three-particle interactions become relevant when kinetic equilibrium has been reached. These three-particle interactions are shown to be essential [28] in bringing electron-positron plasma to thermal equilibrium, as they are particle non-conserving processes.

In [31] relaxation timescales for optically thick electron-positron plasma in a wide range of temperatures and proton loadings were computed numerically using the kinetic code developed in [28, 30]. These timescales were previously estimated in the literature by order of magnitude arguments using the reaction rates of the dominant processes [56, 57]. It was shown that these numerically obtained timescales differ from previous estimations by several orders of magnitude. In the description of plasma Boltzmann statistics of particles was used in all these works. However, electrons, positrons and photons are quantum particles fulfilling Fermi-Dirac and Bose-Einstein statistics, respectively. This leads to change of reaction rates considered firstly in [58, 59]. The role of relativistic degeneracy in pair plasma in establishing thermal equilibrium has never been studied. In this Chapter we bridge this gap.

We generalize previous works on thermalization of uniform isotropic neutral pair plasma. In addition to collision integrals for two-particle interactions expressed through QED matrix elements we take into account also three-particle interactions in the same way. Plasma degeneracy is accounted for by quantum corrections to collision integrals with the corresponding Pauli blocking and Bose enhancement factors. In Sec. 1.1 basic parameters of pair plasma are introduced. In Sec. 1.2 concepts of kinetic and thermal equilibria and their relations to detailed balance conditions are recalled. In Sec. 1.3 relativistic Boltzmann equation is introduced. In Sec. 1.3.1 two-particle collision integrals are described. In Sec. 1.3.2 three-particle collision integrals are introduced. In Sec. 1.4 details of adopted numerical scheme are given. In Sec. 1.5 our numerical results of integration of Boltzmann equations for several interesting cases are described. Conclusions follow in Sec. 1.6.

1.1 Basic parameters

The qualitative character of processes in electron-positron plasma is determined by a number of parameters, which we recall below, for details see [30].

The average energy per particle $\langle\varepsilon\rangle$ determines wether plasma is in relativistic

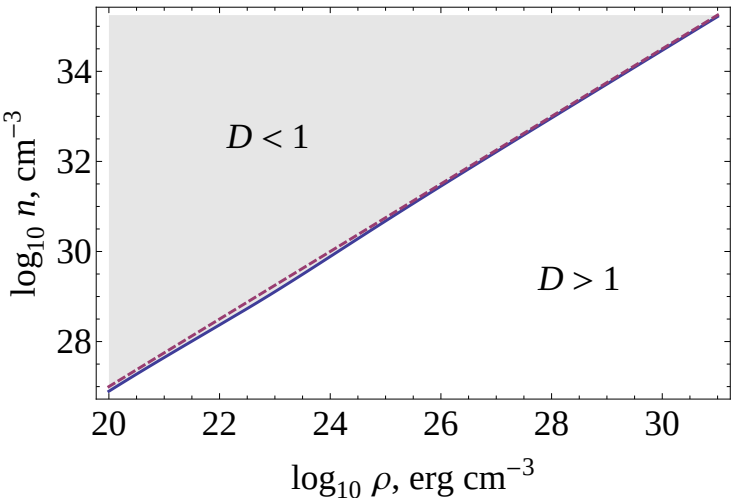

Figure 1.1: Number density-energy density diagram of relativistic electron-positron plasma. Solid curve shows critical particle density $n_{cr}(\rho)$, obtained from Eq. (1.8) with $\xi = 0$. Dashed line corresponds to transition from nondegenerate $D > 1$ to degenerate $D < 1$ plasma, where D is defined by Eq. (1.2).

or in non-relativistic domain. We consider mildly relativistic plasma with

$$0.01 \lesssim \frac{\langle \varepsilon \rangle}{m_e c^2} \lesssim 10, \tag{1.1}$$

where m_e is electron mass, c is the speed of light. This range contains both relativistic and non-relativistic domains. The upper limit is chosen to avoid thermal production of other particles such as neutrinos and muons, while the lower limit is required to have sufficient pair density [31].

The degeneracy parameter [60, p. 352] is defined as

$$D = \frac{1}{n\lambda_{th}^3}, \tag{1.2}$$

where n is number density of particles, $\lambda_{th} = \dfrac{c\hbar}{kT}$ is the thermal wave-length, k is Boltzmann constant, T is temperature, $\hbar = h/(2\pi)$, h is Planck constant. In Fig. 1.1 on the number density–energy density diagram for relativistic electron-positron plasma we show nondegenerate ($D > 1$) and degenerate ($D < 1$) regions.

The plasma parameter $\mathfrak{g}$ is defined as

$$\mathfrak{g} = \frac{1}{n\lambda_D^3}, \tag{1.3}$$

where the Debye length [60, p. 351] is

$$\lambda_D = \begin{cases} \sqrt{\dfrac{kT}{4\pi e^2 n}}, & D > 1, \\ \sqrt{\dfrac{E_F}{4\pi e^2 n}}, & D < 1, \end{cases} \tag{1.4}$$

e is electron charge, and E_F is the Fermi energy. For $\mathfrak{g} \ll 1$ plasma is called ideal, and Boltzmann equation for one-particle distribution functions can be used for its description. This is indeed the case for relativistic plasma, as discussed in [60, p. 352].

The classicality parameter defined by

$$\kappa = \frac{e^2}{\hbar v_r} = \frac{\alpha}{\beta_r}, \tag{1.5}$$

where α is the fine-structure constant, $v_r = \beta_r c$ is mean relative velocity of the particles, determines the type of cross section to be used in charged particle collisions. In relativistic plasma $\kappa \ll 1$, which requires quantum description.

The Coulomb logarithm defined by

$$\Lambda = \frac{\mathcal{M}\lambda_D \Gamma_r v_r}{\hbar}, \tag{1.6}$$

where $\mathcal{M}$ is the reduced mass of charged particles, $\Gamma_r = (1 - \beta_r^2)^{-1/2}$, characterizes the strength of screening in Coulomb interactions.

Finally, *the optical depth* τ characterizes intensity of interactions between photons and other particles. We discuss the computation of this important parameter in details in the following Chapters. In static relativistic plasma, which is the case in this Chapter, the optical depth can be estimated as

$$\tau = \sigma n l, \tag{1.7}$$

where n is electron density, σ is Thompson cross section, and l is plasma linear dimension. In this Chapter we assume $\tau \gg 1$.

1.2 Kinetic and thermal equilibria

The concepts of kinetic and thermal equilibria play important role in description of relativistic plasma. They both are connected with conditions of detailed balance established for two-particles and three-particles interactions, respectively.

1.2.1 Two-particle interactions and kinetic equilibrium

Kinetic equilibrium [55, 61] is defined as the state with vanishing difference between the rates of direct and inverse interactions for each of the two-particle processes. Such state is characterized by two parameters: common temperature of all particles T and non-null chemical potential μ. Both these parameters can be found from given energy density ρ and number density n by the system of equations

$$\begin{cases} n = \dfrac{8\pi m_e^3 c^3}{h^3}\left(2\displaystyle\int_1^\infty \frac{\epsilon\sqrt{\epsilon^2-1}}{e^{\epsilon/\theta-\xi}+1}d\epsilon + \int_0^\infty \frac{\epsilon^2}{e^{\epsilon/\theta-\xi}-1}d\epsilon\right), \\ \rho = \dfrac{8\pi m_e^4 c^5}{h^3}\left(2\displaystyle\int_1^\infty \frac{\epsilon^2\sqrt{\epsilon^2-1}}{e^{\epsilon/\theta-\xi}+1}d\epsilon + \int_0^\infty \frac{\epsilon^3}{e^{\epsilon/\theta-\xi}-1}d\epsilon\right), \end{cases} \tag{1.8}$$

where $\epsilon = \dfrac{\varepsilon}{m_e c^2}$ is dimensionless energy, $\theta = \dfrac{kT}{m_e c^2}$ is dimensionless temperature and $\xi = \dfrac{\mu}{kT}$ is dimensionless chemical potential.

For instance, the detailed balance in electron-positron pair creation and annihilation process

$$e_1^+ + e_2^- \longleftrightarrow \gamma_3 + \gamma_4 \tag{1.9}$$

Table 1.1: Two-particle processes in electron-positron plasma and detailed balance conditions

Binary interactions	Conditions
Møller and Bhabha scattering	
$e_1^{\pm} e_2^{\pm} \longleftrightarrow e_1^{\pm\prime} e_2^{\pm\prime}$ $e^{\pm} e^{\mp} \longleftrightarrow e^{\pm\prime} e^{\mp\prime}$	$n_{\pm} = \dfrac{1}{\exp \frac{\epsilon_{\pm} - \mu_{\pm}}{kT_{\pm}} + 1}$ $T_+ = T_-$
Compton scattering	
$e^{\pm}\gamma \longleftrightarrow e^{\pm}\gamma'$	$n_{\gamma} = \dfrac{1}{\exp \frac{\epsilon_{\gamma} - \mu_{\gamma}}{kT_{\gamma}} - 1}$ $T_{\pm} = T_{\gamma}$
Pair production and annihilation	
$\gamma\gamma' \longleftrightarrow e^{\pm} e^{\mp}$	$2\mu_{\gamma} = \mu_+ + \mu_-$

is described by the condition

$$f_+(\varepsilon_1) f_-(\varepsilon_2) \left[1 + \frac{f_\gamma(\varepsilon_3)}{g_\gamma h^{-3}}\right] \left[1 + \frac{f_\gamma(\varepsilon_4)}{g_\gamma h^{-3}}\right] = f_\gamma(\varepsilon_3) f_\gamma(\varepsilon_4) \left[1 - \frac{f_+(\varepsilon_1)}{g_+ h^{-3}}\right] \left[1 - \frac{f_-(\varepsilon_2)}{g_- h^{-3}}\right], \quad (1.10)$$

where $f_\alpha(\varepsilon)$ are distribution functions of particle species α, $g_\alpha = 2$ are spin weights of particles. Energies of interacting particles related by the conservation law $\varepsilon_1 + \varepsilon_2 = \varepsilon_3 + \varepsilon_4$. The distribution functions f_α are normalized as

$$n_\alpha(t) = \int f_\alpha(\mathbf{p}, t) d^3\mathbf{p}, \quad (1.11)$$

where n_α are the corresponding number densities. Similar conditions hold for the detailed balance conditions in all other two-particle interactions listed in Tab. 1.1. Combining these conditions and requiring that distribution functions for electrons and positrons (photons) have Fermi-Dirac (Bose-Einstein) form we arrive to [30]

$$\theta = \theta_+ = \theta_- = \theta_\gamma, \qquad \xi = \xi_\gamma = \xi_+ = \xi_-. \quad (1.12)$$

In fact, the chemical potential in kinetic equilibrium is constrained by the condition $\xi \leq 0$. The equality in this relation implies that there is a critical number density n_{cr} given by Eq. (1.8) with $\xi = 0$. Since in two-particle processes the total number of particles (number density) is conserved, for $n > n_{cr}$ Bose condensation of photons is expected. However, in reality three-particle interactions do change the number of particles bringing the system to thermal equilibrium with $\xi = 0$ [62].

1.2.2 Three-particle interactions and thermal equilibrium

Thermal equilibrium is defined as the state with vanishing difference between the rates of direct and inverse interactions of all processes. It was shown in [28] that in electron-positron plasma two-particle processes are insufficient to bring the non-equilibrium system to thermal equilibrium. The necessary condition for reaching thermal equilibrium is detailed balance in three-particle processes.

For instance, the detailed balance in double Compton scattering

$$e_1^{\pm} + \gamma_2 \longleftrightarrow e_3^{\pm} + \gamma_4 + \gamma_5 \tag{1.13}$$

is described by the condition

$$\begin{aligned}\frac{f_{\pm}(\varepsilon_1)}{2h^{-3}}\frac{f_{\gamma}(\varepsilon_2)}{2h^{-3}}\left[1-\frac{f_{\pm}(\varepsilon_3)}{2h^{-3}}\right]\left[1+\frac{f_{\gamma}(\varepsilon_4)}{2h^{-3}}\right]\left[1+\frac{f_{\gamma}(\varepsilon_5)}{2h^{-3}}\right]\\ = \frac{f_{\pm}(\varepsilon_3)}{2h^{-3}}\frac{f_{\gamma}(\varepsilon_4)}{2h^{-3}}\frac{f_{\gamma}(\varepsilon_5)}{2h^{-3}}\left[1-\frac{f_{\pm}(\varepsilon_1)}{2h^{-3}}\right]\left[1+\frac{f_{\gamma}(\varepsilon_2)}{2h^{-3}}\right].\end{aligned} \tag{1.14}$$

Provided that kinetic equilibrium is established, this condition, as any of the corresponding conditions of all three-particle processes, constrains the chemical potential to vanish, $\xi = 0$.

1.3 Boltzmann equations

In uniform and isotropic electron-positron plasma relativistic Boltzmann equations for distribution functions f_α have the following form [28]:

$$\frac{d}{dt}f_\alpha(\mathbf{p},t) = \sum_q \left(\eta_\alpha^q - \chi_\alpha^q f_\alpha(\mathbf{p},t)\right), \tag{1.15}$$

Table 1.2: Particle interactions in the pair plasma.

Two-particle processes	Three-particle processes
Compton scattering	Double Compton
$e^{\pm}\gamma \longrightarrow e^{\pm\prime}\gamma'$	$e^{\pm}\gamma \longleftrightarrow e^{\pm\prime}\gamma'\gamma''$
Coulomb, Møller and Bhabha scattering	Bremmstrahlung
$e_1^{\pm}e_2^{\pm} \longrightarrow e_1^{\pm\prime}e_2^{\pm\prime}$ $e^+e^- \longrightarrow e^{+\prime}e^{-\prime}$	$e_1^{\pm}e_2^{\pm} \longleftrightarrow e_1^{\pm\prime}e_2^{\pm\prime}\gamma$ $e^+e^- \longleftrightarrow e^{+\prime}e^{-\prime}\gamma$
Creation/annihilation	Three-photon annihilation
$e^+e^- \longleftrightarrow \gamma_1\gamma_2$	$e^+e^- \longleftrightarrow \gamma_1\gamma_2\gamma_3$
	Pair creation/annihilation
	$\gamma_1\gamma_2 \longleftrightarrow e^+e^-\gamma'$ $e^{\pm}\gamma \longleftrightarrow e^{\pm\prime}e^+e^-$

where the sum enumerated by index q is taken over all two- and three-particle processes q listed in Tab. 1.2, η_α^q and χ_α^q are, respectively, emission and absorption coefficients.

1.3.1 Two-particle collision integrals

Consider interaction of two incoming particles of species I and II in quantum states 1 and 2, producing two outgoing particles of species III and IV in quantum states 3 and 4. Let initial particle momenta be $\mathbf{p}_1$ in a given range $d^3\mathbf{p}_1$ and $\mathbf{p}_2$ in $d^3\mathbf{p}_2$, and final particle momenta be $\mathbf{p}_3$ in $d^3\mathbf{p}_3$ and $\mathbf{p}_4$ in $d^3\mathbf{p}_4$, respectively. This process can be symbolically represented as follows

$$I_1 + II_2 \longrightarrow III_3 + IV_4. \tag{1.16}$$

The corresponding inverse process is thus

$$III_3 + IV_4 \longrightarrow I_1 + II_2. \tag{1.17}$$

Energy and momentum conservations read

$$\hat{\varepsilon} = \varepsilon_1 + \varepsilon_2 = \varepsilon_3 + \varepsilon_4, \qquad \hat{\mathbf{p}} = \mathbf{p}_1 + \mathbf{p}_2 = \mathbf{p}_3 + \mathbf{p}_4. \tag{1.18}$$

The number of collisions per unit time and volume is, see e.g. [63, Eq. (2.1)],

$$\frac{dN}{dVdt} = d^3\mathbf{p}_1 d^3\mathbf{p}_2 d^3\mathbf{p}_3 d^3\mathbf{p}_4 \times W_{(1,2|3,4)} f_I(\mathbf{p}_1,t) f_{II}(\mathbf{p}_2,t) \left(1 \pm \frac{f_{III}(\mathbf{p}_3,t)}{2h^{-3}}\right)\left(1 \pm \frac{f_{IV}(\mathbf{p}_4,t)}{2h^{-3}}\right), \quad (1.19)$$

where W is the transition function, linked to QED matrix elements of the reaction M_{fi} as

$$W_{(1,2|3,4)} = \frac{\hbar^2 c^6}{(2\pi)^2} \frac{|M_{fi}|^2}{16\varepsilon_1\varepsilon_2\varepsilon_3\varepsilon_4} \delta(\varepsilon_1+\varepsilon_2-\varepsilon_3-\varepsilon_4)\delta^3(\mathbf{p}_1+\mathbf{p}_2-\mathbf{p}_3-\mathbf{p}_4), \quad (1.20)$$

δ is Dirac delta-function, and $\left[1 \pm f_\alpha(\mathbf{p},t)/(g_\alpha h^{-3})\right]$ are Bose enhancement (sign "$+$") and Pauli blocking (sign "$-$") factors. Matrix elements can be found, for example, in [64], Eqs. (86.6, 88.4, 81.7, 81.17).

Then collision integral for the particle I in the state 1 is

$$\eta_I(\mathbf{p}_1,t) - \chi_I(\mathbf{p}_1,t) f_I(\mathbf{p}_1,t) = \int d^3\mathbf{p}_2 d^3\mathbf{p}_3 d^3\mathbf{p}_4 \times \left[W_{(3,4|1,2)} f_{III}(\mathbf{p}_3,t) f_{IV}(\mathbf{p}_4,t) \left(1 \pm \frac{f_I(\mathbf{p}_1,t)}{2h^{-3}}\right)\left(1 \pm \frac{f_{II}(\mathbf{p}_2,t)}{2h^{-3}}\right) - W_{(1,2|3,4)} f_I(\mathbf{p}_1,t) f_{II}(\mathbf{p}_2,t) \left(1 \pm \frac{f_{III}(\mathbf{p}_3,t)}{2h^{-3}}\right)\left(1 \pm \frac{f_{IV}(\mathbf{p}_4,t)}{2h^{-3}}\right)\right]. \quad (1.21)$$

Specifically, for a scattering with $I = III$ and $II = IV$ the inverse process is the same as the direct one since pairs of indices $(1,2)$ and $(3,4)$ can be interchanged. The relation $W_{(1,2|3,4)} = W_{(3,4|1,2)}$ holds for all processes listed in Tab. 1.1. When incoming or outgoing particles coincide ($I = II$ and/or $III = IV$) quantum indistinguishability gives the term $\frac{1}{2}$ in front of the corresponding emission and absorption coefficients, see e.g. [65, p. 76], [60, p. 18].

There are 4 delta-functions in Eq. (1.20) representing conservation of energy and momentum (1.18). Three integrations over momentum of particle III can be performed immediately

$$\int d\mathbf{p}_3 \delta^3(\mathbf{p}_1+\mathbf{p}_2-\mathbf{p}_3-\mathbf{p}_4) \longrightarrow 1. \quad (1.22)$$

In the integration over energy ε_4 of particle IV it is necessary to take into account

that ε_3 is now a function of energy and angles of particles I and II, as well as angles of particle IV, so we have

$$\int d\varepsilon_4 \delta(\varepsilon_1 + \varepsilon_2 - \varepsilon_3 - \varepsilon_4) \longrightarrow \frac{1}{1 - (\beta_3/\beta_4)\mathbf{n}_3 \cdot \mathbf{n}_4}, \tag{1.23}$$

where $\mathbf{n} = \mathbf{p}/p$ is the unit vector in the direction of particle momentum, $p = |\mathbf{p}| = \sqrt{(\varepsilon/c)^2 - m^2c^2}$ is the absolute value of particle momentum, $\beta = pc/\varepsilon$, and a dot denotes scalar product of 3-vectors. We use spherical coordinates in momentum space: $\{\varepsilon, \mu, \phi\}$, $\mu = \cos\vartheta$, where ε is the particle energy, and ϑ and ϕ are polar and azimuthal angles, respectively. Then energy and angles of particle III and energy of particle IV follow from energy and momentum conservations (1.18) and relativistic energy-momentum relation, namely

$$\begin{gathered} \varepsilon_4 = c\sqrt{p_4^2 + m_{IV}^2c^2}, \qquad \varepsilon_3 = \hat{\varepsilon} - \varepsilon_4, \qquad \mathbf{p}_3 = \hat{\mathbf{p}} - \mathbf{p}_4, \\ p_4 = \frac{AB \pm \sqrt{A^2 + 4m_{IV}^2c^2(B^2-1)}}{2(B^2-1)}, \\ A = \frac{c}{\hat{\varepsilon}}[\hat{p}^2 + (m_{III}^2 - m_{IV}^2)c^2] - \frac{\hat{\varepsilon}}{c}, \qquad B = \frac{c}{\hat{\varepsilon}}\mathbf{n}_4 \cdot \hat{\mathbf{p}}. \end{gathered} \tag{1.24}$$

Then we introduce these relations into collision integral (1.21). We also use spherical symmetry in momentum space to fix angles of the particle I: $\mu_1 = 1, \phi_1 = 0$, and to perform the integration over azimuthal angle of particle II: $\int d\phi_2 \longrightarrow 2\pi$, setting $\phi_2 = 0$ in the remaining integrals. Then final expression for collision integral is

$$\begin{aligned} \eta_I(\varepsilon_1, t) - \chi_I(\varepsilon_1, t) f_I(\varepsilon_1, t) = \frac{\hbar^2}{32\pi} \int d\varepsilon_2 d\mu_2 \, d\mu_4 d\phi_4 \\ \times \frac{p_2 p_4 |M_{fi}|^2}{\varepsilon_1 \varepsilon_3 \left[1 - (\beta_3/\beta_4)\mathbf{n}_3 \cdot \mathbf{n}_4\right]} \\ \times \Bigg[f_{III}(\varepsilon_3, t) f_{IV}(\varepsilon_4, t) \left(1 \pm \frac{f_I(\varepsilon_1, t)}{2h^{-3}}\right) \left(1 \pm \frac{f_{II}(\varepsilon_2, t)}{2h^{-3}}\right) \\ - \quad f_I(\varepsilon_1, t) f_{II}(\varepsilon_2, t) \left(1 \pm \frac{f_{III}(\varepsilon_3, t)}{2h^{-3}}\right) \left(1 \pm \frac{f_{IV}(\varepsilon_4, t)}{2h^{-3}}\right) \Bigg]. \end{aligned} \tag{1.25}$$

For numerical integration, however, another expression is proved useful

$$\begin{aligned}\eta_I(\varepsilon,t)-\chi_I(\varepsilon,t)f_I(\varepsilon,t)=\frac{\hbar^2}{32\pi}\Bigg[\int d\varepsilon_3\, d\varepsilon_4 d\mu_4\, d\mu_2 d\phi_2 \\ \times\delta(\varepsilon_1-\varepsilon)\times\frac{p_2p_4|M_{fi}|^2}{\varepsilon_1\varepsilon_3\left[1-(\beta_1/\beta_2)\mathbf{n}_1\cdot\mathbf{n}_2\right]} \\ \times f_{III}(\varepsilon_3,t)f_{IV}(\varepsilon_4,t)\left(1\pm\frac{f_I(\varepsilon_1,t)}{2h^{-3}}\right)\left(1\pm\frac{f_{II}(\varepsilon_2,t)}{2h^{-3}}\right) \\ -\int d\varepsilon_2 d\mu_2\, d\mu_4 d\phi_4\times\frac{p_2p_4|M_{fi}|^2}{\varepsilon\varepsilon_3\left[1-(\beta_3/\beta_4)\mathbf{n}_3\cdot\mathbf{n}_4\right]} \\ \times\quad f_I(\varepsilon,t)f_{II}(\varepsilon_2,t)\left(1\pm\frac{f_{III}(\varepsilon_3,t)}{2h^{-3}}\right)\left(1\pm\frac{f_{IV}(\varepsilon_4,t)}{2h^{-3}}\right)\Bigg], \quad (1.26)\end{aligned}$$

where the first term, i.e. emission coefficient, is expressed in the form ready for replacement by the sum over incoming particles III and IV. In this term $\varepsilon_1, \mu_1, \phi_1, \varepsilon_2$ are given by relations (1.24) with indices exchange $1 \leftrightarrow 3$, $2 \leftrightarrow 4$, $I \leftrightarrow III$, $II \leftrightarrow IV$.

This collision integral of any of two-particle processes is a four-dimensional integral in momentum space. In Sec. 1.4 we show how such integral is computed numerically on finite grid.

1.3.2 Three-particle collision integrals

Consider interaction of two incoming particles of species I and II in quantum states 1 and 2, producing three outgoing particles of species III, IV, and V in quantum states 3, 4, and 5. Let particle momenta be $\mathbf{p}_1$ and $\mathbf{p}_2$ before the interaction, and $\mathbf{p}_3$, $\mathbf{p}_4$, and $\mathbf{p}_5$ after interaction, respectively. This process can be represented as

$$I_1 + II_2 \longrightarrow III_3 + IV_4 + V_5. \quad (1.27)$$

The corresponding inverse process is

$$III_3 + IV_4 + V_5 \longrightarrow I_1 + II_2. \quad (1.28)$$

Energy and momentum conservations give

$$\varepsilon_1 + \varepsilon_2 = \varepsilon_3 + \varepsilon_4 + \varepsilon_5, \qquad \mathbf{p}_1 + \mathbf{p}_2 = \mathbf{p}_3 + \mathbf{p}_4 + \mathbf{p}_5. \tag{1.29}$$

The number of collisions of the direct process (1.27) per unit time and volume is

$$\frac{dN}{dVdt} = d^3\mathbf{p}_1 d^3\mathbf{p}_2 d^3\mathbf{p}_3 d^3\mathbf{p}_k d^3\mathbf{p}_5 \times W_{(1,2|3,4,5)} \times f_I(\mathbf{p}_1,t) f_{II}(\mathbf{p}_2,t) \times \left(1 \pm \frac{f_{III}(\mathbf{p}_3,t)}{2h^{-3}}\right)\left(1 \pm \frac{f_{IV}(\mathbf{p}_4,t)}{2h^{-3}}\right)\left(1 \pm \frac{f_V(\mathbf{p}_5,t)}{2h^{-3}}\right). \tag{1.30}$$

For the inverse process (1.28) this number is

$$\frac{dN}{dVdt} = d^3\mathbf{p}_1 d^3\mathbf{p}_2 d^3\mathbf{p}_3 d^3\mathbf{p}_3 d^3\mathbf{p}_5 \times W_{(3,4,5|1,2)} \times f_{III}(\mathbf{p}_3,t) f_{IV}(\mathbf{p}_4,t) f_V(\mathbf{p}_5,t) \times \left(1 \pm \frac{f_I(\mathbf{p}_1,t)}{2h^{-3}}\right)\left(1 \pm \frac{f_{II}(\mathbf{p}_2,t)}{2h^{-3}}\right). \tag{1.31}$$

Then collision integral for particle I in the state 1 becomes

$$\eta_I(\mathbf{p}_1,t) - \chi_I(\mathbf{p}_1,t) f_I(\mathbf{p}_1,t) = \int d^3\mathbf{p}_2 d^3\mathbf{p}_3 d^3\mathbf{p}_4 d^3\mathbf{p}_5 \times \Bigg[W_{(3,4,5|1,2)} \times f_{III}(\mathbf{p}_3,t) f_{IV}(\mathbf{p}_4,t) f_V(\mathbf{p}_5,t) \times \left(1 \pm \frac{f_I(\mathbf{p}_1,t)}{2h^{-3}}\right)\left(1 \pm \frac{f_{II}(\mathbf{p}_2,t)}{2h^{-3}}\right) - W_{(1,2|3,4,5)} \times f_I(\mathbf{p}_1,t) f_{II}(\mathbf{p}_2,t) \times \left(1 \pm \frac{f_{III}(\mathbf{p}_3,t)}{2h^{-3}}\right)\left(1 \pm \frac{f_{IV}(\mathbf{p}_4,t)}{2h^{-3}}\right)\left(1 \pm \frac{f_V(\mathbf{p}_5,t)}{2h^{-3}}\right)\Bigg], \tag{1.32}$$

where the first term in square parenthesis corresponds to emission of particle I in inverse process (1.28), while the second term corresponds to absorption of particle I in direct process (1.27). So far we considered the case when all incoming and outgoing particles are different. When the same particle is present among incoming and outgoing ones, the collision integral for this particle species becomes more complicated.

Consider, for instance, the case when $I = V$. This particle disappears from the

quantum state 1 and appears in the quantum state 5 in the direct process (1.27). The same particle disappears from the quantum state 5 and appears in the quantum state 1 in the inverse process (1.28). Consequently two terms in the collision integral on the RHS of Boltzmann equation (1.15) are ready to be written. These are the absorption coefficient $\chi_I(\mathbf{p}_1,t)f_I(\mathbf{p}_1,t)$ in the direct process (1.27) and the emission coefficient $\eta_I(\mathbf{p}_1,t)$ in the inverse process (1.28). Both these terms appear in Eq. (1.32). However, indices denoted with arabic numbers enumerate quantum particle states, which are arbitrary. Consequently, indices 1 and 5 can be interchanged both in direct (1.27) and inverse (1.28) processes. Then two new terms in collision integral for particle I in state 1 appear: emission coefficient $\eta_I(\mathbf{p}_1,t)$ in direct process $I_5 + II_2 \longrightarrow III_3 + IV_4 + I_1$, and absorption coefficient $\chi_I(\mathbf{p}_1,t)f_I(\mathbf{p}_1,t)$ in inverse process $III_3 + IV_4 + I_1 \longrightarrow I_5 + II_2$. Combining all four terms, the collision integral in this case becomes

$$
\begin{aligned}
&\eta_I(\mathbf{p}_1,t) - \chi_I(\mathbf{p}_1,t)f_I(\mathbf{p}_1,t) = \int d^3\mathbf{p}_2 d^3\mathbf{p}_3 d^3\mathbf{p}_4 d^3\mathbf{p}_5 \\
&\times \Bigg[-W_{(1,2|3,4,5)} \times f_I(\mathbf{p}_1,t) f_{II}(\mathbf{p}_2,t) \\
&\qquad \times \left(1 \pm \frac{f_{III}(\mathbf{p}_3,t)}{2h^{-3}}\right)\left(1 \pm \frac{f_{IV}(\mathbf{p}_4,t)}{2h^{-3}}\right)\left(1 \pm \frac{f_I(\mathbf{p}_5,t)}{2h^{-3}}\right) \\
&\quad + W_{(3,4,5|1,2)} \times f_{III}(\mathbf{p}_3,t) f_{IV}(\mathbf{p}_4,t) f_I(\mathbf{p}_5,t) \\
&\qquad \times \left(1 \pm \frac{f_I(\mathbf{p}_1,t)}{2h^{-3}}\right)\left(1 \pm \frac{f_{II}(\mathbf{p}_2,t)}{2h^{-3}}\right) \\
&\quad + W_{(5,2|3,4,1)} \times f_I(\mathbf{p}_5,t) f_{II}(\mathbf{p}_2,t) \\
&\qquad \times \left(1 \pm \frac{f_{III}(\mathbf{p}_3,t)}{2h^{-3}}\right)\left(1 \pm \frac{f_{IV}(\mathbf{p}_4,t)}{2h^{-3}}\right)\left(1 \pm \frac{f_I(\mathbf{p}_1,t)}{2h^{-3}}\right) \\
&\quad - W_{(3,4,1|5,2)} \times f_{III}(\mathbf{p}_3,t) f_{IV}(\mathbf{p}_4,t) f_I(\mathbf{p}_1,t) \\
&\qquad \times \left(1 \pm \frac{f_I(\mathbf{p}_5,t)}{2h^{-3}}\right)\left(1 \pm \frac{f_{II}(\mathbf{p}_2,t)}{2h^{-3}}\right)\Bigg]. \qquad (1.33)
\end{aligned}
$$

Generally speaking, *such four terms should be present in collision integral of any reaction for a particle specie which is present both among incoming and outgoing particles, unless the process is a scattering.* This statement is valid for arbitrary number of incoming and outgoing particles. It is not limited to QED but applies to any quantum field theory in general.

All three-particle QED processes listed in Tab. 1.2, with exception of three-photon annihilation, are indeed represented by four terms in collision integrals. Such four terms for double Compton scattering with corresponding symmetrization factors were considered by Chluba [66]. It should be noted, that the detailed balance conditions discussed in Sec. 1.2.2 may be obtained [67, 68] with only two terms in collision integrals, without interchanging the states 1 and 5. However, the structure of all four coefficients is different, and their presence in collision integral (1.33) is essential.

In three-particle processes transition function W can be expressed through the differential cross-section $d\sigma$. Using the definition of $d\sigma$ [64, Eq. (64.18)] and its relation to number of collisions $\dfrac{dN}{dVdt}$ per unit time in unit volume (1.30), given by Eq. (12.7) in [69], we have

$$W_{(1,2|3,4,5)} d^3\mathbf{p}_3 d^3\mathbf{p}_4 d^3\mathbf{p}_5 = c \frac{\sqrt{[\varepsilon_1\varepsilon_2 - (\mathbf{p}_1\cdot\mathbf{p}_2)c^2]^2 - (m_I m_{II} c^4)^2}}{\varepsilon_1\varepsilon_2} d\sigma. \qquad (1.34)$$

The differential cross section in turn can be expressed through dimensionless matrix element squared X, see [70, Eq. (11.31)]. Then we obtain

$$W_{(1,2|3,4,5)} \;=\; \frac{\alpha r_e^2}{(4\pi)^2} \times \frac{c^7 X}{\varepsilon_1\varepsilon_2\varepsilon_3\varepsilon_4\varepsilon_5} \delta(\varepsilon_{initial} - \varepsilon_{final}) \delta^3(\mathbf{p}_{initial} - \mathbf{p}_{final}), \quad (1.35)$$

where $r_e = \dfrac{e^2}{m_e c^2}$ is the classical electron radius. For double Compton scattering X is given by Eqs. (3), (9), (10) of [71]. For relativistic bremsstrahlung $X = 16A$, where A is given by Eqs. in Appendix B of [72].

Matrix elements for all other processes of Tab. 1.2 can be obtained from the ones of double Compton scattering and of relativistic bremsstrahlung by the substitution law, given in [70, Sec. 8.5]. For example, exchanging initial photon with the final electron or positron in double Compton scattering

$$e_1^- + \gamma_2 \longrightarrow e_3^- + \gamma_4 + \gamma_5, \qquad (1.36)$$

we obtain three-photon annihilation process

$$e_1^- + e_3^+ \longrightarrow \gamma_2 + \gamma_4 + \gamma_5. \qquad (1.37)$$

The matrix element squared of this process (1.37) can then be obtained from the one of double Compton process (1.36) with the following substitution law

$$\mathbf{p}_3 \longrightarrow -\mathbf{p}_3, \quad \varepsilon_3 \longrightarrow -\varepsilon_3, \quad \mathbf{p}_2 \longrightarrow -\mathbf{p}_2, \quad \varepsilon_2 \longrightarrow -\varepsilon_2. \tag{1.38}$$

The detailed balance condition for three-particle processes gives

$$h^3 W_{(1,2|3,4,5)} = 2W_{(3,4,5|1,2)}. \tag{1.39}$$

Following the same line of reasoning as in the derivation of Eq. (1.26), we arrive to the collision integral in the form

$$\begin{aligned}
\eta_I(\varepsilon,t) - \chi_I(\varepsilon,t) f_I(\varepsilon,t) = \frac{\alpha r_e^2 c}{8\pi} \Bigg[\int d\varepsilon_3 \, d\varepsilon_4 d\mu_4 \, d\varepsilon_5 d\mu_5 d\phi_5 \, d\mu_2 d\phi_2 \\
\times \delta(\varepsilon_1 - \varepsilon) \times \frac{p_2 p_4 p_5 X}{\varepsilon_1 \varepsilon_3 \left[1 - (\beta_1/\beta_2)\mathbf{n}_1 \cdot \mathbf{n}_2\right]} \\
\times f_{III}(\varepsilon_3,t) f_{IV}(\varepsilon_4,t) f_V(\varepsilon_5,t) \left(1 \pm \frac{f_I(\varepsilon_1,t)}{2h^{-3}}\right) \left(1 \pm \frac{f_{II}(\varepsilon_2,t)}{2h^{-3}}\right) \\
- \int d\varepsilon_2 d\mu_2 \, d\mu_4 d\phi_4 \, d\varepsilon_5 d\mu_5 d\phi_5 \times \frac{p_2 p_4 p_5 \, X}{\varepsilon \varepsilon_3 \left[1 - (\beta_3/\beta_4)\mathbf{n}_3 \cdot \mathbf{n}_4\right]} \\
\times f_I(\varepsilon,t) f_{II}(\varepsilon_2,t) \left(1 \pm \frac{f_{III}(\varepsilon_3,t)}{2h^{-3}}\right) \left(1 \pm \frac{f_{IV}(\varepsilon_4,t)}{2h^{-3}}\right) \left(1 \pm \frac{f_V(\varepsilon_5,t)}{2h^{-3}}\right) \Bigg],
\end{aligned} \tag{1.40}$$

where again the form of the first integral is ready to be substituted by corresponding sum over incoming particles III, IV, and V. In this first integral, i.e. in the emission coefficient, in order to find energy and angles of particle I and energy of particle II relations (1.24) should be used with indices exchange $1 \leftrightarrow 3$, $2 \leftrightarrow 4$, $I \leftrightarrow III$, $II \leftrightarrow IV$, and

$$\hat{\varepsilon} = \varepsilon_3 + \varepsilon_4 + \varepsilon_5, \qquad \hat{\mathbf{p}} = \mathbf{p}_3 + \mathbf{p}_4 + \mathbf{p}_5. \tag{1.41}$$

In the absorption coefficient in order to find energy and angles of particle III and energy of particle IV from relation (1.24) instead of (1.18) the following relations must be used

$$\hat{\varepsilon} = \varepsilon_1 + \varepsilon_2 - \varepsilon_5, \qquad \hat{\mathbf{p}} = \mathbf{p}_1 + \mathbf{p}_2 - \mathbf{p}_5. \tag{1.42}$$

This collision integral (1.40) of any of three-particle processes is a seven-dimensional integral in momentum space. In the next Section we show how such integral is computed numerically on finite grid.

1.4 The numerical scheme

The main difficulty arising in computation of collision integrals in comparison with previous works [28, 30, 31] is that particle emission and absorbtion coefficients contain not only distribution functions of incoming particles, but also those of outgoing particles. Therefore we adopt a different approach which we refer to as "*reaction-oriented*" instead of "particle-oriented" one used earlier.

The phase space is divided in zones. The zone $\Omega^{\alpha}_{a,j,k}$ for particle specie α corresponds to energy ε_a, cosine of polar angle μ_j and azimuthal angle ϕ_k, where indices run in the following ranges $1 \le a \le a_{\max}$, $1 \le j \le j_{\max}$, and $1 \le k \le k_{\max}$. The zone boundaries are $\varepsilon_{a\mp1/2}$, $\mu_{j\mp1/2}$, $\phi_{k\mp1/2}$. The length of the a-th energy zone Ω^{α}_{a} is $\Delta\varepsilon_a \equiv \varepsilon_{a+1/2} - \varepsilon_{a-1/2}$. On finite grid f_α does not depend on μ and ϕ, and number density of particle α in zone a is

$$Y^{\alpha}_{a}(t) = 4\pi \int_{\varepsilon_{a-1/2}}^{\varepsilon_{a+1/2}} c^{-3}\varepsilon\sqrt{\varepsilon^2 - m_\alpha^2 c^4} f_\alpha(\varepsilon, t) d\varepsilon \\ = 4\pi c^{-3}\varepsilon_a \sqrt{\varepsilon_a^2 - m_\alpha^2 c^4} f_\alpha(\varepsilon_a, t)\Delta\varepsilon_a. \quad (1.43)$$

In this variables discretized Boltzmann equation for particle I and energy zone a reads

$$\frac{dY^{\alpha}_{a}(t)}{dt} = \sum \left[\eta^{I}_{a}(t) - \chi^{I}_{a}(t) Y^{I}_{a}(t)\right], \quad (1.44)$$

where the sum is taken over all processes involving particle I. Emission and absorption coefficients on the grid are obtained by integration of (1.26) for two-particle processes and of (1.40) for three-particle processes over the zone. The corresponding integrals are replaced by sums on the grid. For instance, absorp-

tion coefficient for incoming particle I in two-particle process (1.16) is

$$\chi_a^I(t)Y_a^I(t) = \frac{\hbar^2 c^4}{8(4\pi)^2}\sum_{b,j,s,k}\Delta\mu_j\Delta\mu_s\Delta\phi_k \times |M_{fi}|^2$$
$$\times \frac{p_4}{\varepsilon_3[1-(\beta_3/\beta_4)\mathbf{n}_3\cdot\mathbf{n}_4]} \times \frac{Y_a^I(t)}{\varepsilon_a}\frac{Y_b^{II}(t)}{\varepsilon_b} \times \left[1 \pm \frac{Y_c^{III}(t)}{\bar{Y}_c^{III}}\right]\left[1 \pm \frac{Y_d^{IV}(t)}{\bar{Y}_d^{IV}}\right], \quad (1.45)$$

where index j denotes polar angle zone of incoming particle II, index s denotes polar angle zone of outgoing particle IV, index k denotes azimuthal angle zone of outgoing particle IV, and

$$\bar{Y}_a^\alpha = 4\pi\int_{\varepsilon_{a-1/2}}^{\varepsilon_{a+1/2}} c^{-3}\varepsilon\sqrt{\varepsilon^2 - m_\alpha^2 c^4}\ (2h^{-3})d\varepsilon = 8\pi(hc)^{-3}\varepsilon_a\sqrt{\varepsilon_a^2 - m_\alpha^2 c^4}\Delta\varepsilon_a. \quad (1.46)$$

Emission coefficient of particle I in process (1.17) from integration of (1.26) is

$$\eta_a^I(t) = \frac{\hbar^2 c^4}{8(4\pi)^2}\sum_{c,d,j,s,k} C_a(\varepsilon_1)\Delta\mu_j\Delta\mu_s\Delta\phi_k \times |M_{fi}|^2$$
$$\times \frac{p_2}{\varepsilon_1[1-(\beta_1/\beta_2)\mathbf{n}_1\cdot\mathbf{n}_2]} \times \frac{Y_c^{III}(t)}{\varepsilon_c}\frac{Y_d^{IV}(t)}{\varepsilon_d} \times \left[1 \pm \frac{Y_a^I(t)}{\bar{Y}_a^I}\right]\left[1 \pm \frac{Y_b^{II}(t)}{\bar{Y}_b^{II}}\right], \quad (1.47)$$

where index j denotes polar angle zone of incoming particle IV, index s denotes polar angle zone of outgoing particle II, index k denotes azimuthal angle zone of outgoing particle II, and

$$C_a(\varepsilon_1) = \begin{cases} \dfrac{\varepsilon_a - \varepsilon_1}{\varepsilon_a - \varepsilon_{a-1}}, & \varepsilon_{a-1} < \varepsilon_1 < \varepsilon_a, \\ \dfrac{\varepsilon_{a+1} - \varepsilon_1}{\varepsilon_{a+1} - \varepsilon_a}, & \varepsilon_a < \varepsilon_1 < \varepsilon_{a+1}, \\ 0, & \text{otherwise.} \end{cases} \quad (1.48)$$

In integration of (1.26) over the zone one can integrate out the δ-function $\int \delta(\varepsilon_1 - \varepsilon)d\varepsilon_1 \longrightarrow 1$. However, when energies of incoming particles are fixed on the grid, the energies of outgoing particles are not on the grid. Hence an interpolation (1.48) is adopted, which enforces the exact number of particles and energy conservation in each two-particle process due to redistribution of outgoing particle α with energy ε over two energy zones $\Omega_n^\alpha, \Omega_{n+1}^\alpha$ with $\varepsilon_n < \varepsilon < \varepsilon_{n+1}$.

The redistribution of final particles should also satisfy requirements of quantum statistics. Therefore if a process occurs, when final particle should be distributed over the quantum states which are fully occupied, such process is forbidden. Thus we introduce the Bose enhancement/Pauli blocking coefficients in (1.45) and (1.47) as

$$\left[1 \pm \frac{\Upsilon_a^\alpha(t)}{\bar{\Upsilon}_a^\alpha}\right] = \min\left(1 \pm \frac{\Upsilon_n^\alpha(t)}{\bar{\Upsilon}_n^\alpha}, 1 \pm \frac{\Upsilon_{n+1}^\alpha(t)}{\bar{\Upsilon}_{n+1}^\alpha}\right). \tag{1.49}$$

The sum over angles μ_j, μ_s, ϕ_k can be found once and for all at the beginning of the calculations. We then store in the program for each set of the incoming and outgoing particles the corresponding terms and redistribution coefficients given by Eq. (1.48).

Extension of this scheme to three-particle interactions is straightforward. However, unlike two-particle case where pairs of indices I, II and III, IV can be interchanged, in three-particle case there is no such symmetry. Then we give absorption and emission coefficients for incoming and outgoing particles in processes (1.27) and (1.28) separately. Considering the direct process (1.27), finite difference representation of absorption coefficient for incoming particle I in (1.40) is

$$\begin{aligned}\chi_a^I(t)\Upsilon_a^I(t) = \frac{\alpha r_e^2 c^3}{2(4\pi)^2} \sum_{b,j,s,k,f,p,r} \Delta\mu_j \Delta\mu_s \Delta\phi_k \Delta\varepsilon_f \Delta\mu_p \Delta\phi_r \\ \times X \times \frac{p_4 p_5}{\varepsilon_3[1-(\beta_3/\beta_4)\mathbf{n}_3\cdot\mathbf{n}_4]} \times \frac{\Upsilon_a^I(t)}{\varepsilon_a}\frac{\Upsilon_b^{II}(t)}{\varepsilon_b} \\ \times \left[1 \pm \frac{\Upsilon_c^{III}(t)}{\bar{\Upsilon}_c^{III}}\right]\left[1 \pm \frac{\Upsilon_d^{IV}(t)}{\bar{\Upsilon}_d^{IV}}\right]\left[1 \pm \frac{\Upsilon_f^{V}(t)}{\bar{\Upsilon}_f^{V}}\right],\end{aligned} \tag{1.50}$$

and emission coefficient for outgoing particle III is

$$\begin{aligned}\eta_c^{III}(t) = \frac{\alpha r_e^2 c^3}{2(4\pi)^2} \sum_{a,b,j,s,k,f,p,r} \Delta\mu_j \Delta\mu_s \Delta\phi_k \Delta\varepsilon_f \Delta\mu_p \Delta\phi_r \\ \times C_a(\varepsilon_3) \times X \times \frac{p_4 p_5}{\varepsilon_3[1-(\beta_3/\beta_4)\mathbf{n}_3\cdot\mathbf{n}_4]} \times \frac{\Upsilon_a^I(t)}{\varepsilon_a}\frac{\Upsilon_b^{II}(t)}{\varepsilon_b} \\ \times \left[1 \pm \frac{\Upsilon_c^{III}(t)}{\bar{\Upsilon}_c^{III}}\right]\left[1 \pm \frac{\Upsilon_d^{IV}(t)}{\bar{\Upsilon}_d^{IV}}\right]\left[1 \pm \frac{\Upsilon_f^{V}(t)}{\bar{\Upsilon}_f^{V}}\right],\end{aligned} \tag{1.51}$$

where indices f, p, r denote energy, polar angle and azimuthal angle zone of outgoing particle V, respectively. Considering the inverse process (1.28), emission coefficient for the outgoing particle I is

$$\eta_a^I(t) = \frac{\alpha r_e^2 c^5 h^3}{4(4\pi)^3} \sum_{c,s,k,d,j,f,p,r} \Delta\mu_s \Delta\phi_k \Delta\mu_j \Delta\mu_p \Delta\phi_r \times C_a(\epsilon_1) \times X \times \frac{p_2}{\varepsilon_1[1-(\beta_1/\beta_2)\mathbf{n}_1\cdot\mathbf{n}_2]} \frac{\Upsilon_c^{III}(t)}{\varepsilon_c} \frac{\Upsilon_d^{IV}(t)}{\varepsilon_d} \frac{\Upsilon_f^{V}(t)}{\varepsilon_f} \times \left[1 \pm \frac{\Upsilon_a^I(t)}{\bar{\Upsilon}_a^I}\right] \left[1 \pm \frac{\Upsilon_b^{II}(t)}{\bar{\Upsilon}_b^{II}}\right], \quad (1.52)$$

while absorption coefficient for the incoming particle III is

$$\chi_c^{III}(t)\Upsilon_c^{III}(t) = \frac{\alpha r_e^2 c^5 h^3}{4(4\pi)^3} \sum_{s,k,d,j,f,p,r} \Delta\mu_s \Delta\phi_k \Delta\mu_j \Delta\mu_p \Delta\phi_r \times X \times \frac{p_2}{\varepsilon_1[1-(\beta_1/\beta_2)\mathbf{n}_1\cdot\mathbf{n}_2]} \frac{\Upsilon_c^{III}(t)}{\varepsilon_c} \frac{\Upsilon_d^{IV}(t)}{\varepsilon_d} \frac{\Upsilon_f^{V}(t)}{\varepsilon_f} \times \left[1 \pm \frac{\Upsilon_a^I(t)}{\bar{\Upsilon}_a^I}\right] \left[1 \pm \frac{\Upsilon_b^{II}(t)}{\bar{\Upsilon}_b^{II}}\right], \quad (1.53)$$

where indices s and k denote polar and azimuthal angle zones of outgoing particle II, respectively; index j denotes polar angle zone of incoming particle IV, and indices f, p, r denote energy, polar angle and azimuthal angle zone of particle V, respectively.

In these sums (1.50–1.53) summation over angles μ_j, μ_s, ϕ_k, μ_p, ϕ_r again can be performed once and for all at the beginning of the calculations. Representation of discretized collisional integral for particle I and energy zone a in processes

(1.16, 1.17, 1.27, 1.28) is

$$\frac{dY_a^I}{dt} = -\sum A \times Y_a^I(t) Y_b^{II}(t) \times \left[1 \pm \frac{Y_c^{III}(t)}{\bar{Y}_c^{III}}\right] \left[1 \pm \frac{Y_d^{IV}(t)}{\bar{Y}_d^{IV}}\right] + \sum B \times Y_c^{III}(t) Y_d^{IV}(t) \times \left[1 \pm \frac{Y_a^I(t)}{\bar{Y}_a^I}\right] \left[1 \pm \frac{Y_b^{II}(t)}{\bar{Y}_b^{II}}\right] - \sum C \times Y_a^I(t) Y_b^{II}(t) \times \left[1 \pm \frac{Y_c^{III}(t)}{\bar{Y}_c^{III}}\right] \left[1 \pm \frac{Y_d^{IV}(t)}{\bar{Y}_d^{IV}}\right] \left[1 \pm \frac{Y_f^V(t)}{\bar{Y}_f^V}\right] + \sum D \times Y_c^{III}(t) Y_d^{IV}(t) Y_f^V(t) \times \left[1 \pm \frac{Y_a^I(t)}{\bar{Y}_a^I}\right] \left[1 \pm \frac{Y_b^{II}(t)}{\bar{Y}_b^{II}}\right], \quad (1.54)$$

where constant coefficients A, B, C, D are obtained from the summation over angles in the sums (1.45, 1.47, 1.50, 1.52). The full Boltzmann equation (1.44) contains similar sums for all processes from Tab. 1.2. Each individual term in these sums appears in the system of discretized Boltzmann equations four or five times in emission and absorption coefficients for each particle entering a given process. Then each term can be computed only once and added to all corresponding sums, that is the essence of our *"reaction-oriented" approach*.

In our method exact energy and number of particles conservation laws are satisfied. The number of energy intervals is typically 20, while internal grid of angles has 32 points in μ and 64 in ϕ. The system under consideration has several characteristic times for different processes, and therefore the resulting system of ordinary differential equations (1.44) is stiff. We use Gear's method [73] to integrate the system numerically.

1.5 Characteristic time scales of plasma relaxation

We solved numerically Boltzmann equation (1.15) in two cases. Initially only photons are present with constant spectral energy density and total energy density $\rho = 10^{23}$ erg/cm^3 and $\rho = 10^{29}$ erg/cm^3. Such energy densities corresponds to the temperature θ in thermal equilibrium of 0.3 and 8, respectively.

In Figs. 1.2 and 1.3 we present number density, energy density, temperature and chemical potential of photons and pairs in both cases. We also show the difference between quantum and Boltzmann statistics by including and omitting the Pauli blocking and Bose enhancement factors in evolution equations (1.54).

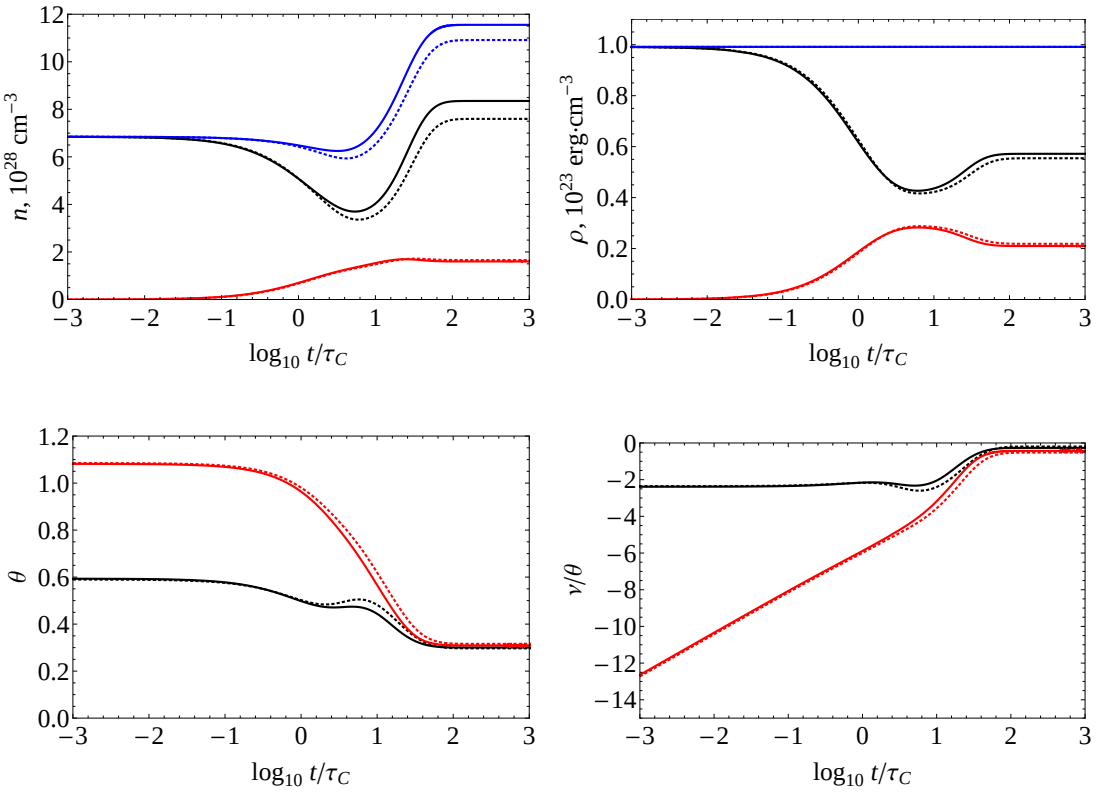

Figure 1.2: Comparison of evolution of number n and energy ρ densities, dimensionless temperature θ, chemical potential ξ, for quantum (solid curves) and classical (dotted curves) statistics with total energy density $\rho = 10^{23}$ erg/cm^3. Black and red curves correspond to photons and pairs, respectively, blue curve gives the sum of densities.

Time is expressed in units of Compton time

$$\tau_C = \frac{1}{\sigma_T n_\pm c}, \tag{1.55}$$

where $n_\pm$ is number density of pairs in thermal equilibrium, σ_T is Thomson cross section.

Timescales of relaxation to thermal equilibrium for quantum (classical) statistics nearly coincide: $15\tau_C$ ($18\tau_C$) for $\rho = 10^{23}$ erg/cm^3, and $27\tau_C$ ($23\tau_C$) for $\rho = 10^{29}$ erg/cm^3. Inspection of Figs. 1.2 and 1.3 indicates that both temperatures and chemical potentials of leptonic and photon components become nearly equal when the total number density of particles shown by blue curves is almost constant. This fact indicates that three-particle interactions become relevant when almost detailed balance (kinetic equilibrium) is established by two-particle in-

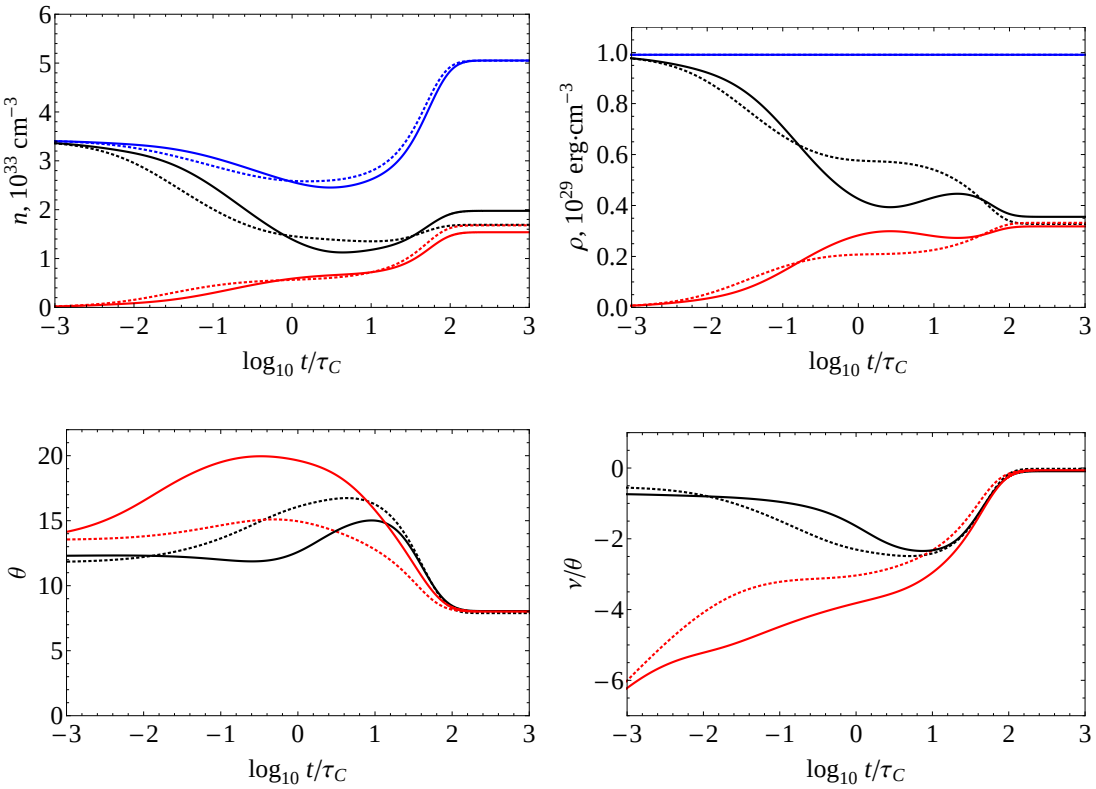

Figure 1.3: The same as in Fig. 1.2, but for total energy density $\rho = 10^{29}$ erg/cm^3.

teractions [28]. Notice, however, that due to energy dependence of reaction rates the characteristic timescale on which kinetic equilibrium is established is larger than Compton time (1.55). For the same reason the characteristic timescale on which thermal equilibrium is established is smaller than the simple estimate $\alpha^{-1}\tau_C$. Thus the ratio of the timescales of kinetic and thermal equilibrium is no longer α but higher. This fact shows why the exact treatment of three-particle interactions, especially for high energy densities, becomes important.

In Figs. 1.4 and 1.5 we show spectral evolution for both our initial conditions. The final spectra shown for $t = 10^3\tau_C$ are in good agreement with Planck/Fermi-Dirac distribution functions, correspondingly, obtained for the given energy density, typically within 5 % accuracy. Notice that at the Compton time both electron/positron and photon spectra are far from equilibrium shape, with the only exception of leptonic spectrum for $\rho = 10^{23}$ erg/cm^3. This quick relaxation of leptonic component is due to large Coulomb logarithm for non-relativistic temperatures.

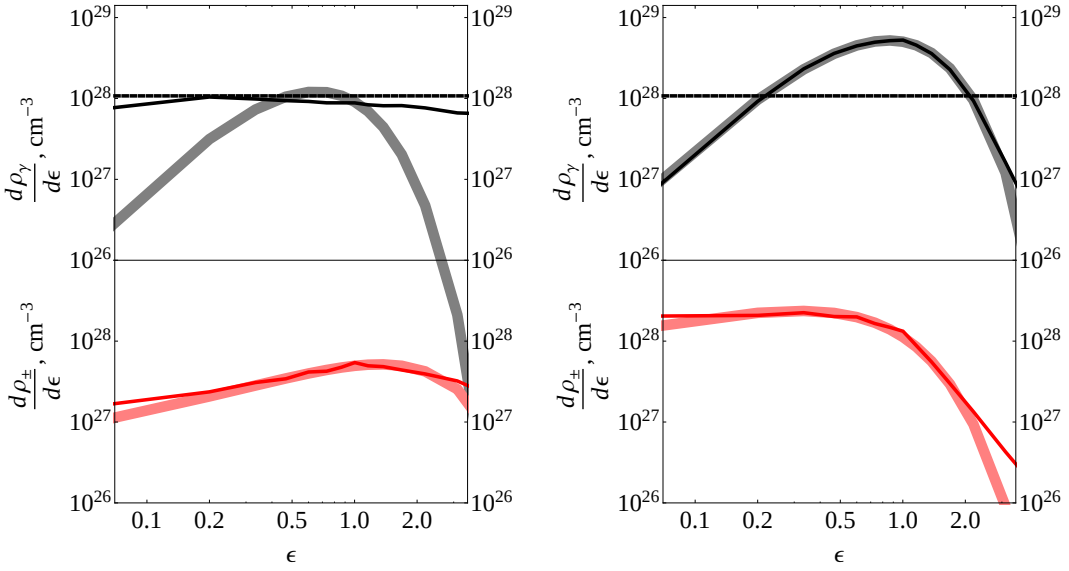

Figure 1.4: Numerical spectral energy densities of photons (black line) and pairs (red line) at $t = \tau_C$ (left) and at $t = 10^3\tau_C$ (right) for $\rho = 10^{23}$ erg/cm^3. Thick curves show the corresponding Bose-Einstein and Fermi-Dirac distributions with the same number and energy densities, respectively. Dashed thin line shows initial photon spectrum.

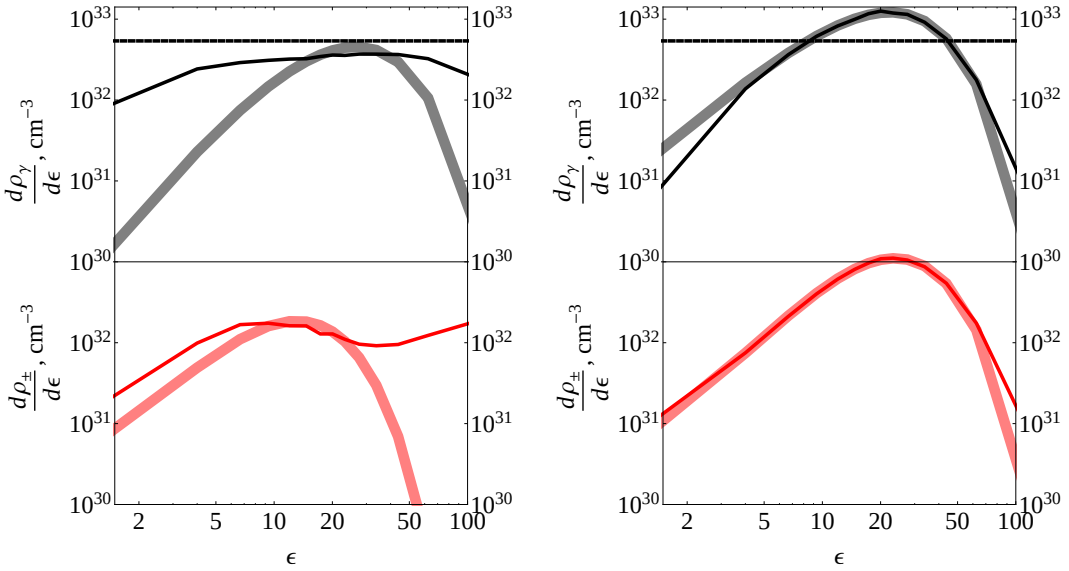

Figure 1.5: The same as in Fig. 1.4 for $\rho = 10^{29}$ erg/cm^3.

1.6 Conclusions

In this Chapter we consider relaxation of nonequilibrium optically thick pair plasma to complete thermal equilibrium by integrating numerically relativistic Boltzmann equations with exact QED two-particle and three-particle collision integrals. Quantum nature of particle statistics is accounted for in collision integrals by the corresponding Bose enhancement and Pauli blocking factors.

We point out that unlike classical Boltzmann equation for binary interactions such as scattering, more general interactions are typically described by four collision integrals for each particle that appears both among incoming and outgoing particles.

The partial summations over angles in three-particle processes appears to be the most time-consuming part of the numerical solution of Boltzmann equation. Typical number of points in calculations is 10^{12}.

Our numerical results indicate that the rates of three-particle interactions become comparable to those of two-particle ones for temperatures exceeding the electron rest-mass energy. Thus three particle interactions such as relativistic bremsstrahlung, double Compton scattering, and radiative pair creation become essential not only for establishment of thermal equilibrium, but also for correct estimation of interaction rates, energy losses etc.

Chapter 2

Hydrodynamics of GRBs

Observations of time-resolved spectra from GRBs indicate the presence of relativistic motion. This fact follows from the compactness argument, see e.g. Sec. 4 of [7], as observations of nonthermal spectra from initially optically thick plasma require ultrarelativistic velocity of expansion.

GRBs are known to be located at cosmological distances, thanks to detection of their X-ray afterglows [74]. Total number of photons emitted from the source during time δt is

$$N_\gamma = \frac{E_\gamma}{\varepsilon_\gamma} = \frac{L_\gamma \delta t}{\varepsilon_\gamma}, \tag{2.1}$$

where E_γ is the total energy of the photons, L_γ is the luminosity of the source, ε_γ is the average energy of photon. Assuming the source is at rest, the optical depth of emitting region to pair production $\gamma\gamma \longrightarrow e^+e^-$ is

$$\tau_{\gamma\gamma} \sim n_\gamma \sigma_T R_{er} \sim \frac{N_\gamma \sigma_T}{R_{er}^2} \sim \frac{L_\gamma \sigma_T}{\varepsilon_\gamma c^2 \delta t} \sim 10^{15}, \tag{2.2}$$

where n_γ is the photon number density, σ_T is Thomson cross section, linear dimension of emitting region is $R_{er} \sim c\delta t$, and we assumed typical values of GRB parameters $L_\gamma \sim 10^{52}$ erg/s, $\delta t \sim 1$ ms, $\varepsilon_\gamma \sim 1$ MeV. Eq. (2.2) implies that indeed the source is optically thick. The compactness argument is based on the dependence of $\tau_{\gamma\gamma}$ on the Lorentz factor of the bulk motion of expanding plasma. The corresponding lower limit, which follows from the condition $\tau_{\gamma\gamma} \leq 1$, is typically $\Gamma \gtrsim 100$. The presence of such ultrarelativistic motion requires description in terms of relativistic hydrodynamics.

In this Chapter we focus on the baryonic thermally accelerated GRB model which includes both fireball [3, 7] and fireshell [75] models. In the optically thick phase of expansion the plasma is assumed to be composed of two components: baryons with nonrelativistic equation of state, and photons with ultrarelativistic equation of state. When electron-positron pairs are present, their equation of state can be also considered ultrarelativistic for simplicity. We also assume spherical symmetry. Then any relativistic outflow of such composition can be characterized by the following three hydrodynamical quantities: comoving number density of baryons $n_B(r,t)$, total comoving energy density $\rho(r,t)$, and Lorentz factor $\Gamma(r,t)$. Any finite outflow can then be discretized and represented by the sequence of thin shells with thickness δ with constant hydrodynamic quantities within the shell. Each individual subshell is characterized by $n_{B,i}(t), \rho_i(t), \Gamma_i(t)$, i being the number of the subshell. Usually in the literature instead of time dependence of these quantities, their dependence on the radial position R of a given subshell is considered.

In this Chapter we review the hydrodynamic phase of GRBs and recall the derivation of the expressions for $n(R), \rho(R)$, and $\Gamma(R)$. These results will be used in subsequent Chapters. In Sec. 2.1 we discuss initial and boundary conditions for hydrodynamic equations. Two particular classes of these conditions lead to wind and shell models of GRBs. In Sec. 2.2 we recall hydrodynamic equations and their solutions for ultrarelativistic outflows. We also consider spatial spreading of the relativistically expanding plasma in Sec. 2.4. In Sec. 2.5 we discuss also additional mechanism of spreading due to thermal velocity dispersion, and in Sec. 2.6 we show that for typical GRB parameters thermal effects are negligible. Conclusions follow.

2.1 Initial and boundary conditions: wind and shell models

Consider the release of energy E_0 in a source of radius R_0 loaded with mass M.

When the energy is released gradually, on a time scale $\Delta t \gg R_0/c$, the resulting outflow is characterized by activity time Δt and the quantities defined on the boundary R_0: energy ejection rate $L = dE/dt$, mass ejection rate $\dot{M} = dM/dt$, and ejection velocity v_0. Such initial and boundary conditions are generally referred to as *a wind*. The comoving energy density on the boundary R_0 is given by

$\rho = L/(4\pi R_0^2 v_0 \Gamma_0^2)$ with $\Gamma_0 = (1 - v_0^2/c^2)^{-1/2}$. In thermal equilibrium this corresponds to the temperature $T \sim (\rho/\sigma_{SB})^{1/4}$, where σ_{SB} is the Stefan-Boltzmann constant.

In principle, all these quantities may depend on time, that would produce the variable outflow with $n_B(r,t)$, $\rho(r,t)$, and $\Gamma(r,t)$. Particulary simple choice $L(t) = \text{const}, \dot{M}(t) = \text{const}, v_0(t) = \text{const}, R_0 = \text{const}, \Delta t \to \infty$ gives rise to the model of *steady infinite wind* [11]. This is the most actively studied model, see e.g. [23, 24, 24–26, 76], provided by its simplicity. In [77] the authors considered gravitational collapse of a charged shell with the electric field exceeding the critical value $E_{cr} = (m_e^2 c^3)/(e\hbar) \simeq 1.323 \times 10^{16}$ V/cm. In that model of relativistic wind all parameters explicitly depend on time.

Sudden energy release can be considered as a special case of wind with $\Delta t \simeq R_0/c$. In the literature a model of sudden energy release is considered with $\Delta t \to 0$ [10, 32, 33, 78, 79]. In this model energy E_0 and mass M are initially distributed with, respectively, densities $\rho(r, t = 0)$ and $m_p n(r, t = 0)$ and initial velocity $v(r, t = 0)$ within the sphere of radius R_0, and vacuum outside it. Such initial conditions give rise to the model of *thin shell* [32, 33, 78, 79]. Particulary simple choice is uniform distributions $\rho(r) = \text{const}, n(r) = \text{const}$ with $v(r) = 0$, see [10] and [80].

In the following Chapters we consider a wind with $L = \text{const}, \dot{M} = \text{const}, v_0 = \text{const}, R_0 = \text{const}$ with finite activity time Δt. Clearly steady infinite wind can be recovered in this model with $\Delta t \to \infty$. Due to ultrarelativistic character of expansion also thin shell can be recovered with $\Delta t = R_0/c$. From the point of view of dynamics the key parameter is the baryonic loading [20, 80, 81]

$$B = \frac{Mc^2}{E_0} = \frac{\dot{M}c^2}{L}. \tag{2.3}$$

2.2 Relativistic hydrodynamics of expansion

Hydrodynamic expansion of GRB plasma far from the origin may be studied within the formalism of Special Relativity. General Relativity effects may be included by taking Schwarzschild or Kerr-Newman metric. However, we are interested in optically thick plasma which expands with acceleration and propagates far from its source, where the spatial curvature effects may be neglected. For this reason we simplify the treatment and adopt a spatially flat metric. The interval

in laboratory frame is taken in the form

$$ds^2 = -c^2dt^2 + dr^2 + r^2d\vartheta^2 + r^2\sin^2\vartheta d\varphi^2. \tag{2.4}$$

Following [82], we start with the energy-momentum conservation, that in curvilinear coordinates reads

$$(T^{\mu\nu})_{;\nu} = \frac{1}{\sqrt{-\det g_{\mu\nu}}}\frac{\partial(\sqrt{-\det g_{\mu\nu}}\,T^{\mu\nu})}{\partial x^\nu} + \Gamma^\mu_{\nu\lambda}T^{\nu\lambda} = 0, \tag{2.5}$$

where $\Gamma^\mu_{\nu\lambda}$ are Cristoffel symbols and $\det g_{\mu\nu}$ is determinant of the metric tensor. We assume for the energy-momentum tensor

$$T^{\mu\nu} = p\,g^{\mu\nu} + \omega\,U^\mu U^\nu, \tag{2.6}$$

where U^μ is four-velocity, $\omega = \rho + p$ is comoving enthalpy, p is comoving pressure and ρ is comoving energy density.

The energy conservation equation is the zeroth component of (2.5)

$$\left(T^{0\nu}\right)_{;\nu} = \omega U^0 U^\nu{}_{;\nu} + U^\nu\left(\omega U^0\right)_{;\nu} = 0. \tag{2.7}$$

When plasma is optically thick, radiation is trapped in it and entropy conservation applies. It may be obtained multiplying (2.5) by four-velocity

$$-U_\mu\,(T^{\mu\nu})_{;\nu} = U^\mu\rho_{;\mu} + \omega U^\mu{}_{;\mu} = 0. \tag{2.8}$$

Using the second law of thermodynamics, see e.g. [83]

$$d\left(\frac{\omega}{n}\right) = Td\left(\frac{\sigma}{n}\right) + \frac{1}{n}dp, \tag{2.9}$$

where $\sigma = \omega/T$ is comoving entropy density, T is the comoving temperature, and n is comoving density, one may rewrite (2.8) as

$$(\sigma U^\mu)_{;\mu} = U^\mu\sigma_{;\mu} + \sigma U^\mu{}_{;\mu} = 0. \tag{2.10}$$

Baryon number conservation equation for comoving density of baryons n_B has

exactly the same form

$$(n_B U^\mu)_{;\mu} = U^\mu n_{B;\mu} + n_B U^\mu{}_{;\mu} = 0. \tag{2.11}$$

Equations (2.7), (2.8), and (2.11) together with equation of state $p(\rho)$ and appropriate initial and boundary conditions were solved for thin shell model numerically, see [10, 32, 33] and analytically, see [84]. For the steady wind model solutions of Eqs. (2.7), (2.8), and (2.11) were found analytically in [11] and numerically in [27]. Nonequilibrium effects were considered for the steady wind in [85] and for thin shell in [78, 79] using rate equation formalism.

In the case of sudden energy release considered in [32, 33] it was found that expanding plasma forms a thin shell (hence the name). The width l of the shell measured in laboratory reference frame remains constant $l \simeq R_0$ until the radius R of the shell reaches the value

$$R_b = 2\Gamma^2 l, \tag{2.12}$$

where Γ is the average Lorentz factor of the shell. During this phase the density and energy profiles of the outflow are "frozen" in laboratory frame, that is called "frozen-pulse approximation" in [33]. Hydrodynamic simulations [32, 33] show that for $R > R_b$ shell width increases linearly with radius $l \simeq R(R_0/R_b)$ due to gradient of expansion velocity developed inside the shell. We discuss this hydrodynamic spreading in Sec. 2.4.

The fact $l \simeq$ const for $R < R_b$ has been used in [78, 79] to simplify the hydrodynamic description of expanding shell by averaging all quantities over its width. These averaged values satisfy the set of ordinary differential equations. The reliability of such *averaged shell* approximation, referred to as "constant thickness approximation" in [79], has been verified by direct comparison to the solution of hydrodynamic equations (2.7), (2.8) and (2.11).

In the fireshell model [75] it is assumed that pure electron-positron plasma forms in the source of GRB. This plasma expands and interacts with the remnant of GRB progenitor represented by shell of cold baryons. It is found in [79] that after interaction between expanding plasma and baryon shell, the resulting

electron-positron-baryon plasma shell expands keeping its original width for

$$B \leq 10^{-2}. \tag{2.13}$$

Now following [82], see also [33, 78–80], we derive the scaling laws for the averaged over the thin shell comoving quantities: baryon density $\langle n \rangle$, energy density $\langle \rho \rangle$, temperature $\langle T \rangle$, and Lorentz factor $\langle \Gamma \rangle$.

Recalling that $U^\mu \dfrac{\partial}{\partial x^\mu} = \dfrac{d}{dt_c}$, $U^\mu{}_{;\mu} = \dfrac{d \ln V_c}{dt_c}$, and $U_0 = -\Gamma$, where V_c is comoving volume, t_c is the comoving time, from Eqs. (2.7), (2.8), and (2.11) we get for every differential shell

$$d\rho + \omega d \ln V_c = 0, \qquad d \ln n_B + d \ln V_c = 0, \qquad d \ln(\omega\Gamma) + d \ln V_c = 0. \tag{2.14}$$

Introducing the thermal index $\gamma = 1 + \frac{p}{\rho}$ restricted by the inequality $1 \leq \gamma \leq 4/3$ and *integrating over finite volume* V_c we obtain the following scaling laws for number and energy densities averaged over this volume

$$\langle \rho \rangle V_c^{\langle \gamma \rangle} = \text{const}, \qquad \langle n_B \rangle V_c = \text{const}, \qquad \langle \omega\Gamma \rangle V_c = \text{const}. \tag{2.15}$$

One can derive [33, 82] the corresponding scaling laws for the average comoving temperature by splitting the total energy density into nonrelativistic (with $\gamma = 1$) and ultrarelativistic (with $\gamma = 4/3$) parts with $\rho \to n_B mc^2 + \varepsilon$, where m is the mass of particles[1], ε is proper internal energy density. The entropy of the ultrarelativistic component is then $\sigma = \dfrac{4}{3}\dfrac{\varepsilon}{T}$, and (2.10) gives

$$\frac{\langle \varepsilon \rangle V_c}{\langle T \rangle} = \text{const}. \tag{2.16}$$

For $\varepsilon \gg n_B mc^2$, which is the energy dominance condition, internal energy plays dynamical role by influencing the laws of expansion. For $\varepsilon \ll n_B mc^2$, which is the matter dominance condition, internal energy does not play any dynamical role, but determines the scaling law of the temperature. In order to understand the dynamics of thermodynamic quantities, one should write down the corre-

[1]Nonrelativistic component is represented by baryons. For simplicity we assume only one sort of baryons, say protons, having mass m. Ultrarelativistic component is represented by photons and electron-positron pairs.

sponding equations of motion.

The volume of the differential shell located at r, measured in the laboratory reference frame is

$$dV = 4\pi r^2 dr, \tag{2.17}$$

while the same volume measured in the reference frame comoving with the shell is

$$dV_c = 4\pi\Gamma r^2 dr, \tag{2.18}$$

where we neglect the hydrodynamic spreading.

Consider an expanding ultrarelativistic shell with laboratory radius R, laboratory width l, and Lorentz factor $\Gamma = \text{const}$ across the shell. For fixed laboratory time and $l \ll R$ comoving volume of the shell is $V_c \simeq 4\pi\Gamma R^2 l$.

Then omitting averaging $\langle \dots \rangle$ for simplification of notation we rewrite the conservation equations (2.15) as [86]

$$\rho^{\frac{1}{\gamma}}\Gamma R^2 = \text{const}, \qquad n_B\Gamma R^2 = \text{const}, \qquad \rho\Gamma^2 R^2 = \text{const}, \tag{2.19}$$

leading to the solution

$$\Gamma \propto R^{\frac{2(\gamma-1)}{2-\gamma}}, \quad n_B \propto R^{-\frac{2}{2-\gamma}}, \quad \rho \propto R^{-\frac{2\gamma}{2-\gamma}}. \tag{2.20}$$

These relations can be applied to the geometrically thin expanding shell with R being its radius. Since the shell is expanding, the equation of motion $R(t)$ should be specified. However, in ultrarelativistic limit simple relation $R(t) \simeq ct$ can be used. From the other hand, the same equations hold for steady wind, with R being the radial position, see e.g. [3, 7].

For the ultrarelativistic equation of state with $\gamma = 4/3$ we obtain

$$\Gamma \propto R, \quad n_B \propto R^{-3}, \quad \rho \propto R^{-4}. \tag{2.21}$$

As Γ is linearly increasing with radius, this phase of expansion is called acceleration phase. In the presence of baryons as the pressure decreases, plasma becomes matter dominated and expansion velocity saturates. Hence for the nonrelativistic

equation of state with $\gamma = 1$ different scaling laws come out

$$\Gamma \simeq \text{const}, \quad n_B \propto R^{-2}, \quad \rho \propto R^{-2}. \tag{2.22}$$

Since velocity gets constant, the expansion enters the coasting phase. Transition between the two regimes (2.21) and (2.22) occurs at the saturation radius

$$R_s = B^{-1} R_0, \tag{2.23}$$

where R_0 is initial size of plasma.

From (2.19) we obtain for internal energy density and temperature at acceleration phase

$$\varepsilon \propto R^{-4}, \quad T \propto R^{-1}, \quad R_0 < R < R_s, \tag{2.24}$$

and at coasting phase

$$\varepsilon \propto R^{-8/3}, \quad T \propto R^{-2/3}, \quad R > R_s. \tag{2.25}$$

Initial temperature in the source of GRB in thin shell model may be estimated neglecting the baryonic contribution as [82]

$$kT_0 \simeq \left(\frac{3E_0}{4\pi a R_0^3} \right)^{1/4} \simeq 6.5 E_{54}^{1/4} R_8^{-3/4} \text{ MeV}, \tag{2.26}$$

where k is Boltzmann constant, $a = 4\sigma_{SB}/c$, and the last value is obtained for the parametrization $E_0 = 10^{54} E_{54}$ erg and $R_0 = 10^8 R_8$ cm. For the steady wind model analogous expression is

$$kT_0 \simeq \left(\frac{L}{16\pi\sigma_{SB} R_0^2} \right)^{1/4} \simeq 1.2 L_{54}^{1/4} R_8^{-1/2} \text{ MeV}, \tag{2.27}$$

where wind luminosity is parameterized by $L = 10^{54} L_{54}$ erg/s.

2.3 Finite wind model

Consider now a wind with $L = \text{const}, \dot{M} = \text{const}, v_0 = \text{const}, R_0 = \text{const}$ during finite activity time Δt. As follows from Eqs. (2.21) and (2.22), each differential shell originating from the boundary R_0 follows the same expansion law.

In Fig. 2.1 we illustrate the dynamics of the outflow produced by such finite wind. It is clear that when the outflow reaches ultrarelativistic velocities its width is

$$l \simeq c\Delta t. \tag{2.28}$$

Given that the width of the outflow is constant during expansion, baryon conservation implies that laboratory baryon number density $n_{B,l} = \Gamma n_B$ at a given laboratory time should decrease with radius as r^{-2}. Such radial dependence holds both at acceleration and coasting phases, as follows from Eqs. (2.21) and (2.22). Then the dynamics of the laboratory baryon density in the outflow can be represented as

$$n_{B,l} = \begin{cases} n_0 \left(\dfrac{R_0}{r}\right)^2, & R(t) < r < R(t) + l, \\ \\ 0, & \text{otherwise}, \end{cases} \tag{2.29}$$

where $R(t)$ is the radial position of the inner boundary of the outflow, $R(t) + l$ is the radial position of the outer boundary of the outflow. The equation of motion $R(t)$ at the accelerating phase is determined from Eq. (2.21) as

$$R(t) = \sqrt{c^2 t^2 + R_0^2}, \qquad 0 \leq t \leq \sqrt{B^{-2} - 1}\, R_0/c, \tag{2.30}$$

and at the coasting phase from Eq. (2.22) it becomes

$$R(t) = \sqrt{1 - B^2}\, ct + BR_0, \qquad t > \sqrt{B^{-2} - 1}\, R_0/c. \tag{2.31}$$

For $R \gg l$ all the hydrodynamic variables across such outflow with constant $L, \dot{M}$, and v_{ej} do not deviate strongly from their average values, as follows from

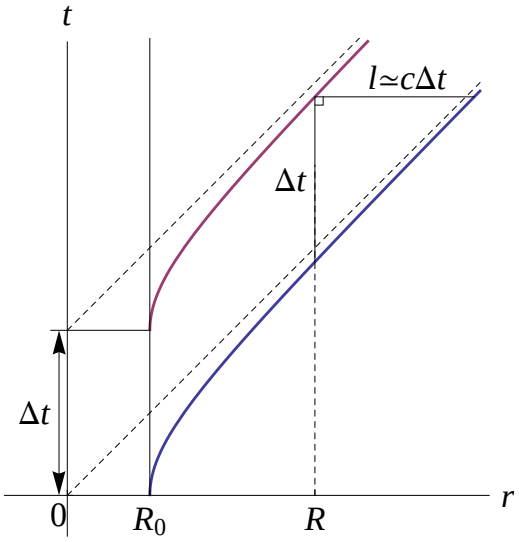

Figure 2.1: Dynamics for finite wind with $B \ll 1$. Solid lines represent world lines of first and last differential shells of the outflow from wind of duration Δt. Dashed lines are asymptotes of these world lines. In the ultrarelativistic regime, when the inner boundary of the outflow is far from the origin, $R(t) \gg R_0$, its width is $l \simeq c\Delta t$.

Eqs. (2.21, 2.22). For this reason both finite wind and averaged shell formulations of initial and boundary conditions produce for $R \gg l$ equivalent outflows, e.g. [3, 7]. In particular, finite wind of duration Δt and constant L and $\dot{M}$ produces the same outflow as averaged shell with

$$E_0 = L\Delta t, \qquad M = \dot{M}\Delta t. \tag{2.32}$$

Clearly, the model of stationary infinite wind can also be obtained in this model with $\Delta t \to \infty$.

2.4 Hydrodynamical spreading

The hydrodynamical mechanism of spreading for ultrarelativistically expanding shell was considered in [32, 33]. As follows from Eq. (2.22) at the matter dominated phase of expansion each differential subshell is moving with almost constant speed $v \simeq c(1 - 1/2\Gamma^2)$, so the spreading of the shell is determined by the radial dependence of the Lorentz factor $\Gamma(r)$. In a variable outflow there can be regions with $\Gamma(r)$ decreasing with radius and $\Gamma(r)$ increasing with ra-

dius. At sufficiently large radii only the regions with increasing Γ contribute to the spreading of the outflow. From equations of motion of external and internal boundaries of this region we obtain the thickness of the region as function of radial position of the region

$$l(R) = l + \frac{R}{2}\left(\frac{1}{\Gamma_i^2} - \frac{1}{\Gamma_e^2}\right), \tag{2.33}$$

where Γ_e and Γ_i are Lorentz factors at external and internal boundaries, l is the width of the region at small R. Let us consider such a region in two limiting cases: a) when relative Lorentz factor difference is strong, $\Gamma_e \gg \Gamma_i$; and b) when relative Lorentz factor difference is weak $\Delta\Gamma = \Gamma_e - \Gamma_i \ll \Gamma_i$.

In case a) the second term in parenthesis in Eq. (2.33) can be neglected, and we obtain that the spreading becomes efficient at $R > R_b$, defined in Eq. (2.12) with $\Gamma = \Gamma_i$, see [32, 33]. In case b) we find the corresponding critical radius of hydrodynamic spreading $R_b = \Gamma_i^2 l \frac{\Gamma_i}{\Delta\Gamma} \gg \Gamma_i^2 l$. Notice that in the finite wind model there is no hydrodynamical spreading.

Note that Eq. (2.22) has been derived under the assumptions of no spreading. Here we derive the corresponding relations assuming strong relative Lorentz factor difference across the outflow in the sense defined above. Let us take an element of fluid with constant number of particles dN in the part of the outflow with gradient of Γ. Internal boundary of the element is moving with velocity v, and external is moving with velocity $v + dv = v + \frac{dv}{dr}dr$, where dr is the differential thickness at some fixed laboratory time $t = 0$ and derivative $\frac{dv}{dr}$ is taken at the same time. Then at time t the width of the element is $dl = dr + tdv$, its radial position is $R(t) = r_0 + vt$ and corresponding laboratory density is

$$n_{B,l} = \frac{dN}{dV} = \frac{dN}{4\pi R^2\left(1 + t\frac{dv}{dr}\right)dr} = n_0\frac{r_0^2}{R^2\left(1 + t\frac{dv}{dr}\right)}, \tag{2.34}$$

where $n_0 = \frac{dN}{dV_0} = \frac{dN}{4\pi r_0^2 dr}$. At large enough t using $R \simeq ct$ we have from Eqs. (2.20)

$$n_{B,l} \propto R^{-3}, \qquad T \propto R^{-1}, \qquad R \gg R_b = \frac{1}{\Gamma^3}\left(\frac{d\Gamma}{dr}\right)^{-1}. \tag{2.35}$$

2.5 Thermal spreading

We now determine the velocity spread of particles as a function of comoving temperature T and bulk Lorentz factor Γ for relativistic Maxwellian distribution. Such spread of particles lead to spreading of expanding plasma with arbitrary $\Gamma(r,t)$, in both wind and shell models. Based on this result we compute the value of thermal spreading for expanding shell.

We assume that each layer of the expanding shell is in local thermodynamical equilibrium. It is a reasonable assumption for the hydrodynamic phase of expansion due to large optical depth of the shell. Then the distribution of particles in the momentum space $\mathbf{p}' = (p'_x, p'_y, p'_z)$ in the rest frame of plasma is given by relativistic relativistic Maxwellian, obtained by Jüttner [87]

$$f(p'_x, p'_y, p'_z) = A \exp\left[-\frac{1}{\theta}\sqrt{1+\left(\frac{\mathbf{p}'}{mc}\right)^2}\right], \tag{2.36}$$

where A is a normalization constant determined by the particle density, $\theta = \frac{kT}{mc^2}$ is the dimensionless temperature, m is the mass of particles, c is the speed of light, T is the local temperature and k is Boltzmann constant. Then in the laboratory frame this distribution will be transformed to the Lorentz-boosted relativistic Maxwellian

$$f(p_x, p_y, p_z) = A \exp\Bigg(-\frac{1}{mc\theta}\Big[m^2c^2 + {p_y}^2 + {p_z}^2 + \left(\Gamma p_x - \sqrt{(\Gamma^2-1)(m^2c^2+\mathbf{p}^2)}\right)^2\Big]^{1/2}\Bigg), \tag{2.37}$$

where we assumed that the relative motion of the frames is along their x-axes.

Velocity dispersion in the x-direction is

$$D(v_x) = M(v_x^2) - M^2(v_x), \tag{2.38}$$

where $M(\chi)$ denotes the average value of χ, which is defined by the convolution

with the distribution function (2.37)

$$M(\chi) = \frac{\int d^3\mathbf{p}\,\chi(\mathbf{p})f(\mathbf{p})}{\int d^3\mathbf{p}\,f(\mathbf{p})}. \tag{2.39}$$

The above written integrals cannot be computed analytically, but their numerical approximations can be found after the following convenient change of variables

$$p_x = mc\,p_r,\ p_y = mc\,p_p\cos\phi,\ p_z = mc\,p_p\sin\phi, \tag{2.40}$$

so that for χ with axial symmetry around x-axis

$$M(\chi) = \frac{\int dp_r \int dp_p\,\chi(p_r,p_p)\exp\left[-g(p_r,p_p)/\theta\right]}{\int dp_r \int dp_p\,\exp\left[-g(p_r,p_p)/\theta\right]}, \tag{2.41}$$

where

$$g(p_r,p_p) = \sqrt{1+(\Gamma p_r - \sqrt{\Gamma^2-1}\sqrt{1+p_r^2+p_p^2})^2+p_p^2}$$

and limits of integration are taken from $-\infty$ to $+\infty$ for p_r and from 0 to $+\infty$ for p_p.

Numerical issues in the velocity dispersion calculations by (2.38) arise from the fact that for high Γ we need to subtract two numbers $M(v^2)$ and $M^2(v)$ which are very close to each other and to c^2. This leads to substantial reduction of accuracy. A different formula for dispersion

$$D(v_x) = M([v_x - M(v_x)]^2) \tag{2.42}$$

proves to be more convenient. The spread of particle velocities is then

$$(\Delta v)_{therm} = \sqrt{D(v)}. \tag{2.43}$$

Results of the numerical integration are illustrated in Figures 2.2–2.4. For

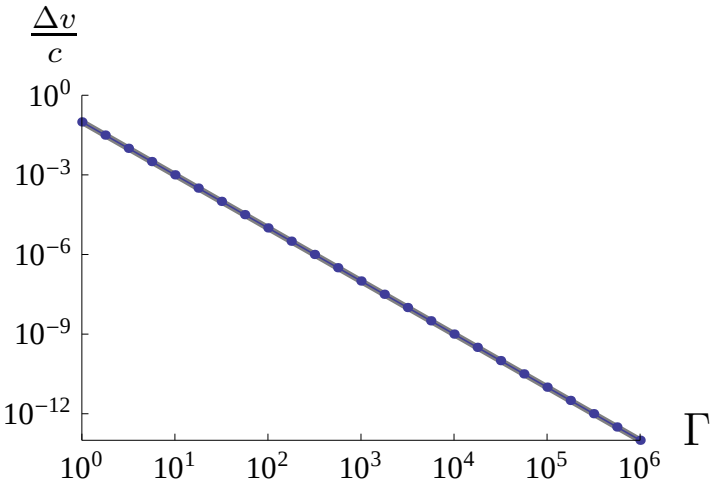

Figure 2.2: The velocity dispersion along the direction of bulk motion for nonrelativistic comoving temperature $\theta = 10^{-2}$ shown as a function of the bulk Lorentz factor. Thick gray line is the asymptotic value (2.44).

nonrelativistic comoving temperatures the correct asymptotics is, see Fig. 2.2

$$\left(\frac{\Delta v}{c}\right)_{\theta\ll 1} = \Gamma^{-2}\theta^{1/2}, \tag{2.44}$$

but not $\Delta v/c = \Gamma^{-2}$ assumed in [32]. This behavior can be understood easily with the following argument: when the initial spread of velocities is small compared to the bulk velocity V, then by the velocity transformation formula we can approximate the new spread as

$$\Delta v \simeq \Delta v' \left.\frac{d}{dv'}\frac{V+v'}{1+\frac{Vv'}{c^2}}\right|_{v'=0} = \Delta v'\left(1-\frac{V^2}{c^2}\right), \tag{2.45}$$

that gives us exactly the result obtained numerically.

The case of ultrarelativistic comoving temperature ($\theta \gg 1$) is more interesting. Starting close to the maximal value $1/\sqrt{2}$, the velocity spread for $10 \lesssim \Gamma \lesssim \theta$ reaches approximately, see Fig. 2.3

$$\left(\frac{\Delta v}{c}\right)_{10\lesssim\Gamma\lesssim\theta} \simeq \Gamma^{-3/2}, \tag{2.46}$$

which means that the dispersion is independent on the temperature. For $\Gamma \gg \theta$

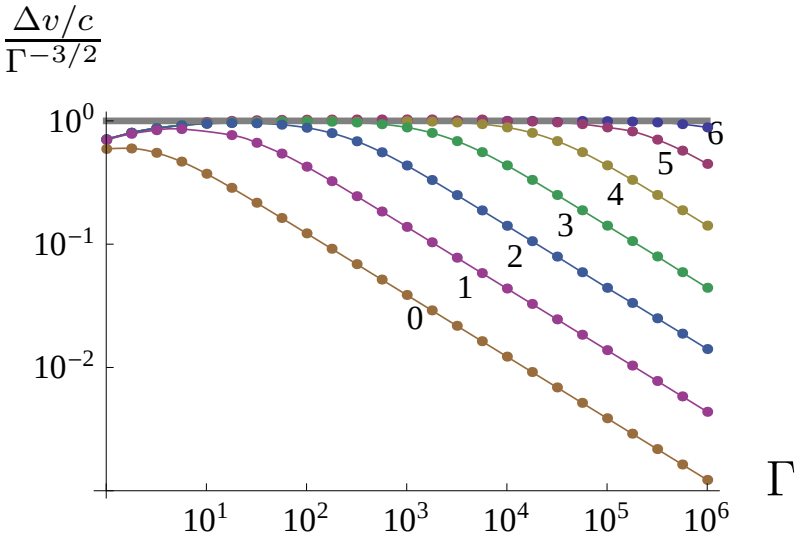

Figure 2.3: The velocity dispersion along the direction of bulk motion for highly relativistic comoving temperature as a function of the bulk Lorentz factor in intermediate regime. Seven sets of dots presented on the figure correspond to values of $\log\theta$ from 0 (lowest curve) to 6 (highest curve) in steps of 1. Thick gray line is the asymptotic value (2.46).

the asymptotics (2.44) is restored just up to a multiplier close to unity, see Fig. 2.4

$$\left(\frac{\Delta v}{c}\right)_{1\ll\theta\ll\Gamma} \simeq 1.16\,\Gamma^{-2}\theta^{1/2}. \tag{2.47}$$

Our results suggest that (2.46) gives absolute upper limit for the velocity spread, and temperature dependence of (2.44) and (2.47) reduce the spread even further.

2.6 Implications of thermal spreading for GRBs

In particular, Eqs. (2.26, 2.27) show that initial temperatures of GRB sources ban be both relativistic or non relativistic for electrons, but for protons it is always nonrelativistic $kT_0 \ll m_p c^2$. At both radiation and matter dominated phases the comoving temperature of the plasma decreases. Now we compute the thermal spreading at both phases.

For the acceleration phase due to the nature of Lorentz transformations in

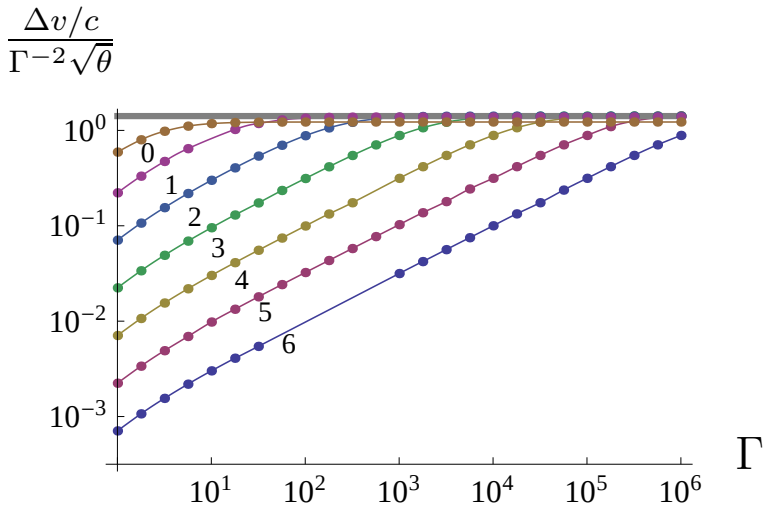

Figure 2.4: The velocity dispersion along the direction of bulk motion for highly relativistic comoving temperature as a function of the bulk Lorentz factor in high-Γ regime. Seven sets of dots presented on the figure correspond to values of $\log\theta$ from 0 (highest curve) to 6 (lowest curve) in steps of 1. Thick gray line is the asymptotic value (2.47).

constantly accelerated frame the final spreading of the shell in laboratory frame $\Delta l_1 = \int_0^t \Delta v\, dt$ appears to be finite even if we extend this phase infinitely in time, and the main part of the spreading is connected with initial part of motion with relatively small Γ. Velocity spread is given by Eq. (2.44) and in energy dominated phase the spreading is

$$\frac{\Delta l_1}{R_0} \lesssim 2.2\sqrt{\frac{kT_0}{m_p c^2}} = 0.18\, E_{54}^{1/8}\, R_8^{-3/8}. \tag{2.48}$$

In the matter dominated phase the additional spreading of the shell at radius $\mathcal{R}$ is

$$\frac{\Delta l_2}{R_0} \simeq 3B^{7/3}\sqrt{\frac{kT_0}{m_p c^2}}\left(\frac{\mathcal{R}}{R_0}\right)^{1/3} = 5.3\cdot 10^{-6}\, E_{54}^{1/8}\, R_8^{-17/24}\, B_{-2}^{7/3}\, \mathcal{R}_8^{1/3}, \tag{2.49}$$

when $\mathcal{R} \gg B^{-1}R_0$. Comparing to the hydrodynamical spreading for reasonable GRB parameters the spreading coming from both (2.48) and (2.49) is negligible.

Note that velocity dispersion in any case does not exceed the value given

by Eq. (2.46) with $\theta \gg 1$ and this gives an absolute maximum of the thermal spreading on the radiation dominated phase

$$\frac{\Delta l_1}{R_0} = \frac{1}{R_0}\int_0^{t_1} \Delta v(t)dt \lesssim \frac{1}{R_0}\int_0^{\infty} c\Gamma(t)^{-3/2}dt \simeq 2.6. \tag{2.50}$$

2.7 Conclusions

In this Chapter we presented a brief overview of relativistic hydrodynamics of GRB paying special attention to the formulation of initial and boundary conditions. We also considered two mechanisms of spreading of relativistically expanding shell.

Considering initial and boundary conditions giving rise to wind and thin shell models we find that their dynamics is similar in the ultrarelativistic limit $\Gamma \gg 1$ and $R \gg l$. Then, following the proposal of [33], we estimated hydrodynamical spreading of relativistically expanding shell.

We also considered thermal spreading. Assuming relativistic Maxwellian distribution function for electrons and baryons we determined the velocity dispersion depending on the temperature and the Lorentz factor of the bulk motion. We then applied these results to GRBs and showed that thermal spreading provides negligible spreading for realistic parameters of GRBs.

Chapter 3

Optical depth of relativistically moving medium

In this Chapter we compute the optical depth of photon scattering in relativistically moving medium and apply the results to GRB outflows. This problem finds applications in theory of GRB photospheric emission and we discuss such applications in Chapter 4.

It is well known that optical depth τ is relativistic invariant, see e.g. [61, Sec. 4.9]. However, in concrete physical situation the choice of particular reference frame where the calculations are performed is dictated by physical conditions. It is also instructive to demonstrate on simple analytic examples the invariance of optical depth.

We begin with the general definition of optical depth and its representation in manifestly covariant 4-dimensional form by Ehlers [65, p. 76–77], see Sec. 3.1. Then we calculate the optical depth of relativistically moving slab in Sec. 3.2, and of spherically symmetric matter distributions, see Sections 3.3–3.7. Finally, optical depth and transparency radius of the outflows in baryonic thermally accelerated models of GRBs, such as fireball [7] and fireshell [75], is computed in Sections 3.8–3.10. A survey of the literature and comparison with previous results is given in Sec. 3.11. Conclusions follow.

3.1 Definition of the optical depth

Take a light ray in the medium. It follows a light-like world line. Optical depth on the world line from one space-time point A to another space-time point B is

defined (see e.g. [61, Eqs. (1.25), (1.26)]) by the following formula

$$\tau_{AB} = -\ln \frac{N_B}{N_A}, \tag{3.1}$$

where N_A and N_B are the numbers of photons emitted at point A and received at point B, respectively.

As it is shown by Ehlers [65, p. 76–77], the optical depth along the ray with the world line $\mathcal{L}$ from space-time point A to space-time point B in a medium with nonrelativistic comoving temperature is a curvilinear integral

$$\tau_{AB} = -\int_{\mathcal{L}_{AB}} \sigma n_c u_\mu dx^\mu = -\int_{\mathcal{L}_{AB}} \sigma j_\mu dx^\mu, \tag{3.2}$$

where we used Einstein summation rule and $(-,+,+,+)$ metric signature, σ is invariant scattering cross-section, i.e. cross section measured in the system comoving with the medium, u^μ and $j^\mu = n_c u^\mu$ are respectively 4-velocity and 4-current of the medium, n_c is its comoving number density, dx^μ is the world line element along the ray. In all Chapter we assume $\sigma = \text{const}$ which is the case of Thomson scattering, relevant for determination of the photospheric emission of GRBs.

For hydrodynamic models considered in Chapter 2, the integral for optical depth (3.2) has its simplest form in the laboratory reference frame. For this reason in all Chapter we adopt this reference frame, if not specified otherwise. We assume Minkowski space-time and use subscripts "c" and "l" referring respectively to comoving and laboratory reference frames. When it does not lead to confusion, index "l" is omitted for simplification of notation. 3-dimensional vectors are denoted by bold letters.

In a given laboratory frame with coordinates $(ct, \mathbf{r})$ we have

$$u^\mu = \Gamma(1, \boldsymbol{\beta}), \qquad j^\mu = n_c \Gamma(1, \boldsymbol{\beta}) = n_l (1, \boldsymbol{\beta}), \tag{3.3}$$

where $\mathbf{v} = \boldsymbol{\beta} c$ is 3-velocity of the medium in laboratory frame, $\Gamma = (1 - \beta^2)^{-1/2}$ is Lorentz factor, n_l is laboratory density of the medium. The element of the ray world line in this reference frame, parameterized by time t or by length along

the ray ζ is

$$dx^\mu = cdt\,(1, \boldsymbol{\mu}) = d\zeta\,(1, \boldsymbol{\mu})\,, \tag{3.4}$$

where $\boldsymbol{\mu}$ is the unit vector in the 3-direction of the ray, $|\boldsymbol{\mu}| = 1$, and $d\zeta = cdt$ is the spatial length of the element.

Then the integral (3.2) in laboratory reference frame is

$$\tau_{AB} = \int_{\zeta_A}^{\zeta_B} \sigma n_c \Gamma (1 - \boldsymbol{\beta} \cdot \boldsymbol{\mu}) d\zeta = \int_{\zeta_A}^{\zeta_B} \sigma n_l (1 - \boldsymbol{\beta} \cdot \boldsymbol{\mu}) d\zeta, \tag{3.5}$$

where ζ_A and ζ_B correspond to space-time points A and B, respectively, and a dot denotes scalar product of 3-vectors. This expression is also in agreement with transformation laws for opacity κ, in particular, it is equivalent to Eq. (4.112) of the textbook [61], if we take into account the Doppler effect, their Eq. (4.11). It is also the same as Eq. (90.8) of the textbook [88], where the Doppler effect is given by Eq. (89.5).

It should be noted that optical depth is a two-point function which depends both on locations of event A and event B, as it clearly follows from Eqs. (3.2) and (3.5). Only if one of these points is fixed, for example, at infinity, then τ becomes a one-point function.

3.2 Optical depth of a slab in planar geometry

In order to clarify the physical meaning of the expression (3.5) it is instructive to make explicit calculation of optical depth in some simple model. Consider a slab with constant comoving density n_c moving along x-axis, and a ray of photons, crossing the slab in both directions parallel and antiparallel to this axis. Space-time diagrams of the events in comoving and laboratory frame are shown on Fig. 3.1.

Spatial lengths of both world lines AB and BC in comoving frame are equal to the width of the slab in this frame $L^c_{AB} = L^c_{BC} = l_c$. The optical depth in this frame is

$$\tau_{AB} = \tau_{BC} = \int_0^{l_c} \sigma n_c d\zeta_c = \sigma n_c l_c. \tag{3.6}$$

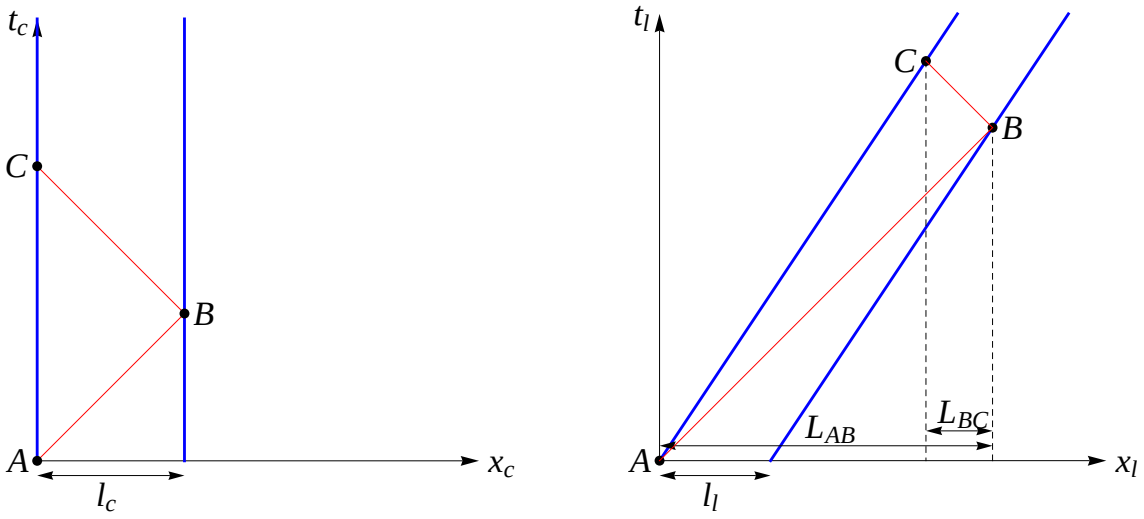

Figure 3.1: Space-time diagram of ray propagation through the slab in comoving (left) and laboratory (right) frame. Scale is the same on both figures, $\beta = 2/3$.

In laboratory frame the length of the ray inside the slab in forward direction is affected by two factors: firstly, it is increased with respect to path in comoving frame by a factor of $1/(1-\beta)$. This is purely kinematical effect, that has direct analogy in nonrelativistic case. Secondly, the path is decreased due to Lorentz contraction of the slab by a factor of $1/\Gamma$. The result is

$$L^l_{AB} = \frac{l_c}{\Gamma(1-\beta)} = \frac{l_l}{1-\beta}. \tag{3.7}$$

For the backward motion we have the same Lorentz contraction multiplier $1/\Gamma$, but another kinematical multiplier $1/(1+\beta)$, also reducing the path as

$$L^l_{BC} = \frac{l_c}{\Gamma(1+\beta)} = \frac{l_l}{1+\beta}. \tag{3.8}$$

The optical depth in laboratory frame along the world line AB is

$$\tau_{AB} = \int_{\zeta_{lA}}^{\zeta_{lB}} \sigma n_l (1 - \mathbf{fi}^-) d\zeta_l = \int_0^{L^l_{AB}} \sigma n_l (1-\beta) d\zeta_l$$
$$= \sigma n_l (1-\beta) L^l_{AB} = \sigma n_l l_l = \sigma n_c l_c. \tag{3.9}$$

For the world line BC

$$\tau_{BC} = \int_{\zeta_{lB}}^{\zeta_{lC}} \sigma n_l (1 - \mathbf{fi}^{-}) d\zeta_l = \int_0^{L^l_{BC}} \sigma n_l (1+\beta) d\zeta_l$$
$$= \sigma n_l (1+\beta) L^l_{BC} = \sigma n_l l_l = \sigma n_c l_c. \quad (3.10)$$

This is an expected result: *the optical depth of a slab does not depend on its state of motion*. This can be understood also as constancy of column number density $K = n_c l_c = n_l l_l$ of the slab. Optical depth $\tau = \sigma K$ is equal to the average number of scattering events inside the world tube with cross section area σ along the world line of rays AB or BC. This number does not depend on the choice of reference frame.

3.3 Optical depth of a spherically-symmetric static matter distribution

Before considering the optical depth in hydrodynamic models discussed in Chapter 2, it is also instructive to calculate the optical depth in the case when density of medium n_l is not a constant along the ray. For illustration take a spherically-symmetric *static* distribution of matter with number density

$$n_l(r) = n_0 \left(\frac{R_0}{r}\right)^2 \quad (3.11)$$

extended from radius R to radius $R + l$, i.e. a static shell. Total number of particles in the shell N does not depend on parameter R

$$N = \int_R^{R+l} n_0 \left(\frac{R_0}{r}\right)^2 4\pi r^2 dr = 4\pi n_0 R_0^2 l. \quad (3.12)$$

However, optical depth (3.5) of this shell in radial direction depends on R

$$\tau = \int_R^{R+l} \sigma n_0 \left(\frac{R_0}{r}\right)^2 dr = \tau_0 R_0 \left(\frac{1}{R} - \frac{1}{R+l}\right), \quad (3.13)$$

where we have introduced the parameter

$$\tau_0 = \sigma n_0 R_0. \tag{3.14}$$

The optical depth has two asymptotic limits: in the case of geometrically thick shell $l \gg R$ second term in parenthesis $(R+l)^{-1}$ can be neglected and optical depth becomes the same as in the case of infinite distribution of matter with $l \to \infty$

$$\tau_{thick} = \tau_0 \frac{R_0}{R}, \qquad l \gg R. \tag{3.15}$$

In the case of geometrically thin shell $l \ll R$ we can expand Eq. (3.13) into a series in small parameter l/R and the first term of the series gives

$$\tau_{thin} = \tau_0 \frac{R_0 l}{R^2}, \qquad l \ll R. \tag{3.16}$$

This expression is the same as in the slab case, because in this case $\tau = \sigma n(R) l$, cf. Eq. (3.9), and it is valid as far as the contrast of density n, given by (3.11), along the ray

$$\frac{\Delta n}{n} = \frac{n(R+l) - n(R)}{n(R)} = 1 - \left(\frac{R}{R+l}\right)^2 \tag{3.17}$$

is small. In this respect the shell far from the origin becomes more and more "slab-like". If density contrast is not small, then exact expression for optical depth (3.13) should be used. Range of applicability of derived asymptotics is illustrated in Fig. 3.2.

3.4 Optical depth of a spherically-symmetric moving matter distribution, computed in laboratory frame

In this section we compute the optical depth of the expanding outflow corresponding to the finite wind model introduced in Sec. 2.3.

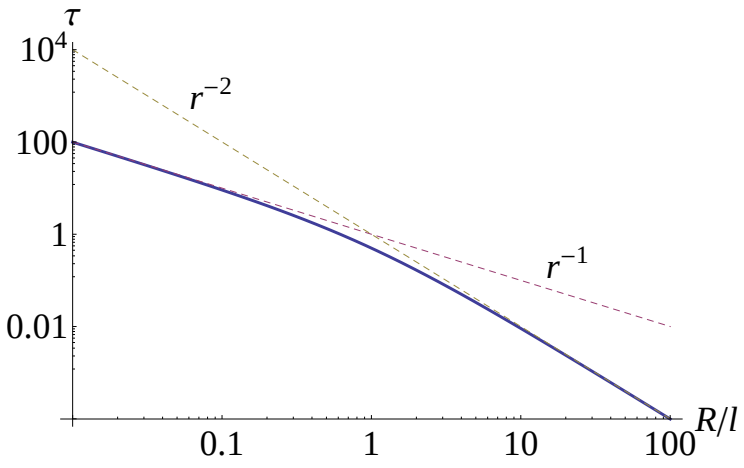

Figure 3.2: Optical depth of a static shell (3.13) as a function of ratio of shell internal radius R to shell width l (solid curve). Asymptotics (3.15) and (3.16) are shown by dashed lines.

3.4.1 Coasting phase

Unlike the previous case of static shell with $R = \text{const}$ as a parameter, this expanding outflow runs through different $R(t)$ in the course of time. We compute the optical depth of the entire outflow (2.29) evaluating integral (3.5) starting from the inner radius R up to the radius $R + L^l_{AB}$ given by Eq. (3.7), namely

$$\tau = \int_R^{R+\frac{l}{1-\beta}} \sigma n_0 \left(\frac{R_0}{r}\right)^2 (1-\beta) dr = \tau_0 R_0 (1-\beta) \left(\frac{1}{R} - \frac{1}{R+\frac{l}{1-\beta}}\right). \qquad (3.18)$$

This expression reduces to Eq. (3.13) for static shell $\beta = 0$.

Again we recover two asymptotic cases. If the outflow is thick enough, we have

$$\tau_{thick} = \tau_0 (1-\beta) \frac{R_0}{R}, \qquad l \gg R(1-\beta). \qquad (3.19)$$

In opposite case of thin outflow we arrive to

$$\tau_{thin} = \tau_0 \frac{R_0 l}{R^2}, \qquad l \ll R(1-\beta), \qquad (3.20)$$

that is equal to the optical depth of static thin shell (3.16). Since $R(t)$ is monotonically increasing with time, the approximation (3.19) becomes invalid at certain

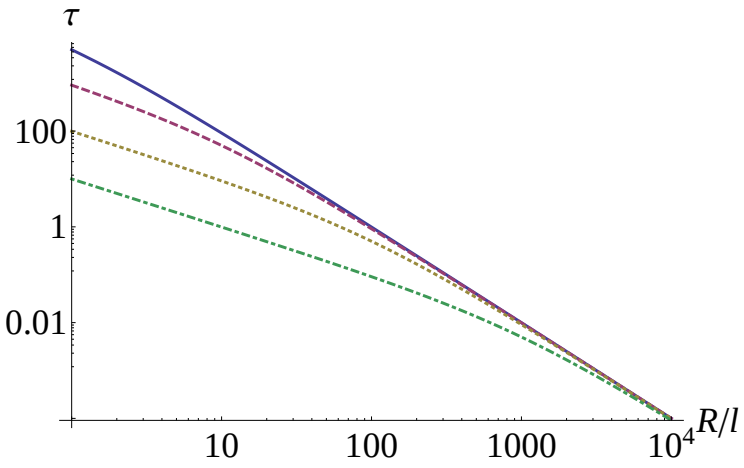

Figure 3.3: Optical depth of a moving outflow (3.18) as a function of ratio of its internal radius R to its width l for different velocities: $\beta = 0$ (static shell, solid curve), $\beta = 0.9$ (dashed curve), $\beta = 0.99$ (dotted curve), $\beta = 0.999$ (dotted–dashed curve). Far enough from the origin all curves approach the asymptotic (3.20).

radius R_t. For larger radii it should be substituted by approximation (3.20) as can be seen clearly from Fig. 3.3. The radius of transition between this two asymptotic solutions is given by

$$R_t = \frac{l}{1-\beta} \simeq 2\Gamma^2 l, \tag{3.21}$$

where the last relation holds in the ultrarelativistic case with $\Gamma \gg 1$. Notice the coincidence of R_t and R_b defined in Eq. (2.12).

Unlike geometrical thickness $l \gg R$ in (3.15) and thinness $l \ll R$ in (3.16) criteria in the static case, in the case of expanding outflow different criteria appear: respectively $l \gg R(1-\beta)$ in (3.19) and $l \ll R(1-\beta)$ in (3.20). For this reason we have introduced the terms *photon thick* and *photon thin* outflows, respectively, in [89].

We can say then that the optical depth of an expanding spherical outflow in general case depends on its velocity as a parameter, in contrast to the case of a moving slab in plane geometry, cf. Eq. (3.15) and Eq. (3.19).

3.4.2 Accelerating phase

Now let us treat the case of accelerating outflow taking again the model of a finite wind, described by Eqs. (2.21) and (2.29) of Sec. 2.3.

The world line of any differential shell with increasing time tends to light-like line, and laboratory distance between a differential shell and the pure light like world line starting radially at some time t_e, has a finite limit in a constantly accelerating case, namely

$$\Delta r_{lim}(t_e) = \lim_{t\to\infty} r(t_e) + c(t - t_e) - r(t) \\ = \sqrt{c^2(t_e - t_0)^2 + R_0^2} - c(t_e - t_0) \leq R_0. \quad (3.22)$$

This effect is analogous to the effect of Rindler horizon for observer with constant proper acceleration, e.g. [90].

For our purposes it means that if the outflow is thick enough $l > \Delta r_{lim}(t_e)$, then light ray from its inner boundary never crosses its outer boundary during acceleration. This is the only case of astrophysical interest, because the width of outflow in GRBs is at least of order R_0, see Chapter 2. In this case integration in optical depth should be extended to infinity, and hence we find that *the accelerating outflow is always photon thick*. Assuming $\Gamma(t) \gg 1$, from Eq. (3.5) optical depth of the outflow (2.29) for a ray emitted from its inner boundary is

$$\tau \simeq \int_R^\infty \sigma n_0 \left(\frac{R_0}{r}\right)^2 \frac{R_0^2}{2r^2} dr = \frac{\tau_0}{6}\frac{R_0^3}{R^3}. \quad (3.23)$$

Note that in accelerating phase optical depth decreases with radius even faster than it does in coasting phase.

3.5 Optical depth of spherical outflow with constant density profile computed in laboratory frame

In this section we calculate optical depth for the average shell model, defined in the Sec. 2.2. In that model the laboratory density of the outflow at a given laboratory time does not depend on radial coordinate $n_l(r,t)|_{t=\text{const}} = \text{const}$. For simplicity we assume that the radial velocity of expansion is constant $v = \beta c$.

Equations of motion of outflow inner boundary $r_i(t)$ and of outflow outer boundary $r_o(t)$ are

$$r_i(t) = vt, \qquad r_o(t) = vt + l, \tag{3.24}$$

respectively, so that l is laboratory width of the outflow. The laboratory volume of the outflow is

$$V(t) = \frac{4}{3}\pi\left[(l+vt)^3 - (vt)^3\right] = \frac{4}{3}\pi\left[l^3 + 3l^2vt + 3l(vt)^2\right], \tag{3.25}$$

and laboratory density of the outflow n_l is

$$n_l = \frac{N}{V(t)}, \tag{3.26}$$

where $N = \text{const}$ is the total number of particles, on which photon scatters.

Approximation of constant density along the ray is good when the density changes slowly on the ray world line, namely $\left|\frac{1}{n}\frac{dn}{dt}\right| \Delta t \ll 1$, where $\Delta t = \frac{l}{c(1-\beta)}$ is the time during which light cross the shell. From Eqs. (3.25) and (3.26) it follows that this condition is

$$F = \left|\frac{1}{n}\frac{dn}{dt}\right| \frac{l}{c(1-\beta)} = \frac{3\beta}{1-\beta}\frac{l^3 + 2l^2vt}{l^3 + 3l^2vt + 3l(vt)^2} \ll 1. \tag{3.27}$$

It is clear that $F(t)$ monotonically decreases with time. When t changes from 0 to infinity, $F(t)$ decreases from $\frac{3\beta}{1-\beta}$ to zero. Then we have two different cases:

- For $\beta < 1/4$ we have $F < 1$ always and density contrast along the ray is small. We can say that in such case the "slab-like" approximation of constant n_l is reasonable, and the optical depth is given by the integral (3.9).

- For $\beta > 1/4$ F can be either larger than 1 or smaller than 1. We can define

$$t^* = \frac{l_c}{v}\frac{9\beta - 3 + \sqrt{33\beta^2 + 6\beta - 3}}{6(1-\beta)} < \frac{2l}{c(1-\beta)} \tag{3.28}$$

  such as $F(t^*) = 1$, then for $t \gg t^*$ the "slab-like" approximation (3.9) should be valid. From Eq. (3.28) we find that $r_i \gg \Gamma^2 l$ in this case, that is exactly our photon thin region (3.20).

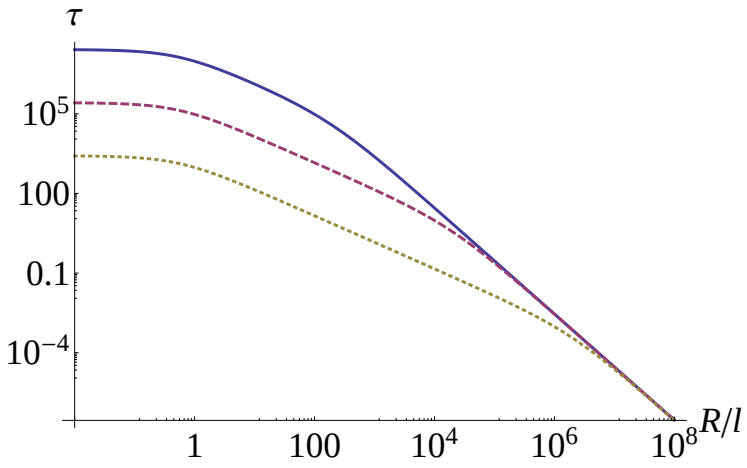

Figure 3.4: Optical depth of the outflow with density, constant in laboratory frame, as function of radius of emission R. Curves from top to bottom correspond to $\Gamma = 10$ (solid), $\Gamma = 100$ (dashed), and $\Gamma = 1000$ (dotted), respectively. Two transition regions at $R \sim l$ and $R \sim \Gamma^2 l$ are clearly visible.

Optical depth for a ray crossing the outflow radially from inner boundary at radius R is

$$\begin{aligned}\tau &= \int_R^{R+\frac{l}{1-\beta}} \sigma \frac{3N}{4\pi\left[l^3 + 3l^2 vt + 3l(vt)^2\right]}(1-\beta)dr \\ &= \frac{(1-\beta)\sigma N\sqrt{3}}{2\pi l^2 \beta}\left\{\tan^{-1}\frac{\sqrt{3}\left[l + 2\left(R + \frac{\beta l}{1-\beta}\right)\right]}{l} - \tan^{-1}\frac{\sqrt{3}[l+2R]}{l}\right\}, \quad (3.29)\end{aligned}$$

where we used the fact that on the world line of the ray $t = R/v + (r-R)/c$, as follows from Eq. (3.24). Evolution of optical depth is illustrated by Fig. 3.4 and has three asymptotics:

- For $l \gg R$, that corresponds to geometrically thick outflow, the optical depth is nearly constant. However this case is not relevant for thermally accelerating GRB models because outflow should be accelerating in these radii.

- For $l \ll R \ll \frac{\beta l}{1-\beta}$, that corresponds to geometrically thin outflow in the photon thick regime, the optical depth is inversely proportional to R, $\tau \simeq \frac{N\sigma(1-\beta)}{4\pi l \beta R}$, cf. Eq. (3.19).

- For $R \gg \frac{\beta l}{1-\beta}$, that corresponds to geometrically thin and photon thin out-

flow, the optical depth is proportional to R^{-2} and does not depend on outflow velocity, $\tau \simeq \frac{N\sigma}{4\pi R^2}$, cf. Eq. (3.20).

We come to conclusion that *the optical depth of geometrically thin outflow of constant laboratory density, $n_l(r,t)|_{t=\text{const}} = \text{const}$ across the outflow, follows the same law as in the case of the outflow with density profile $n \propto r^{-2}$, considered in Sec. 3.4.*

3.6 Optical depth of a radially spreading relativistic outflow

In previous sections we assumed that the Lorentz factor inside the outflow is constant and hence neglected the hydrodynamical spreading phenomena discussed in Sec. 2.4. In this section following [91] we consider the limiting case of strong hydrodynamical spreading, namely case a) of Sec. 2.4. As it was shown there, at sufficiently large radii the laboratory density is described by Eq. (2.34).

Taking into account hydrodynamical spreading (2.33) we obtain for the baryonic density along the light ray the following expression

$$n = n_0 \left(\frac{R_0}{r}\right)^2 \frac{1}{1 + \frac{2r}{\Gamma}\frac{d\Gamma}{dr}}, \tag{3.30}$$

that is exact in ultrarelativistic limit. Notice the difference between Eq. (3.30) and Eq. (2.34): in the former case $d\Gamma/dr$ is computed along the light ray, while in the latter case dv/dr is computed along the radial coordinate at fixed laboratory time. This expression reduces to Eq. (2.22) when $d\Gamma/dr = 0$. Instead when the second term in the denominator of the Eq. (3.30) dominates, namely when $r \gg \Gamma(d\Gamma/dr)^{-1}$, density radial dependence coincides with the one given by Eq. (2.35).

An estimate for $d\Gamma/dr$ can be given for strong relative Lorentz factor difference in the outflow

$$\frac{d\Gamma}{dr} \sim \frac{\Delta\Gamma}{\Delta r} \sim \frac{\Gamma}{2\Gamma^2 l} = \frac{1}{2\Gamma l}, \tag{3.31}$$

where $\Delta r \sim 2\Gamma^2 l$ is the distance inside the outflow along the light ray and $\Delta\Gamma \sim \Gamma$. Integrating expression (3.31) we obtain Lorentz factor dependence on radial

coordinate for the case of strong relative Lorentz factor difference as

$$\Gamma(r) = \sqrt{\frac{r-R}{l}}. \tag{3.32}$$

Then from Eq. (3.5) we have the integral

$$\tau = \tau_0 \int_R^{R+\Delta r} \left(\frac{R_0}{r}\right)^2 \frac{1}{1+\frac{2r}{\Gamma}\frac{d\Gamma}{dr}} \frac{1}{2\Gamma^2} dr. \tag{3.33}$$

Since we are interested in the asymptotics when the hydrodynamic spreading is essential, we can assume in the integral $r \gg R$ and $\Delta r \gg R$. Under these conditions the optical depth is

$$\tau = \frac{\tau_0}{8} \frac{R_0 l}{R^2}. \tag{3.34}$$

This result coincides with Eq. (3.20) up to a numerical factor. However its physical meaning is different. It represents photon thick asymptotic case, because $\Delta r \gg R$ in Eq. (3.33).

We conclude that photon thin asymptotics exists only in relativistic outflows with small variations of the Lorentz factor in coasting phase in the sense defined in the case b) of Sec. 2.4.

3.7 Optical depth of spherical outflow with constant density profile computed in comoving frame

In the literature another approach to optical depth calculation, based on comoving rate of photon scattering is used frequently in analogy with cosmology, see e.g. [12]. In the thin shell model [32, 33] recalled in Sec. 2.2, the comoving thickness of relativistically expanding shell is

$$l_c = \begin{cases} R = R_0\Gamma, & R < B^{-1}R_0, \\ B^{-1}R_0, & B^{-1}R_0 < R < B^{-2}R_0, \\ BR, & R > B^{-2}R_0, \end{cases} \tag{3.35}$$

where B is the baryonic loading (2.3).

The corresponding comoving volume for fixed laboratory time is then [32]

$$V_c = 4\pi R^2 l_c = \begin{cases} 4\pi R^3, & R < B^{-1}R_0, \\ 4\pi B^{-1} R_0 R^2, & B^{-1}R_0 < R < B^{-2}R_0, \\ 4\pi B R^3, & R > B^{-2}R_0. \end{cases} \tag{3.36}$$

Baryon number conservation

$$n_c V_c = \text{const} = 4\pi R_0^3 n_0, \tag{3.37}$$

implies

$$n_c = \begin{cases} n_0 \left(\frac{R}{R_0}\right)^{-3}, & R < B^{-1}R_0, \\ n_0 B \left(\frac{R}{R_0}\right)^{-2}, & B^{-1}R_0 < R < B^{-2}R_0, \\ n_0 B^{-1} \left(\frac{R}{R_0}\right)^{-3}, & R > B^{-2}R_0. \end{cases} \tag{3.38}$$

In analogy with cosmology, the condition of photon decoupling (transparency) for an *uniform* medium may be written as

$$n_c \sigma c = H, \tag{3.39}$$

where $\sigma c = \langle \sigma v \rangle$ is the so-called thermally averaged cross section for Compton scattering of photons on electrons [38, p. 61], H is the comoving expansion rate given by

$$H = \frac{dV_c}{V_c dt_c} = a \frac{dR}{R dt_c}, \tag{3.40}$$

where from Eq. (3.36)

$$a = \begin{cases} 3, & R < B^{-1}R_0, \\ 2, & B^{-1}R_0 < R < B^{-2}R_0, \\ 3, & R > B^{-2}R_0. \end{cases} \tag{3.41}$$

Using the transformation between the laboratory and comoving time $dt = \Gamma dt_c$, we obtain from (3.39) the condition of decoupling

$$\frac{n_c \sigma R}{a\Gamma} = 1. \tag{3.42}$$

The optical depth in the uniform expanding medium is then

$$\tau = \frac{n_c \sigma R}{a\Gamma} = \begin{cases} \dfrac{\tau_0}{3}\left(\dfrac{R}{R_0}\right)^{-3}, & R < B^{-1}R_0, \\ \dfrac{\tau_0 B^2}{2}\left(\dfrac{R}{R_0}\right)^{-1}, & B^{-1}R_0 < R < B^{-2}R_0, \\ \dfrac{\tau_0}{3}\left(\dfrac{R}{R_0}\right)^{-2}, & R > B^{-2}R_0. \end{cases} \tag{3.43}$$

The first and the second expressions are in agreement with the results of this Chapter for photon thick outflows up to numerical factors of order unity, see Eqs. (3.19) and (3.23). The third line of Eq. (3.43) corresponds to the case of the outflow with strong hydrodynamical spreading: case a) of Sec. 2.4, see Eq. (3.34).

We conclude that the photon thin asymptotics relevant for the case b) of weak hydrodynamical spreading cannot be obtained in this approach by comparison of rates in the uniform medium without boundaries. In the photon thin case photons decouple from the outflow because they cross its boundaries, and this process by definition is missing in the comoving frame with infinite matter, for which Eq. (3.43) was derived.

3.8 Optical depth of the GRB outflow and transparency radius

Opacity of GRB outflows is dominated by Compton scattering of photons on electrons and positrons, see e.g. [3, 7]. Positrons and electrons are presented in the outflow by pair creation/annihilation process. There are also electrons, associated with baryons, that are predominant source of opacity for GRB with high enough baryon loading, see e.g. [79]. In what follows we treat separately outflows, opacity of which is dominated by pairs and by baryon-associated electrons. Geometry of the outflow and variables used in the computations are illus-

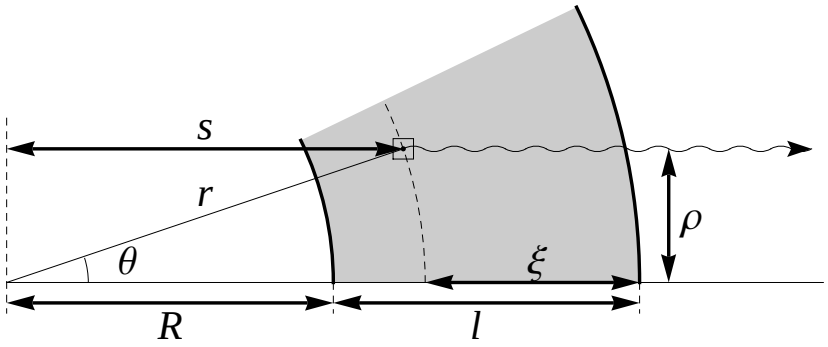

Figure 3.5: Geometry of the outflow (part of it is shown by gray shading) and variables used. Observer is located to the right at infinity.

trated by Fig. 3.5.

The *transparency radius* R_{tr} is defined by equating to unity the optical depth (3.5) for ray direction along the line of sight. This radius has a clear physical meaning: if N photons emitted radially from the inner boundary of the outflow at R_{tr}, then N/e photons are not scattered out of the ray on their way to spatial infinity, where $e = 2.7\ldots$ is the exponential constant. It is clear then that this is the radius of decoupling for the photons emitted from the inner boundary.

It is worth noting that it is the lower limit in the integral (3.5) that is associated with the transparency radius, but not the upper one. The upper limit in (3.5) is the radius at which the photon leaves the outflow, even if it may decouple from the outflow at much smaller radius, as in the photon thick case.

3.8.1 Outflows with opacity dominated by electron-positron pairs

Consider first the case when opacity is dominated by pairs. Then accelerated expansion and optical depth is the same as in the case of pure electron-positron-photon plasma. Due to pair creation/annihilation process number of electrons and positrons in the outflow is not a constant, but it is a function of radial position of the outflow, see Chapter 2.

As pure electron-positron plasma reaches thermal equilibrium before expansion [28, 30] and it remains accelerating until it becomes transparent to radiation[1], the comoving number density of electrons and positrons is then a function of the comoving temperature T_c. It is decreasing during accelerating adiabatic

[1] As rates of Compton scattering $\sigma c n_c$ and annihilation $< \sigma_{e^+e^-} v > n_c$ are comparable (see, e.g. [5]), electron-positron plasma is in thermal equilibrium all the way up to the transparency.

expansion, see Eq. (2.24), as

$$T_c(r) = T_0 \frac{R_0}{r}, \tag{3.44}$$

where T_0 is the temperature of plasma in the source. Far from the source $r \gg R_0$ in ultrarelativistic regime the comoving temperature is nonrelativistic, $kT_c \ll m_e c^2$, as it follows from Eqs. (2.26–2.27), and we can treat electron-positron pairs as nondegenerate and nonrelativistic. Their comoving number density is then

$$n_c(T) = \frac{1}{\sqrt{2}} \left(\frac{kTm_e}{\pi\hbar^2} \right)^{3/2} \exp\left(-\frac{m_e c^2}{kT} \right). \tag{3.45}$$

The optical depth of the pair plasma shell in radial direction is thus

$$\tau(R) = \int_R^\infty \frac{\sigma}{\sqrt{2}} \left(\frac{kT_0 m_e}{\pi\hbar^2} \right)^{3/2} \left(\frac{R_0}{r} \right)^{5/2} \exp\left(-\frac{m_e c^2 r}{kT_0 R_0} \right) dr. \tag{3.46}$$

Solving the equation $\tau(R_{tr}) = 1$ numerically, we obtain that due to exponential dependence on the radial coordinate in pair density (3.45) transparency is reached at the comoving temperature

$$kT_\pm \simeq 0.040 m_e c^2 \tag{3.47}$$

rather independent of the initial conditions of the outflow. Note that the optical depth for an expanding electron-positron-photon shell computed in [80] is incorrect since it uses photon thin asymptotics, which never applies to the pure e^+e^- outflows as they accelerate all the way up to the photosphere. The formula (3.47) is in agreement with works [85] and [92], what used correct photon thick asymptotics.

In thin shell model the radius of transparency corresponding to comoving temperature (3.47) is

$$R_{tr} = \frac{1}{T_\pm} \left(\frac{3E_0 l}{4\pi a} \right)^{1/4}, \tag{3.48}$$

where $a = 4\sigma_{SB}/c$ and σ_{SB} is the Stefan-Boltzmann constant. Analogously in

finite wind model with initial temperature (2.27) we have

$$R_{tr} = \frac{1}{T_\pm}\left(\frac{E_0 R_0^2}{4\pi l a}\right)^{1/4} = \frac{1}{T_\pm}\left(\frac{L R_0^2}{16\pi\sigma_{SB}}\right)^{1/4}, \tag{3.49}$$

where we have used the relations (2.32).

3.8.2 Outflows with opacity dominated by baryon-associated electrons

Consider now the outflows with opacity dominated by electrons associated with baryons. Then we can neglect the pairs and fix the number of electrons in the outflow to the number of baryons

$$N = \frac{E_0 B}{m_p c^2} = \frac{L\Delta t B}{m_p c^2}. \tag{3.50}$$

It this case both for averaged shell model and for finite wind model of the outflow, as it was shown in Sections 3.4 and 3.5, we have three asymptotics of optical depth, one for the outflow at acceleration phase, Eq. (3.23), and two at coasting phase, Eqs. (3.19) and (3.20). These asymptotics can be expressed with the use of parameter τ_0 (3.14)

$$\tau_0 = \sigma n_0 R_0 = \frac{\sigma E_0 B}{4\pi R_0 l m_p c^2} = \frac{\sigma L B}{4\pi R_0 m_p c^3} \tag{3.51}$$

as follows

$$\tau = \begin{cases} \dfrac{1}{6}\tau_0\left(\dfrac{R_0}{R}\right)^3, & R_0 \ll R \ll B^{-1}R_0, \quad (3.52a) \\ \dfrac{B^2}{2}\tau_0\left(\dfrac{R_0}{R}\right), & B^{-1}R_0 \ll R \ll 2B^{-2}l, \quad (3.52b) \\ \tau_0\dfrac{R_0 l}{R^2}, & R \gg 2B^{-2}l. \quad (3.52c) \end{cases}$$

Recall the interpretation of the formulae (3.52). On the one hand, first two asymptotics (3.52a, 3.52b) correspond to the case when the ray propagates in-

side the outflow for a significant time so that the number density on its path substantially decreases before it leaves. In this respect the outflow is "a long wind", even if the laboratory thickness of the outflow may be small, $l \ll R$. That is why we refer to this case as a *photon thick outflow* [89]. On the other hand, (3.52c) corresponds to the case when the number density of the outflow does not change substantially on the photon world line before it escapes. In this respect the outflow is "a thin shell" even if the duration of energy release could be long and a long wind was launched. That is why we refer to this latter case as a *photon thin outflow* [89]. For instance, a geometrically thin ultrarelativistically expanding shell may be both thin or thick with respect to the photon ray propagating inside it.

Similar consideration may be applied to a photon emitted at any distance ξ from the outer boundary of the outflow, see Section 4.2 and Fig. 3.6. It is clear then, that even in a photon thick outflow there is always a photon thin layer located near the outer boundary. During acceleration phase such a photon thin part accounts for a fraction not larger than Γ^{-1} of the entire width of the outflow[2]. Recall that in the derivation of (3.52) we used the finite wind model or averaged shell model, but the asymptotics of optical depth are generic and apply to any density profile of the outflow.

From Eq. (3.52) the transparency radius of the outflow with opacity dominated by baryon-associated electrons has three asymptotics

$$\frac{R_{tr}}{R_0} = \begin{cases} \sqrt[3]{\dfrac{\tau_0}{6}}, & R_{tr} < B^{-1}R_0, \\ \dfrac{\tau_0 B^2}{2}, & B^{-1}R_0 < R_{tr} < B^{-2}R_0, \\ \sqrt{\tau_0 \dfrac{l}{R_0}}, & R_{tr} > B^{-2}R_0. \end{cases} \tag{3.53}$$

Further we will refer this type of the outflows getting transparent at radius R_{tr} with $R_{tr} < B^{-1}R_0$, with $B^{-1}R_0 < R_{tr} < B^{-2}R_0$, and with $R_{tr} > B^{-2}R_0$ to as *accelerating photon thick, coasting photon thick, and coasting photon thin outflows*, respectively.

[2]Formally photon thin accelerating solution exists, and it is given by the Eq. (3.52c). However, its validity condition is $l \ll R_0^2/R = R_0/\Gamma$.

3.9 Transparency of the thin shell

Consider now the shell model of GRBs with typical parameters, expressing their total energy as $E_0 = 10^{54} E_{54}$ erg, initial size as $R_0 = l = 10^8 R_8$ cm and baryonic loading as $B = 10^{-2} B_{-2}$. From Eqs. (3.48) and (3.52) we find the following asymptotic solutions for the transparency radius together with domains of their applicability

$$R_{tr} = \begin{cases} 4.4 \times 10^{10} \left(E_{54} R_8\right)^{1/4} \text{ cm}, \\ \qquad\qquad E_{54} \ll 4.8 \times 10^{-20} B_{-2}^{-4} R_8^{-1}, \\ \hline 1.8 \times 10^{12} \left(E_{54} B_{-2} R_8\right)^{1/3} \text{ cm}, \\ 4.8 \times 10^{-20} B_{-2}^{-4} R_8^{-1} \ll E_{54} \ll 3.2 \times 10^{-8} B_{-2}^{-4} R_8^2, \\ \hline 1.8 \times 10^{17} E_{54} B_{-2}^3 R_8^{-1} \text{ cm}, \\ 3.2 \times 10^{-8} B_{-2}^{-4} R_8^2 \ll E_{54} \ll 1.1 \times 10^{-5} B_{-2}^{-5} R_8^2, \\ \hline 5.9 \times 10^{14} \left(E_{54} B_{-2}\right)^{1/2} \text{ cm}, \\ \qquad\qquad E_{54} \gg 1.1 \times 10^{-5} B_{-2}^{-5} R_8^2. \end{cases} \tag{3.54}$$

Fig. 3.7 shows the energy-baryonic loading diagram, where the regions of validity of the asymptotics are indicated explicitly for typical parameters of GRBs. For very small baryonic loading, or in other words for a pure electron-positron plasma, the transparency radius does not depend on B parameter. For increasing baryonic loading it increases as $B^{1/3}$ (accelerating photon thick solution). In both these cases the Lorentz factor at the transparency is not equal to B^{-1}, but it is much smaller. For larger baryonic loading the transparency radius steeply increases as B^3 (coasting photon thick solution), and finally it increases as $B^{1/2}$ (coasting photon thin solution). For all the relevant range of GRBs parameters 10^{48} erg $< E_0 < 10^{55}$ erg and 10^6 cm $< R_0 < 10^{12}$ cm all four asymptotics are present in the interval $10^{-10} < B < 10^{-1}$. Dependence of parameters of

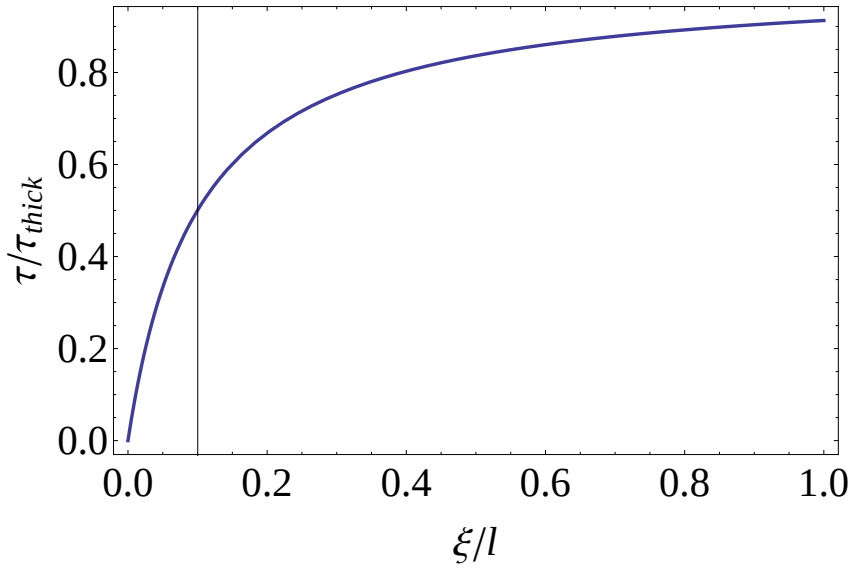

Figure 3.6: Optical depth τ of the outflow with density profile $n \propto r^{-2}$ for radial ray as function of depth of emission ξ at coasting phase. Here τ_{thick} corresponds to optical depth of photon thick asymptotics (3.52b), red line show the position $\xi = (1-\beta)R$ of transition from photon thin $\tau \propto \xi$ to photon thick $\tau \simeq$ const asymptotics of optical depth.

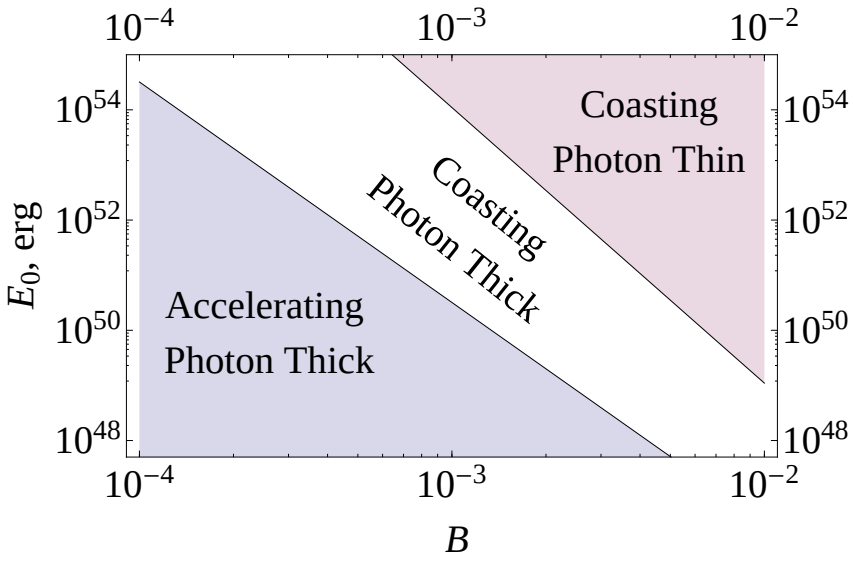

Figure 3.7: The energy–baryonic loading diagram showing the validity of the various asymptotic solutions of the transparency radius for typical parameters of GRBs with $l = R_0 = 10^8$ cm.

transparency on initial conditions is illustrated in Tab. 3.1 at page 80.

Calculating optical depth by integral (3.5) and taking into account both pairs and electrons, associated with baryons, we get for the transparency radius of different shell models the results shown in Fig. 3.8. There we also show as function of the baryonic loading the following quantities computed at the transparency radius: the Lorentz factor, the observed and comoving temperatures, and fraction of energy in the photons there to the total energy, for different values of the total energy E_0. All the four asymptotics of Eq. (3.54) are clearly visible at Fig. 3.8. It is obvious that the highest Lorentz factors at transparency radius are attained in photon thick asymptotics. The largest transparency radii are reached instead in photon thin asymptotics.

3.10 Transparency of the wind

In the case of gradual energy release resulting in relativistic wind an additional parameter is present, that is the duration of energy release, which we parameterize as $\Delta t = 1\Delta t_1$ s. Instead of the total energy E_0 the luminosity $L = 10^{50}L_{50}$ erg/s is used. The corresponding transparency radius is

$$R_{tr} = \begin{cases} 8.1 \times 10^8 L_{50}^{1/4} R_8^{1/2} \text{ cm}, \\ \qquad L_{50} \ll 5.3 \times 10^{-15} B_{-2}^{-4} R_8^{-2}, \\ \hline 1.3 \times 10^{10} \left(L_{50} B_{-2} R_8^2\right)^{1/3} \text{ cm}, \\ 5.3 \times 10^{-15} B_{-2}^{-4} R_8^{-2} \ll L_{50} \ll 9.8 \times 10^{-2} B_{-2}^{-4} R_8, \\ \hline 5.9 \times 10^{10} L_{50} B_{-2}^3 \text{ cm}, \\ \qquad 9.8 \times 10^{-2} B_{-2}^{-4} R_8 \ll L_{50} \ll 10^5 B_{-2}^{-5} \Delta t_1, \\ \hline 5.9 \times 10^{12} \left(L_{50} \Delta t_1 B_{-2}\right)^{1/2} \text{ cm}, \\ \qquad L_{50} \gg 10^5 B_{-2}^{-5} \Delta t_1. \end{cases} \tag{3.55}$$

Fig. 3.9 shows the luminosity-baryonic loading diagram where the regions of validity of the asymptotics discussed above are indicated. Again we can see that

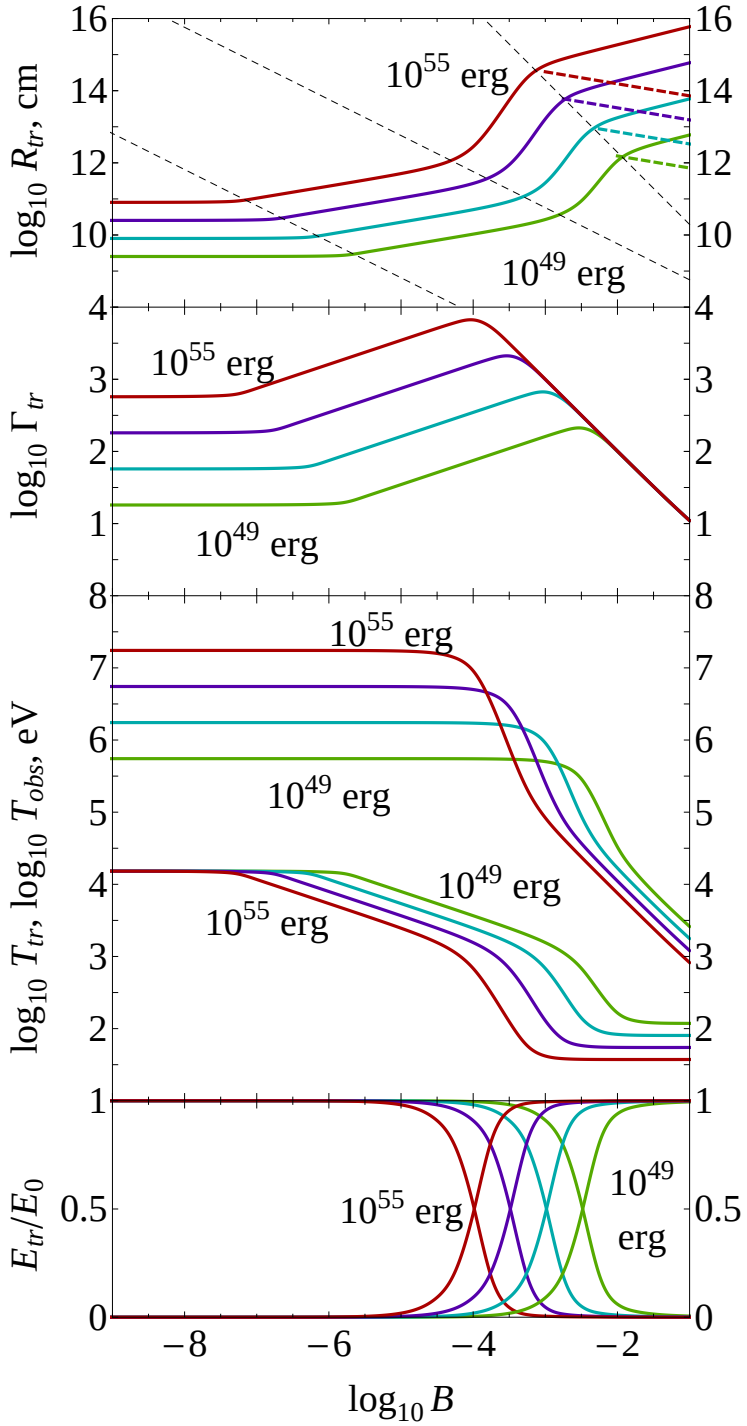

Figure 3.8: From top to bottom: transparency radius R_{tr}, Lorentz factor Γ_{tr}, observed T_{obs} and comoving T_{tr} temperatures, and ratio of the energy in photons to the total energy E_{tr}/E_0 at transparency radius as functions of entropy η for shells with different total energy E_0 but the same width $l = R_0 = 10^8$ cm. All four regimes with different asymptotics are clearly visible and dashed black lines corresponding to their domain of validity from Eq. (3.54) are shown. Curves are drawn for E_0 equal to: 10^{49} erg (green), 10^{51} erg (blue), 10^{53} erg (violet), and 10^{55} erg (red). Dashed thick lines denote the diffusion radius for each energy, see Sec. 4.3.

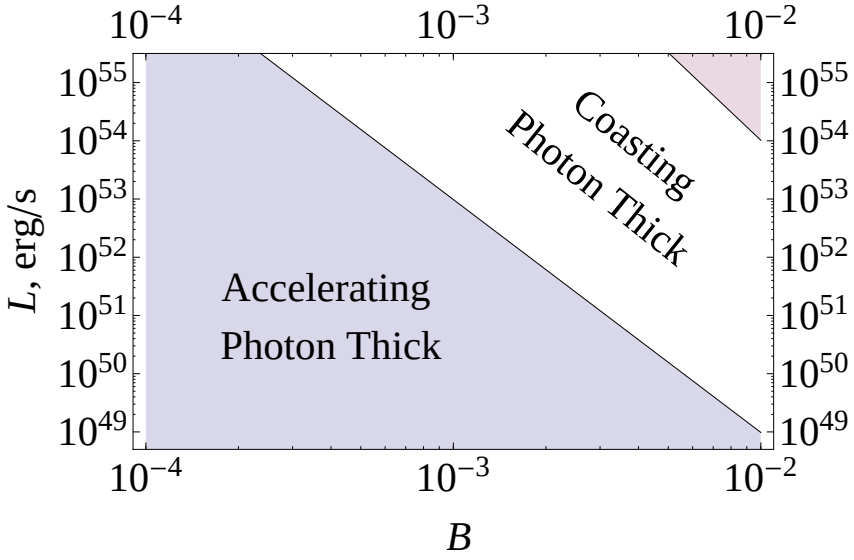

Figure 3.9: The luminosity-baryonic loading diagram showing the validity of the various asymptotic solutions for transparency radius of wind with duration $\Delta t = 0.1$ s. Notation is the same as on Fig. 3.7.

for typical parameters of GRB considered in the literature all the four asymptotic solutions are relevant, contrary to the claims that are encountered in the literature, see for example [93]. The photon thin asymptotic limit may also be valid for relativistic winds in the coasting phase, provided that $l \ll RB^{-2}/2$. This is an independent condition from $\Delta t \gg R_0/c$ and it is therefore possible to give the following constraints for Δt, under which the outflow from a finite wind is photon thin at the transparency radius:

$$\frac{R_0}{c} \ll \Delta t \ll \frac{\tau_0 B^4}{4}\frac{R_0}{c}. \tag{3.56}$$

Dependence of the transparency parameters on the initial conditions of the wind is presented in Tab. 3.2.

Again calculating transparency radius from integral (3.5) taking into account both pairs and electrons we get the results presented in Fig. 3.10. There we show also as function of the baryonic loading the following quantities computed at the transparency radius: the Lorentz factor, the observed and comoving temperatures, and fraction of energy in photons to the total energy, for different duration of the wind with the total energy $E_0 = 10^{51}$ erg, and inner boundary radius $R_0 = 10^8$ cm. Wind duration ranges from 10 ms to 10 s, the corresponding wind luminosity varies from 10^{53} erg/s to 10^{50} erg/s.

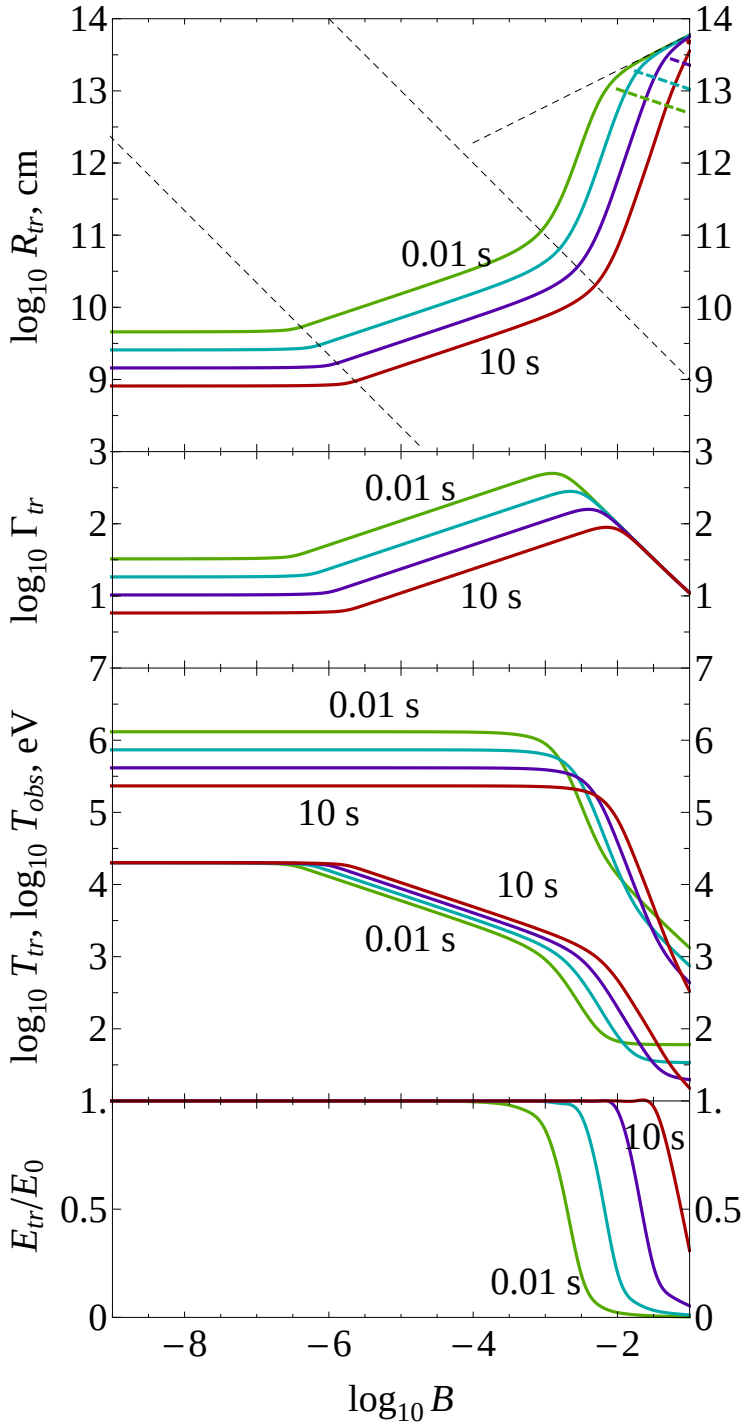

Figure 3.10: The same as in Fig. 3.8 for winds with different duration, but the same total energy $E_0 = 10^{51}$ erg and radius of origin $R_0 = 10^8$ cm. All four regimes with different asymptotics are clearly visible. Curves are drawn for Δt ranging from 10^{-2} s (green) to 10 s (red) in steps of one order of magnitude.

Table 3.1: Dependencies of transparency parameters on initial conditions: energy E_0, baryonic loading B, and radius R_0 for the shell model.

Regime of transparency	R_{tr}			Γ_{tr}			kT_{tr}			kT_{obs}		
Pair	$E_0^{1/4}$		$R_0^{1/4}$	$E_0^{1/4}$		$R_0^{-3/4}$	$0.040 m_e c^2$			$E_0^{1/4}$		$R_0^{-3/4}$
Acceleration	$E_0^{1/3}$	$B^{1/3}$	$R_0^{1/3}$	$E_0^{1/3}$	$B^{1/3}$	$R_0^{-2/3}$	$E_0^{-1/12}$	$B^{-1/3}$	$R_0^{-1/12}$	$E_0^{1/4}$		$R_0^{-3/4}$
Coasting photon thick	E_0	B^3	R_0^{-1}		B^{-1}		$E_0^{-5/12}$	$B^{-5/3}$	$R_0^{7/12}$	$E_0^{-5/12}$	$B^{-8/3}$	$R_0^{7/12}$
Coasting photon thin	$E_0^{1/2}$	$B^{1/2}$			B^{-1}		$E_0^{-1/12}$		$R_0^{-1/12}$	$E_0^{-1/12}$	B^{-1}	$R_0^{-1/12}$

Table 3.2: Dependencies of transparency parameters on initial conditions: energy release rate L, baryonic loading B, duration Δt, and initial radius R_0 for the wind model.

Regime of transparency	R_{tr}			Γ_{tr}			kT_{tr}			kT_{obs}			
Pair	$L^{1/4}$		$R_0^{1/2}$	$L^{1/4}$		$R_0^{-1/2}$	$0.040 m_e c^2$			$L^{1/4}$			$R_0^{-1/2}$
Acceleration	$L^{1/3}$	$B^{1/3}$	$R_0^{2/3}$	$L^{1/3}$	$B^{1/3}$	$R_0^{-1/3}$	$L^{-1/12}$	$B^{-1/3}$	$R_0^{-1/6}$	$L^{1/4}$			$R_0^{-1/2}$
Coasting photon thick	L	B^3			B^{-1}		$L^{-5/12}$	$B^{-5/3}$	$R_0^{1/6}$	$L^{-5/12}$	$B^{-8/3}$		$R_0^{1/6}$
Coasting photon thin	$L^{1/2}$	$B^{1/2}$	$\Delta t^{1/2}$		B^{-1}		$L^{-1/12}$	$\Delta t^{-1/3}$	$R_0^{1/6}$	$L^{-1/12}$	B^{-1}	$\Delta t^{-1/3}$	$R_0^{1/6}$

3.11 Comparison with previous works

Reviewing existing literature, we found that different asymptotics for optical depth and transparency radius were used previously, see Tab. 3.3. There were no paper discussing all asymptotics with the range of their applicability until a recent work of Toma, Wu & Mészáros (2011) [93].

As the photon thick outflow becomes transparent for the photons from different differential shells at the same radius equal to the radius of transparency, this radius is traditionally called in the literature the radius of photosphere, e.g. [23]. The expressions for the optical depth of a relativistic wind outflow were obtained e.g. in [20]. Their formulas coincide with our (3.52) up to a numerical factor which comes from the integration over the radial coordinate. It should be noted, however, that only the photon thick asymptotic limit is discussed in [20]. The transparency radius for photon thick and photon thin asymptotics for a finite coasting relativistic wind outflow was obtained by [96]. However, literature on the photospheric emission of relativistic winds generally neglect photon thin asymptotics, see e.g. [23, 26].

Similar considerations apply to an ultrarelativistic shell which is considered in [32, 79, 80] in the photon thin approximation. The corresponding condition that the shell at the photospheric radius appears to be photon thin is $\tau_0 \gg 4B^{-4}$. Gamma-Ray Bursts analyzed so far in the context of the fireshell model fall into the domain of validity of photon thin asymptotics with the only exception of two cases, GRB050509B and GRB071227, see Fig. 3.11. For low baryonic loading it is possible that initial conditions result in a photon thick shell, considered for the case of giant flares in soft gamma-ray repeaters in [98].

All asymptotic solutions for the optical depth have been considered by [12], except for the case of pure electron-positron outflow. They derived the photospheric radius considering the expansion in comoving reference frame, see Sec. 3.7. Notice, that the photon thin asymptotics was obtained in [12] by assuming hydrodynamic spreading of the outflow found by the same authors in [32]. In absence of such spreading (e.g. for the finite wind model considered above) this asymptotics cannot be obtained this way. Finally, [93] discusses all asymptotic solutions, applying them to a relativistic wind.

Table 3.3: Different asymptotics of transparency radius

Paper	Pairs	Accelerating	Coasting thick	Coasting thin
Goodman (1986) [10]	+	−	−	−
Paczynski (1986) [11]	+	−	−	−
Shemi & Piran (1990) [80]	±	−	−	−
Paczynski (1990) [27]	+	−	+	−
Abramowicz, Novikov & Paczynski (1991) [94]	−	−	+	−
Thompson (1994) [95]	−	+	+	−
Grimsrud & Wasserman (1998) [85]	+	+	+	−
Rees & Mészáros (2000) [20]	±	+	+	−
Ruffini, Salmonson, Wilson, & Xue (2000) [78]	±	−	−	+
Daigne & Mochkovitch (2002) [96]	−	+	+	−
Iwamoto & Takahara (2002) [97]	+	+	+	−
Mészáros, Ramirez-Ruiz, Rees & Zhang (2002) [12]	+	±	±	±
Rees & Mészáros (2005) [21]	+	+	+	−
Nakar, Piran & Sari (2005) [98]	±	+	+	−
Li & Sari (2008) [92]	+	+	+	−
Toma, Wu & Mészáros (2011) [93]	±	+	+	+

Sign + means that this asymptotics was considered in the paper, − means that asymptotics was not considered, and ± means that although the asymptotics was considered, its range of validity was found incorrectly.

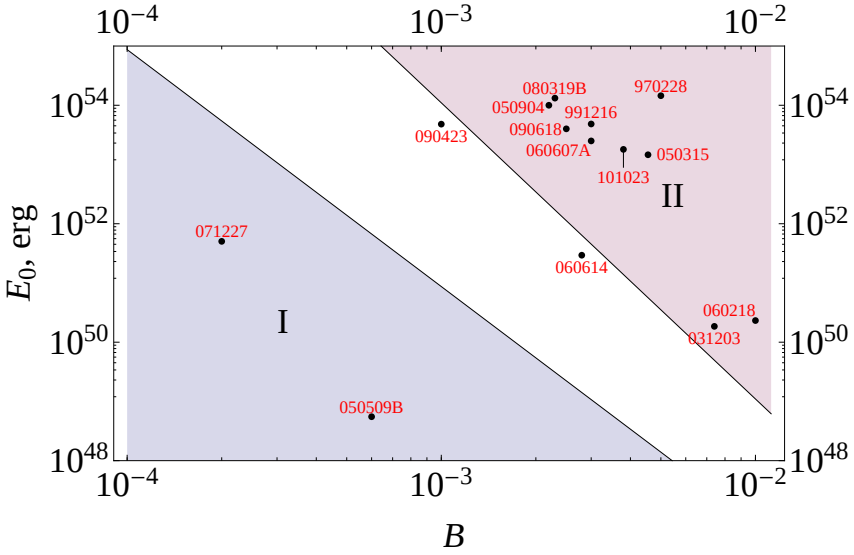

Figure 3.11: Validity of different asymptotics shown on the plane E–B with $l = 10^8$ cm. Blue range I represents applicability domain of accelerating photon thick asymptotics. In white region the coasting photon thick asymptotics is valid, while in the magenta region II the coasting photon thin asymptotics is held. GRBs analyzed so far in the fireshell model are shown by red points with the numbers. Data for different GRBs were taken from the following papers: GRB970228 [99], GRB991216 [100], GRB050315 [101], GRB060607A [102], GRB090618 [103], GRB060218 [104], GRB031203 [105], GRB060614 [106], GRB090423 [107, 108], GRB050509B [109], GRB071227 [110, 111], GRB080319B and GRB050904 [112], GRB101023 [113].

3.12 Conclusions

We conclude that interpretation of the formula (3.52) it terms of photon thick and photon thin conditions given in this Chapter provides additional physical insight to the consideration of optical depth in shell and wind models of GRBs. This new classification is different from the classification based on the geometrical thickness of the outflow, that is essential in the hydrodynamic treatment of Chapter 2.

The photon thick/thin classification is rooted in the time evolution of ultrarelativistic outflow as it expands during the light crossing time of the outflow. Due to relativistic motion this time is $2\Gamma^2$ times larger than crossing time for static shell of the same width, that is just a kinematic effect. If the evolution of the outflow during this time is negligible, we refer to the outflow as photon thin; if it

is substantial, we refer to the outflow as photon thick. It should be stressed that as a result of relativistic motion outflows are effectively "thickened", as crossing time is increasing.

One of the scopes of this Chapter is to show that the association of “instantaneous energy release” with “thin shell” (e.g. [32, 33]) and “continuous energy release” with “thick wind” (e.g. [11, 27]) generally adopted in the literature is incomplete with respect to the optical depth of the outflows: both shells can be "wind-like", i.e. photon thick, see Fig. 3.7, and winds can be "shell-like", i.e. photon thin, see Fig. 3.9. We found that all four asymptotics of optical depth and transparency radius derived in Sec. 3.8 are relevant for typical parameters of GRBs both in shell and wind models, see Sections 3.9 and 3.10.

Chapter 4

Radiative transport in ultrarelativistic outflows and photospheric emission of GRBs

Due to rarefication of the expanding GRB outflow photons decouple from it and reach the observer. These photons represent the photospheric emission of GRBs. Early models of such photospheric emission have been proposed already in the 80's [10, 11]. Within the fireshell model [75] special attention is paid to this emission which is called the Proper GRB (P-GRB) [100, 114]. In this model both energy and time separation of this emission from the rest of the prompt emission is predicted and identified in many GRBs, see [99–113].

Theoretically properties of this emission were studied in [114–117]. In [115] radiative diffusion from expanding outflow was treated as a quasistationary problem in semiinfinite medium and the results were then applied in [114] to obtain light curves and spectra of P-GRB. However, GRB outflows are both non-stationary and finite, and in this Chapter we take into account these factors. Another approach of slicing the GRB outflow into small shells emitted during the process of collapse, suggested in [77], was used in [116, 117] with a simplifying assumption about instantaneous emission of thermal spectrum of photons from these shells of plasma at their transparency. Here we treat the problem with the help of full radiative transfer and take into account the fact that process of photon decoupling from different parts of the outflow is not instantaneous.

Following the identification of thermal component in time-resolved spectra of BAT GRBs [118, 119], a different theoretical approach to photospheric emission was developed, e.g. in [23, 24, 24–26, 76]. It uses essentially the model of

steady wind due to Pachinski [11, 27] and analytic result for the optical depth in this case was obtained in [94]. In particular, geometrical effects of switching off relativistic wind were discussed in the work [23]. Comoving anisotropy of radiative field was discussed in the work [25] using radiative transfer and MC simulations. However, they all miss the case of photon thin outflows.

In this Chapter we present the treatment of radiative transport in the relativistic outflows with application to GRBs, based on the paper [89]. In Section 4.3 radiative diffusion in an expanding relativistic outflow is treated. In Section 4.2 we discuss geometry and dynamics of the outflow photosphere as seen by a distant observer. Section 4.1 describes the scheme of application of radiative transfer equations to photospheric emission of relativistic outflows. Then observed light curves and spectra of photon thick and photon thin outflows are computed in Sections 4.4–4.5. In Section 4.6 main results and their implications for GRBs are discussed. Conclusions follow.

4.1 Radiative transfer in relativistic outflows

The basis of spectrum and flux calculation is the radiative transfer equation for specific intensity I_ν along the ray, see e.g. [61, p. 11]

$$\frac{dI_\nu}{ds} = j_\nu - \kappa_\nu I_\nu, \tag{4.1}$$

where j_ν is monochromatic emission coefficient, κ_ν is absorption coefficient and s is distance, measured along the ray.

Spectral intensity of radiation at infinity on a ray coming to observer at some arrival time t_a is given by formal solution of this equation

$$\begin{aligned} I_\nu(\nu,\rho,t_a) &= \int \mathcal{I}_\nu(\nu,r,\theta,t)\frac{d}{ds}\left\{\exp[-\tau(\nu,r,\theta,t)]\right\}\, ds \\ &= \int \mathcal{I}_\nu(\nu,r,\theta,t)\exp[-\tau(\nu,r,\theta,t)]\, d\tau, \end{aligned} \tag{4.2}$$

where $\mathcal{I}_\nu(r,\theta,t)$ is the source function, equal to the ratio of emission and absorption coefficients $\mathcal{I}_\nu = j_\nu/\kappa_\nu$, optical depth τ is an integral of κ_ν from the point on the ray under consideration to infinity $\tau = \int \kappa_\nu ds$, given by Eq. (3.2) or, after specification of reference frame, by Eq. (3.5), and variables (r,θ,t) are connected by $t_a = t - r\cos\theta$ and $r\sin\theta = \rho$, see Fig. 3.5. We use Thomson scattering cross

section in comoving frame $\kappa_{\nu,c} = const$.

The formal solution (4.2) emphasizes the meaning of optical depth τ (3.2) that defines the visibility of N_0 photons, emitted towards the observer from a given element of 4-tube around the ray world line, specified by the parameter s along the ray. The intensity in these photons is given by the source function $\mathcal{I}_\nu$, and only $N_0 \exp(-\tau)$ part of them reaches the observer without further scattering or absorption.

Total observed flux is an integral over all rays

$$F_\nu(\nu, t_a) = 2\pi\Delta\Omega \int \rho \, d\rho \, I_\nu(\nu, \rho, t_a), \tag{4.3}$$

where $\Delta\Omega$ is the solid angle of the observer's detector as seen from the outflow in the laboratory frame and $2\pi\rho d\rho$ is an element of area in the plane of the sky.

In what follows we assume that emissivity j_ν is thermal and isotropic in comoving frame of the outflow. The laboratory source function is then

$$\mathcal{I}_\nu(\nu, r, \theta, t) = \frac{2h}{c^2} \frac{\nu^3}{\exp\left\{\frac{h\nu\Gamma(r,t)[1-\beta(r,t)\cos\theta]}{kT_c(r,t)}\right\} - 1}, \tag{4.4}$$

where T_c is the comoving temperature. This approximation is justified when the radiation field is tightly coupled to the matter. The photospheric emission comes from entire volume of the outflow, and the computational method sketched above is closely related to that used in [25] where the concept of "fuzzy photosphere" was introduced. This method will be referred to as *fuzzy photosphere* approximation.

Most of energy reaching observer is emitted from the region near the the photosphere. One can define the probability density function along the ray as

$$P(r, \theta, t) = P_0 \frac{d}{ds} \exp[-\tau(r, \theta, t)] \tag{4.5}$$

with P_0 being normalization. When the time dependence in this equation is discarded this $P(r, \theta)$ coincides with the probability density function of the last scattering defined in [23]. This function determines the probability of the photon to come to observer at infinity, and it reaches the maximum near the photosphere. For determination of both light curves and spectra of photospheric emission it is then crucial to know the dynamics of the photosphere which crosses the outflow

during its expansion. Assuming that all the energy comes from the photosphere only, i.e. from a surface instead of the volume discussed above, the computation of fluxes and spectra may be reduced to one dimensional integration by substitution of the function P with a Dirac delta in the integral (4.2). Such more crude approximation, in contrast to the fuzzy photosphere one, will be referred to as *sharp photosphere* approximation.

4.2 Geometry and dynamics of the photosphere

Unlike traditional static sources usually dealt with in astrophysics, relativistic outflows may have strongly time-varying photospheres, i.e. surfaces of $\tau = 1$ along the ray coming to the observer at infinity. For the finite wind model (3.11) the optical depth can be calculated analytically both at acceleration and coasting phases for photon thin and photon thick outflows. For model of Lorentz factor, smoothly joining asymptotics (2.21) and (2.22)

$$\Gamma(r) = \frac{r}{R_0 + r/\eta} \tag{4.6}$$

the result is

$$\begin{aligned}\tau(r,\theta,t) = \tau_0 R_0 \Bigg\{ & \frac{1}{r\sin\theta}\left[\theta - \tan^{-1}\left(\frac{r\sin\theta}{cT + r\cos\theta}\right)\right] \\ & - \beta_m \left(\frac{1}{r} - \frac{1}{\sqrt{(cT + r\cos\theta)^2 + (r\sin\theta)^2}}\right) \\ & + \frac{R_0^2}{6}\left(\frac{1}{r^3} - \frac{1}{\left[(cT + r\cos\theta)^2 + (r\sin\theta)^2\right]^{3/2}}\right)\Bigg\},\end{aligned} \tag{4.7}$$

where T is the time interval during which photon remains inside the outflow, determined by the equations of motion of the photon and of the outflow, and $\beta_m = 1 - B^2/2$. For a given laboratory time t the photosphere geometry $r = r(\theta)$ is obtained by equating (4.7) to unity along the rays coming to observer. Then formula (4.7) gives complete information on the dynamics and geometry of the photosphere of finite ultrarelativistic wind. In order to understand this dynamics it is instructive to consider its limiting cases.

Firstly, the photosphere of the coasting infinitely long relativistic wind with

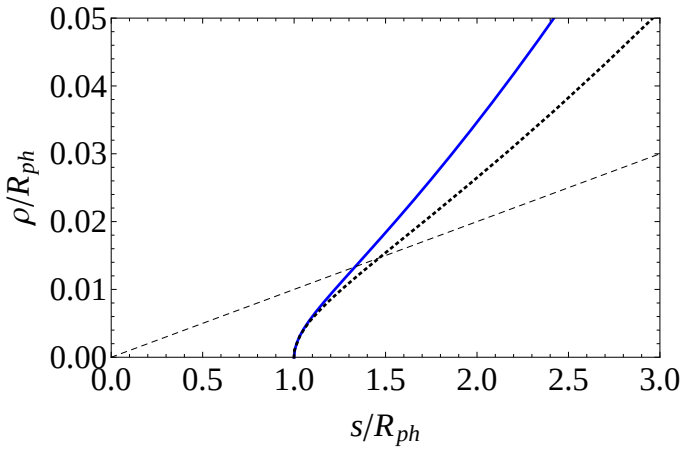

Figure 4.1: The shape of photospheres of infinitely long coasting (blue solid curve) and accelerating (black dotted curve) winds for $\Gamma_{ph} = 100$. Dashed line shows the relativistic beaming angle.

$\Gamma = \text{const}$ analyzed by [94] may be recovered from (4.7) with $T \to \infty$. In that case the last term in (4.7) can be neglected and we have (see e.g. [23])

$$\frac{r}{R_0} = \tau_0 \left(\frac{\theta}{\sin\theta} - \beta_m \right), \tag{4.8}$$

which is a static surface having concave shape, see Fig. 4.1.

Secondly, the photosphere of the accelerating infinite wind may be obtained from (4.7) for $T \to \infty$ and $\eta \to \infty$. It results in a cubic equation describing a static surface

$$\frac{r}{R_0} = \frac{\zeta\tau_0}{3}\left(1 - A - A^{-1}\right), \tag{4.9}$$

$$A = \sqrt[3]{\frac{4\zeta^3\tau_0^2}{3\sqrt{9 + 8\zeta^3\tau_0^2} - 9 - 4\zeta^3\tau_0^2}}, \qquad \zeta = \frac{\theta}{\sin\theta} - 1,$$

with curvature larger than that of the coasting wind, see Fig. 4.1. In both cases these photospheres appear for a distant observer as static spots with radius

$$\rho = \pi\tau_0 R_0. \tag{4.10}$$

Now consider dynamic properties of the photosphere of ultrarelativistic outflow described by (4.7) as seen by a distant observer. The arrival time of radiation

is defined as $t_a = t - r\cos\theta/c$. The equitemporal surface (EQTS) of the photosphere represents a part of the photosphere visible at a given instant of arrival time t_a, see e.g. [100]. We will refer to that surface as *Photospheric EQTS* (PhE).

PhE of any outflow initially appears at acceleration phase as a convex surface with increasing visible radius, tending to asymptotic value of $\rho = R_0$, that propagates towards observer with increasing velocity, see Fig. 4.2.

If at transparency outflow is still deep in acceleration phase, size of spot changes at this phase of the PhE evolution as

$$\rho = \sqrt{R_0^2 - (t_a/c)^2}, \qquad -R_0/c \le t_a \le 0,$$

and velocity of central part of PhE reaches the maximum and begin to decrease. That leads to change of PhE shape—it become concave. Then at $t_a = 0$ PhE reaches the photosphere of infinite accelerating wind (4.9) inside relativistic beaming surface $\cos\theta = \beta$ (in this case it is the cylinder $\rho = R_0$) and stop there, growing only along this surface almost linearly with arrival time $\rho \simeq R_0 + ct_a$.

If baryon loading is higher, outflow comes into coasting phase still being optically thick as a whole. PhE does not become concave at acceleration, instead it transforms to the part of convex ellipsoid, that is the EQTS of infinitesimally thin constantly emitting relativistic shell considered firstly in [120] and then in [121, 122], see the first PhEs at Fig. 4.3. The EQTS of this shell appears to a distant observer as an ellipsoid with axes ratio equal to Γ. The external boundary of PhE—part of the ellipsoid described—for a given t_a is defined by the condition that photons emitted from the outermost layer of the outflow toward observer has $\tau = 1$. In the beginning of coasting phase, when PhE crosses photon thin part of the outflow, this surface almost coincides with the relativistic beaming cone, provided by $\xi|_{\tau=1} \ll B^2 R$. Visible radius of PhE is growing at this stage as $\rho = ct_a/B$.

If baryon loading is not so high, then PhE crosses photon thin part of the outflow and comes into photon thick part. This leads to decrease of PhE velocity propagation, firstly in the central part, and then at larger and larger θ. Form of PhE become concave and it tends asymptotically to the photosphere of infinite coasting wind (4.8). Notice that the boundary of PhE at this phase gets out of the relativistic beaming angle, see Fig. 4.3.

In the last case of very high baryon loading PhE resides only in photon thin part of the outflow and PhE is always the part of ellipsoid described above.

Let us summarize similarities and differences between PhEs of accelerating and coasting outflows. Developed PhE of photon thick outflow has concave shape, see Fig. 4.2 and Fig. 4.3. This concave PhE in both cases approaches the photosphere of infinitely long wind. In the coasting case the approach to that surface is only asymptotic, while in the accelerating case the photosphere actually reaches it at finite arrival time. The external boundary of the PhE for a given t_a shown in Fig. 4.3 is defined by the condition that the optical depth for photons emitted from the outermost layer of the outflow equals unity. Notice that this boundary is wider than the relativistic beaming surface (these are tube and cone for accelerating and coasting outflows, respectively).

As soon as the innermost part of the outflow reaches the photospheric radius, i.e. observer sees the switching off of the wind, the inner boundary of the PhE expands with t_a. The surface of these boundaries is given by Eqs. (4.8) and (4.9) in the case of coasting and accelerating photon thick outflows, respectively. Analogous behavior is presented in the case of photon thin outflow, but it is irrelevant for photospheric emission and will not be described here in detail.

4.3 The role of radiative diffusion

Before considering the photospheric emission from photon thick and photon thin outflows we focus on the role of radiative diffusion.

In the previous Chapter we assumed explicitly that photons escape the expanding outflow when its optical depth decreases to unity. We have distinguished two possibilities:

- in the photon thick case electron number density decreases along the photon path so rapidly that the medium becomes too rarified to sustain collisions. Most photons however still remain inside the outflow after decoupling;
- in the photon thin case the variation of the electron number density along the ray can be neglected, but the mean free path of photons increases with expansion and eventually exceeds the radial thickness of the outflow.

However, photon can also escape from the outflow due to diffusion, and we briefly discuss this effect below.

Comoving diffusion time is given by $t_{D,c} = l_c^2/D_c$, where $l_c = \Gamma l$ is the comoving radial thickness of the outflow, and diffusion coefficient is $D_c =$

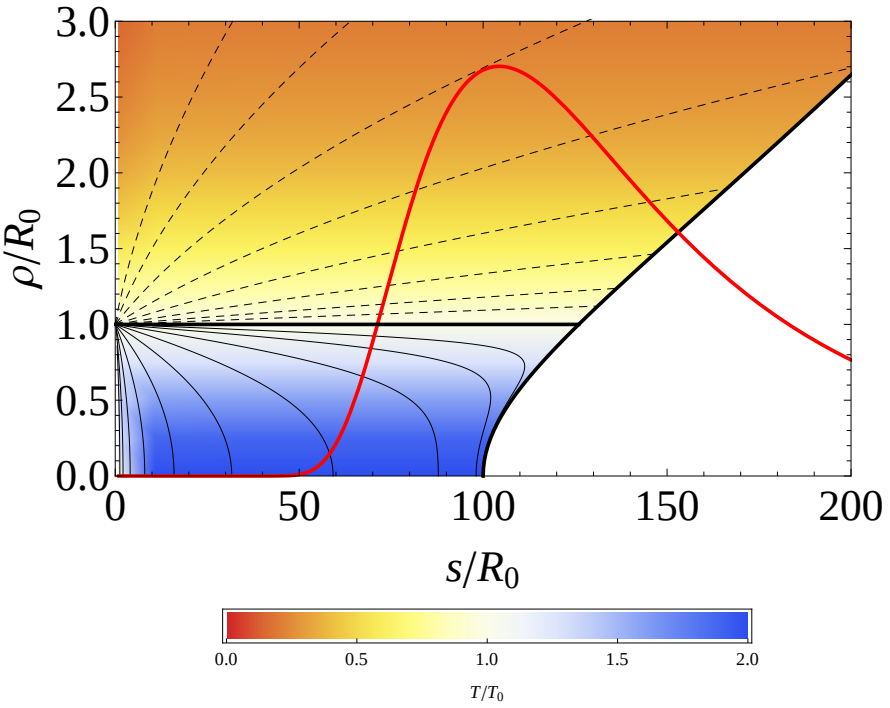

Figure 4.2: PhE of the photon thick accelerating outflow at different arrival times, and the probability density function of photon last scattering integrated over angles $P(r)$ (red thick curve). Thick black curve represents the photosphere of infinitely long accelerating wind. PhEs are illustrated for several arrival times with logarithmic spacing (from right to left $t_a = (-2^{-10}\delta t, -2^{-9}\delta t, \dots)$, see (4.12)) by thin black curves. The surface $\cos\theta = \beta$ is given by $\rho = R_0$ and it is shown by thick black line. Dashed curves illustrate the maximal visible size ρ for several arrival times with logarithmic spacing $t_a = (2^{-10}\delta t, 2^{-9}\delta t, \dots)$ from bottom to top. The PhE at that arrival times is a part of the wind photosphere limited by the corresponding curves. Range of observed temperature of emission under the asymptotic photosphere is illustrated by color, see legend. Here $R_{ph} = 100R_0$.

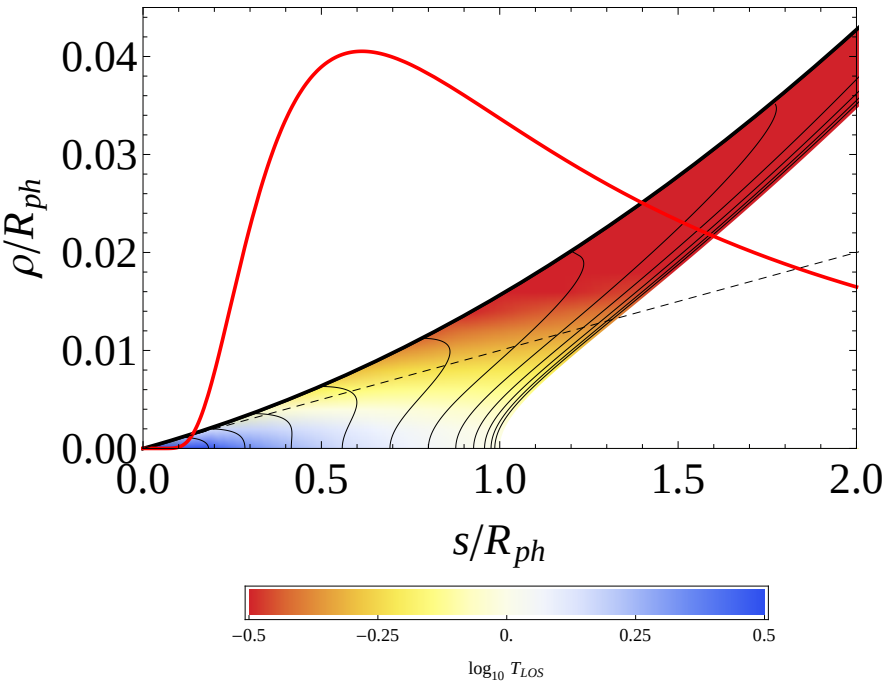

Figure 4.3: The same as in Fig. 4.2 for a photon thick coasting outflow. PhEs are illustrated by thin curves for several arrival times with logarithmic spacing from left to right $t_a = (10^{-2}t_p, 10^{-1.75}t_p, 10^{-1.5}t_p, \dots)$, see (4.14). Thick black curve bounding PhEs correspond to the position of maximal visible angles at given t_a. Notice that these angles exceed the relativistic beaming angle, shown by dashed black line. Right edge of the colored area is the photosphere of infinitely long coasting wind (4.8). Here $\Gamma = 100$.

$(c\lambda_c)/3 = c/(3\sigma n_c)$, where λ_c and n_c are comoving mean free path of photons and comoving electron number density, respectively.

In order to determine, at which radii diffusion becomes important, one has to compare this comoving diffusion time with comoving expansion time of the outflow $t_c = R/(c\Gamma)$. Then we obtain that it happens when the outflow reaches the radius

$$R_D = \left(\tau_0 \eta^2 R_0 l^2\right)^{1/3} \simeq \begin{cases} 7.2 \times 10^{13} (E_{54} l_8 B_{-2}^{-1})^{1/3} \text{ cm}, \\ 2.2 \times 10^{13} (L_{50} \Delta t_1^2 B_{-2}^{-1})^{1/3} \text{ cm}. \end{cases} \tag{4.11}$$

This diffusion radius turns out to be larger than the transparency radius of photon thick outflows, $R_D \gg R_{tr}$, so that diffusion is irrelevant for their description.

In the case of photon thin outflows the diffusion radius is smaller than the transparency radius $R_D \ll R_{tr}$. In this case most radiation leaves the photon thin outflow not at its photospheric radius, but when it reaches the diffusion radius. Notice, that at that radius the outflow as a whole is still opaque.

In other words, the decoupling of photons from the outflow occurs not locally, as in the photon thick case, but near its boundaries where photons are transferred to by diffusion. In this sense the characteristic radius of the photospheric emission is not the transparency radius found from (3.52), but the radius of diffusion (4.11). Besides, the comoving temperature of escaping radiation is different from that discussed in Section 3.8. We discuss all these effect in details in Sec. 4.5.

4.4 Photospheric emission from photon thick outflows

For photon thick outflow the optical depth (4.7) becomes function of r and θ only and the comoving temperature also depends only on radius. In this respect the photon thick case is similar to the infinite wind. Then the integrand in (4.3) does not depend on time and only limits of integration provide time dependence due to motion of the outflow boundaries. The probability density function (4.5) integrated over angles is shown in Figs. 4.2 and 4.3 for accelerating and coasting photon thick outflows.

The observed flux of photospheric emission from accelerating outflow is illustrated in Fig. 4.4 by thick red curve (fuzzy photosphere) and by dotted blue curve (sharp photosphere). The characteristic raising and decaying time is in

both cases

$$\delta t = \frac{R_0^2}{(R_{tr}c)} = \frac{R_0}{\Gamma_{tr}c}. \tag{4.12}$$

There is no simple analytic expression describing full light curve, however its decreasing part is close to a power law with index -4.7 and -6.5 within fuzzy and sharp photosphere approximations, respectively. As minimal duration of the photon thick outflow Δt is of order R_0/c, then $\Delta t \gg \delta t$ and the light curve has almost rectangular shape.

Such accelerating outflow appears to a distant observer as a spot with size $\rho = (R_0^2 - (t_a/c)^2)^{1/2}$, for $-R_0/c \leq t_a \leq 0$. As soon as the PhE reaches the corresponding accelerating infinitely long wind photosphere at $t_a = 0$ the spot size starts to increase almost linearly with time $\rho \simeq R_0 + ct_a$. Finally, as the innermost part of the outflow reaches the transparency radius the spot transforms to a ring with rapidly decreasing width and brightness.

The observed photospheric emission of the coasting photon thick outflow results in the flux changing as

$$F = F_{max}\left[1 - (t_p/t_a)^2\right], \tag{4.13}$$

with

$$t_p = \frac{R_{tr}B^2}{2c}, \tag{4.14}$$

i.e. increase up to the saturation value $F_{max} \propto L$, see the raising part of the light curve in Fig. 4.5, both in sharp and fuzzy photosphere approximations. Radius of the visible spot then reaches its maximal size (4.10). As arrival time exceeds $t_p + \Delta t$ the innermost part of the outflow approaches the wind photosphere (4.8) along the line of sight and the spot transforms to a ring, the flux decreases rapidly in both approximations

$$F \propto t_p^2\left[\frac{1}{(t_a - \Delta t)^2} - \frac{1}{t_a^2}\right]. \tag{4.15}$$

For $t_a \gg \Delta t$ it behaves as $F \propto t_a^{-3}$, see the decreasing part of the light curve in Fig. 4.5. Similarly to the accelerating photon thick outflow the light curve for

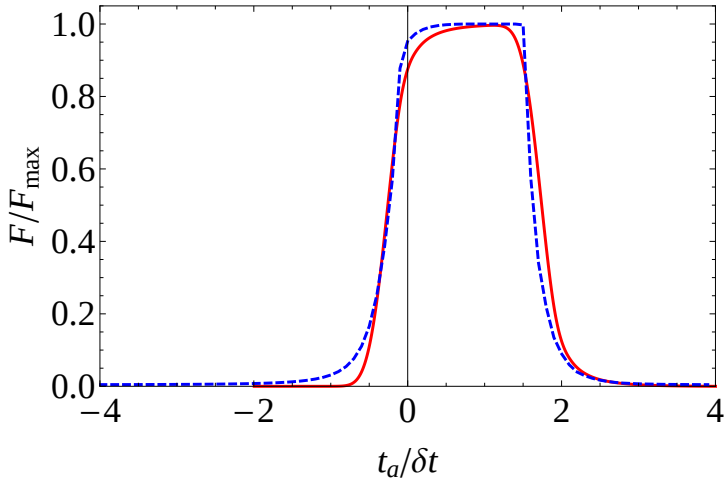

Figure 4.4: The light curve of photospheric emission from the photon thick accelerating outflow in fuzzy (red curve) and sharp photosphere approximations (dashed blue curve). Here $R_{ph} = 100R_0$, and $\Delta t = 2\delta t$, see (4.12).

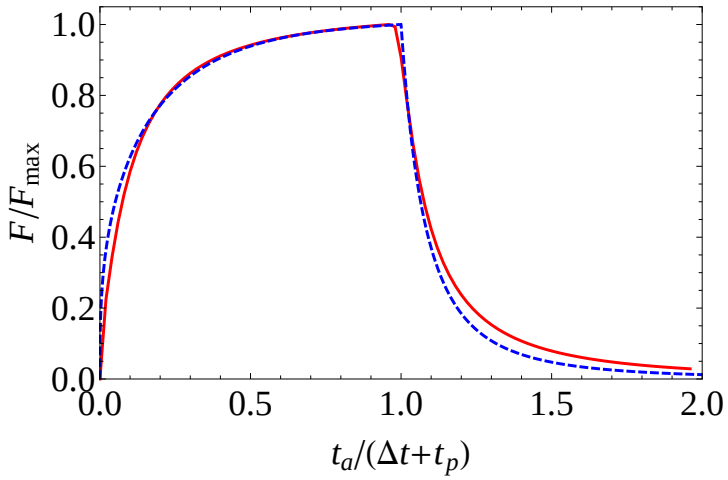

Figure 4.5: The same as in Fig. 4.4 for a photon thick coasting outflow. Here $\Gamma = 100$ and $\Delta t = 5t_p$, see (4.14).

$\Delta t \gg t_p$ has almost rectangular shape due to the fact that its increase and decay times are much shorter than Δt.

Accelerating photon thick outflows exhibit photospheric spectra close to thermal ones, see Fig. 4.6. In ultrarelativistic case spectra computed using both sharp and fuzzy photosphere approximations are very close to each other. Both have small deviations from thermal spectrum in the low energy part with the corresponding Band low energy indices $\alpha = 0.82$ and $\alpha = 0.71$, respectively.

In contrast, the spectrum of photospheric emission of the coasting photon

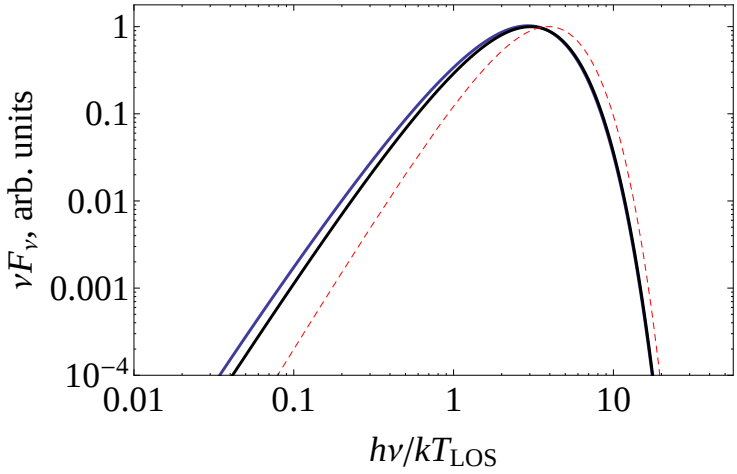

Figure 4.6: Instantaneous spectrum of photospheric emission of accelerating photon thick outflow in continuous (blue thick curve) and sharp photosphere approximation (black thick curve). Dashed red curve represents the thermal spectrum with the temperature at the line of sight T_{LOS}. Lorentz factor at photospheric radius is $\Gamma_{ph} = 100$.

thick outflow is significantly wider that the thermal spectrum, see Fig. 4.7. Low energy part is described by a power law with Band indices respectively $\alpha = 0.34$ and $\alpha = 0$, for sharp and fuzzy photosphere approximations.

After initial phase of evolution, namely rising of the low-energy part, spectra do not evolve until observer detects emission from the innermost part of the outflow. At that moment there is a transition to another phase characterized by the fast decrease of both temperature and flux. Considering time-integrated spectrum we find that as characteristic times of the first and third phases are much less than that of the second one, the spectrum is close to the instantaneous one described above.

4.5 Photospheric emission from photon thin outflows

Now we turn to photon thin outflows. In Sec. 4.3 we pointed out that most of the radiation leaves the outflow not at its transparency radius, but earlier, before and near the diffusion radius. Given that opacity of the outflow is still large there, the emission escapes only from a very narrow region near the outer boundary of the outflow. The probability density function (4.5) is strongly peaked in this narrow region and the photospheric emission for a given arrival time originates

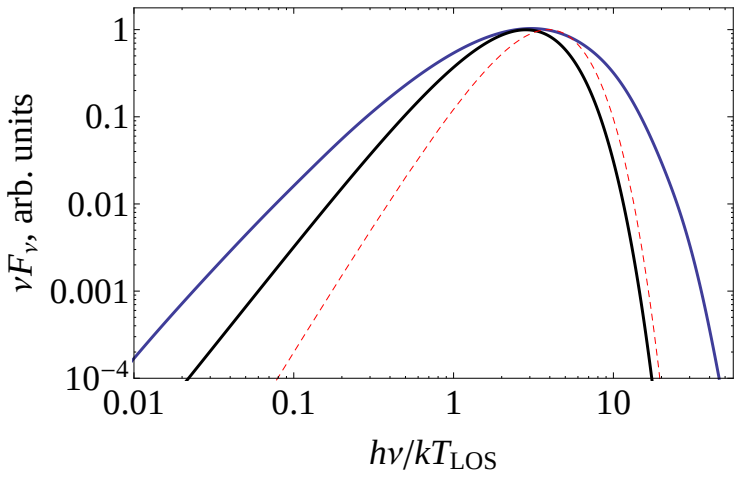

Figure 4.7: The same as in Fig. 4.4 for a photon thick coasting outflow with Lorentz factor $\Gamma = 100$.

from this place. Sharp photosphere approximation is thus completely justified for photon thin outflows.

Since all the radiation is emitted from the PhE we briefly remind its geometry and dynamics. The PhE of the photon thin outflow is similar to EQTS of infinitesimally thin constantly emitting relativistic shell considered firstly by [120] and then by [121, 122]. The EQTS of this shell appears to a distant observer as an ellipsoid with axes ratio equal to Γ. However the PhE of photon thin outflow is not the entire ellipsoid: it is only a part of that surface, see Fig. 4.8. The external boundary of the PhE for a given t_a is defined by the condition that photons emitted from the outermost layer of the outflow toward observer leaves the outflow. In the photon thin asymptotics this surface coincides with the relativistic beaming cone.

We again start with the radiative transfer equation (4.1). In contrast with the photon thick case, here the source function $\mathcal{I}$ in (4.2) strongly depends on both r and t. The main process by which photons are coupled to the matter is Compton scattering which conserves the number of photons. Since opacity is large other processes which do not conserve the photon number lead to local thermodynamic equilibrium with thermal comoving radiation intensity $I_c = J$[1], number density and spectrum of photons in the outflow. Hence we use the Rosseland radiative diffusion approximation (see e.g. [61], pp. 39–42), that we now derive

[1]To avoid excessive usage of subscripts c in this section, comoving radiation intensity I_c and comoving source function $\mathcal{I}_c$ are referred to as J and S, respectively.

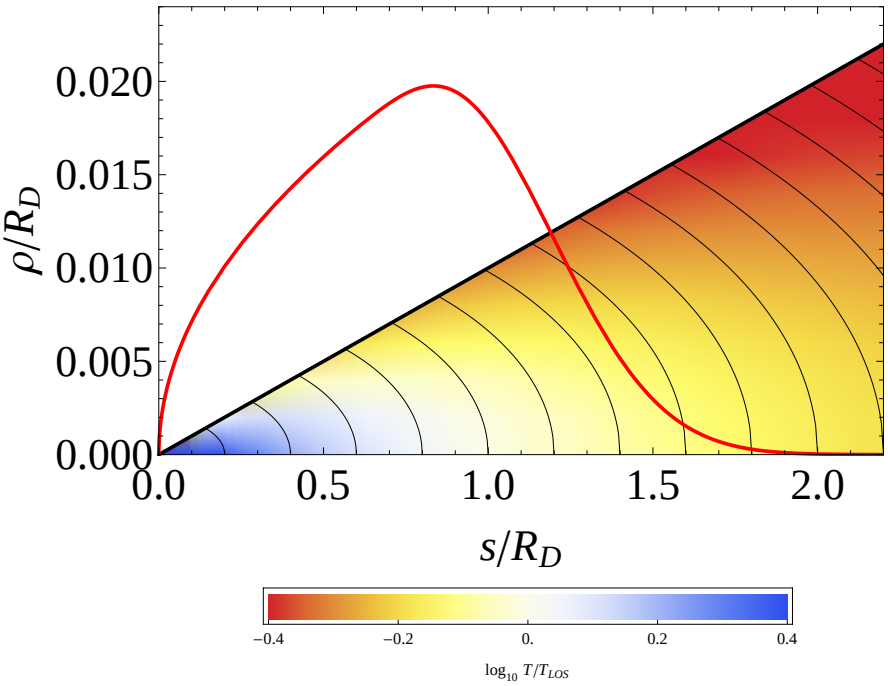

Figure 4.8: Evolution of PhE for the photon thin coasting outflow and dimensionless radiative diffusion flux, corrected for adiabatic cooling (red thick curve). PhEs shown by thin curves correspond from left to right to arrival times $t_a = (t_a^D/5, 2t_a^D/5, \dots)$, see (4.26). Thick black curve bounding PhEs correspond to the surface $\cos\theta = \beta$. Relevant range of observed temperature of photospheric emission is illustrated by color, see legend. Here $\Gamma = 100$.

from the radiative transfer equations (4.1) for expanding outflows.

For large opacities the distribution function of photons in comoving reference frame is close to isotropic one and the radiative diffusion approximation is accurate. Following [25] we use spectral intensity in comoving frame $J_\nu(t,\xi,\mu)$. Starting from the radiative transfer equation (4.1) along the ray s in laboratory frame, we transform all variables except time t, depth ξ, and distance s into comoving reference frame

$$\nu^3 \frac{d}{ds}\left(\frac{J_\nu}{\nu^3}\right) = \frac{\kappa_\nu}{\mathcal{D}}(S_\nu - J_\nu), \tag{4.16}$$

and integrating over comoving frequency ν we have

$$\frac{1}{c}\frac{\partial J}{\partial t} - \frac{\mu}{\Gamma\mathcal{D}}\frac{\partial J}{\partial \xi} + \frac{1-\mu^2}{vt-\xi}\frac{\partial J}{\partial \mu} + 4\frac{\Gamma\beta}{\mathcal{D}}\frac{1-\mu^2}{vt-\xi}J = \frac{\kappa}{\mathcal{D}}(S-J), \tag{4.17}$$

where $\mu = \cos\theta_c$, θ_c is the photon angle with respect to the radial direction in comoving frame, $\mathcal{D} = \Gamma(1+\beta\mu)$ is Doppler factor, $J = \int J_\nu d\nu$ is total photon intensity, $S = \int S_\nu d\nu$ is total source function, $\kappa = J^{-1}\int \kappa_\nu J_\nu d\nu$ is effective opacity, $\kappa_\nu = \sigma n_c$ is opacity in comoving frame.

In the case of small deviations from isotropy decomposition

$$J = J_0(t,\xi) + \mu J_1(t,\xi) \tag{4.18}$$

could be applied. Introducing it into (4.17) and integrating it over $\mathcal{D}d\mu$ and over $\mathcal{D}\mu d\mu$ after some algebra for coherent scattering with $S = S_0 = J_0$ we have

$$\frac{\partial J_0}{\partial ct} + \frac{\beta}{3}\frac{\partial J_1}{\partial ct} - \frac{1}{3\Gamma^2}\frac{\partial J_1}{\partial \xi} + \frac{2J_1}{3(vt-\xi)} + \frac{4J_0\beta}{3(vt-\xi)} = 0, \tag{4.19}$$

$$\frac{\partial J_1}{\partial ct} + \beta\frac{\partial J_0}{\partial ct} - \frac{1}{\Gamma^2}\frac{\partial J_0}{\partial \xi} + \frac{8J_1\beta}{5(vt-\xi)} = -\frac{\kappa J_1}{\Gamma}. \tag{4.20}$$

Diffusion approximation is based on slow variation of total flux through the entire sphere $L_1 = J_1(t/t_0)^2$ over mean free path, so that $\frac{\partial L_1}{\partial ct} = 0$, and it provide J_1 from the equation (4.20). Inserting this into (4.19) after simple but tedious calculations in ultrarelativistic $\beta \simeq 1$ photon thin case $\Gamma^2\xi \ll vt$ for function $L = J_0(t/t_0)^{8/3}$, which effectively accounts for the adiabatic cooling of radiation

in expanding outflow, we obtain the diffusion equation

$$\frac{\partial L}{\partial ct} - \frac{c^2 t^2 \Delta}{3R_0}\frac{\partial^2 L}{\partial \xi^2} = 0, \qquad \Delta = \frac{1}{\Gamma^2 \sigma n_0 R_0} = \frac{1}{\Gamma^2 \tau_0}. \tag{4.21}$$

Notice that the diffusion coefficient is explicitly time dependent due to the expansion of the outflow.

This equation should be supplemented with boundary conditions. There are two types of boundary conditions used frequently: free-streaming, for example in two-stream approximation ([61], pp. 42–45), and zero boundary conditions, that can be used as replacement for free-streaming for "extrapolated boundary" [123]. We find that the position of "extrapolated boundary" $\xi = -k\frac{c^2 t^2 \Delta}{R_0}$ (k is a constant of order unity, dependent on the approximation used for free-streaming description) for the main part of emission is very close to the real boundary, and in the case of zero boundary conditions $L|_{\xi=0} = L|_{\xi=l} = 0$ there is a series expansion of solution, that for initial conditions $L(\xi, t_0) = 1$ gives

$$L(\xi, t) = \sum_{n=0}^{\infty} \frac{4}{(2n+1)\pi} \sin\left[\frac{(2n+1)\pi\xi}{l}\right] \times \exp\left[-\frac{\Delta(2n+1)^2\pi^2 c^3 (t^3 - t_0^3)}{9R_0 l^2}\right]. \tag{4.22}$$

This solution in comparison with numerical one with free-streaming boundary conditions is accurate to a few percents and is shown in Fig. 4.9.

The flux of L is characterized by an initial burst and then tends to the asymptotic solution, that corresponds to $t_0 = 0$, with flux

$$F(t) = \frac{4\Delta c^3 t^2}{3R_0 l^2}\ \vartheta_2\left[0, \exp\left(-\frac{4\Delta\pi^2 c^3 t^3}{9R_0 l^2}\right)\right], \tag{4.23}$$

where ϑ_2 is the Jacobi elliptic theta function, see Fig. 4.8. The peak of the flux of L is near the diffusion time

$$t_D = \frac{l}{c}\left(\frac{R_0}{l\Delta}\right)^{1/3}, \tag{4.24}$$

and "extrapolated boundary" $\xi = -kl(l\Delta/R_0)^{1/3} \ll l$ is very close to real one as $\Delta \ll 1$, that ensures the accuracy of (4.22). This diffusion time exactly corresponds to the diffusion radius, obtained in Sec. 4.3.

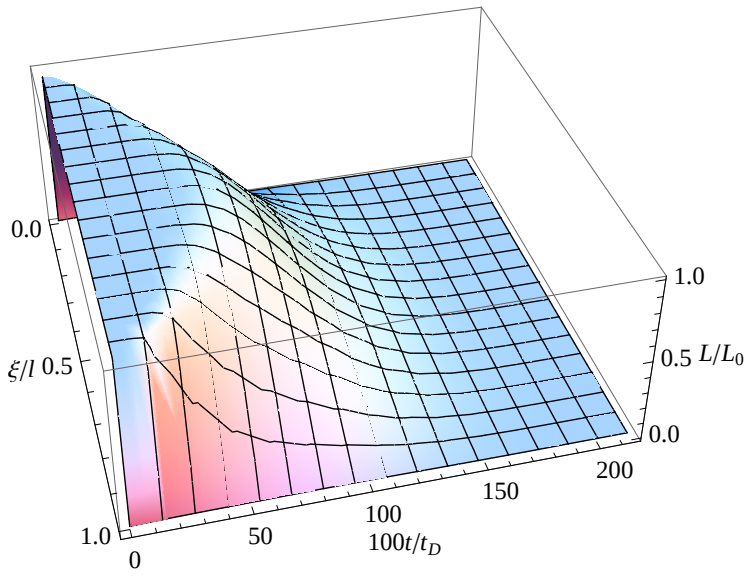

Figure 4.9: Solution to diffusion of comoving radiation intensity corrected for the adiabatic cooling $L(\xi, t)$ from initial homogeneous distribution.

The raising part of the corresponding flux of L through the external boundary of the outflow scales as $t^{1/2}$, while its decaying part is quasi-exponential one. Consequently, while the diffusion in a static object gives the flux decreases as $t^{-1/2}$, in our case the observed flux (4.3), shown in Fig. 4.10, is a more slowly decreasing function

$$F \propto t_a^{-1/6}, \tag{4.25}$$

up to arrival time of diffusion

$$t_a^D = \frac{R_D B^2}{2c} \simeq 0.12 E_{54}^{1/3} B_{-2}^{5/3} l_8^{1/3} \text{ s}, \tag{4.26}$$

where large part of energy has left the outflow already. At this moment the energy decrease due to diffusion becomes substantial even in the deepest parts of the outflow and later the observed flux decreases quasi-exponentially with arrival time.

The comoving temperature of radiation on the photosphere is determined by the balance between the energy diffusion from the interior of the outflow and radiative losses and it is much smaller than the temperature in the interior. The variation of observed temperature across the PhE is small, see Fig. 4.8, and

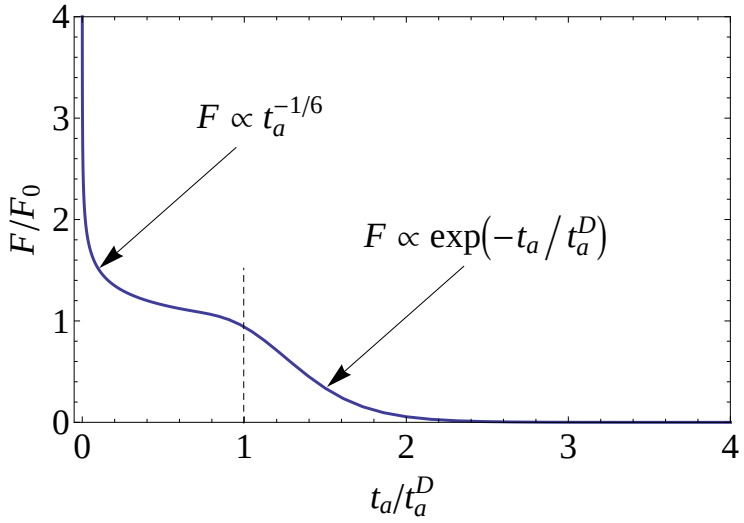

Figure 4.10: Lightcurve of observed photospheric emission from the photon thin outflow.

hence the observed instantaneous spectrum is very close to the thermal one and peaks near the observed temperature on the line of sight. We find that the latter decreases as $t_a^{-13/24}$, in contrast with adiabatic law $t_a^{-2/3}$. However, at diffusion radius both temperatures coincide, giving for the line of sight temperature

$$T_{LOS} \simeq 162 B_{-2}^{-4/9} \text{ keV}, \tag{4.27}$$

with very weak dependence on the other parameters of the outflow. The time integrated spectrum has a Band shape with a cut-off near the temperature of transition from acceleration to coasting, see Fig. 4.11. Low energy part of the spectrum has the slope varying in the range from $\alpha \simeq 0$ near the maximum to $\alpha = 1$ asymptotically far in low energies, while high-energy part has $\beta = -46/13 \simeq -3.5$.

4.6 Discussion

Firstly we compare the results of Sec. 4.4 for photon thick outflows with those obtained by other methods. The photospheric emission from infinitely long wind both at acceleration and coasting phases was considered in [25] by the solution of the corresponding *steady* radiative transfer equation. The main conclusion of that work is that in addition to usual relativistic beaming leading to anisotropy of radiation in laboratory frame, in the coasting wind another anisotropy in the

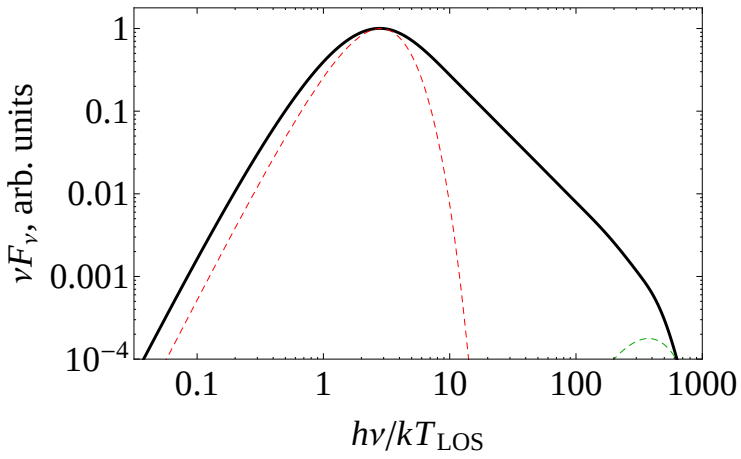

Figure 4.11: Time-integrated spectrum of photospheric emission of photon thin outflow (thick curve, $\eta = 100$, $R_D = 10^5 R_0$), superimposed with two instantaneous spectra of that emission, corresponding to arrival time of photons emitted at the moment of transition from acceleration to coasting (dashed green curve on the right) and to arrival time of diffusion (dashed red curve on the left).

comoving frame of the outflow is developing. This comoving anisotropy results from the fraction of photons which already underwent their last scattering in the bulk photon field of the outflow. The anisotropy of such photons grows with increasing radius for geometrical reasons. Since the amount of such photons increase with radius the entire photon field becomes increasingly anisotropic.

For the finite photon thick outflow the radiative transfer problem becomes explicitly time dependent. The expanding outflow at a given laboratory time spans only a finite part of the probability density distribution shown in Figs. 4.2 and 4.3, that results in difference in observed spectra for finite and infinite cases. Interesting consequence of ultrarelativistic motion of the outflow is that even geometrically thin outflow $l \ll R$ at a given arrival time spans large interval of laboratory radius $\Delta r = 2\Gamma^2 l$.

The effect of additional comoving anisotropy on the source function found in [25] is actually small. The difference between the probability of last scattering (4.5) and the distribution of last scattering in a steady wind found in [25] does not exceed several percent.

Our method is also similar to the one used in [23] and [26] to describe the late-time photospheric emission of switching off relativistic wind considering the probability density function (4.5) for the last scattering of photons. An addi-

tional approximation adopted by these authors is the possibility to split radial and angular dependencies. Actually in [23] not the traditional energy flux understood as energy crossing unit area in unit time was computed, but photon flux as number of photons crossing unit area in unit time. For this reason the decay law for photon flux at late times was found to be $F^{ob}(t_a) \propto t_a^{-2}$. Lorentz transformation of the photon energy from the comoving frame to the laboratory one results in additional multiplier $(1-\beta\mu)^{-1}$ in the energy flux that leads to the observed flux $F \propto t_a^{-3}$, which agrees with our result in Eq. (4.15), see also [26].

We conclude that the fuzzy photosphere approximation in fact follows closely the methods of [26] and [25]. In fact we obtained similar results for the probability of last scattering as more sophisticated treatment of radiation transfer [25]. The sharp photosphere approximation provides good description of light curves including their raising and decaying parts. The observed spectrum from accelerating outflow is also well described in this approximation, while there is some difference for the coasting case. The advantage of sharp photosphere approximation for computing observed light curves and spectra is evident for intrinsically variable and dynamic outflows.

Now turn to the photospheric emission of photon thin outflows. The expression (4.26) gives an estimate for duration of photospheric emission of photon thin outflows. When available observed spectra are integrated on time intervals comparable to (4.26) the observed spectrum of photospheric emission is expected to have Band shape. Thus, starting from comoving thermal spectrum for the photospheric emission we obtain for the first time an observed spectrum which may be well described by the Band function with high energy power law index β being determined by the density profile of the outflow. We find this result quite remarkable.

Notice that non thermal spectra as a result of convolution of thermal ones over time has been introduced for afterglows of GRBs by [124]. Double convolution over EQTS and arrival time is also one of the key ideas in the fireshell model [13].

Band spectra in photospheric models of GRBs have been obtained by now only assuming additional dissipation mechanisms such as magnetic reconnection [22], collisional heating [24] and internal shocks [93, 125]. In our model such additional assumption is not required.

It is even more remarkable that GRBs appear to be the only known objects

in nature able to reach the photon thin asymptotics in their ultrarelativistic expansion. For thermally accelerated relativistic plasmas which are discussed in connection with their possible synthesis in ground based laboratories (e.g. [5]) it is unreachable. The photon thin asymptotics is reached if the optical depth (3.51)

$$\tau_0 \gg 4\Gamma^4 \frac{l}{R_0} = 4 \times 10^8 B_{-2}^{-4} \frac{l_8}{R_8}. \tag{4.28}$$

GRBs clearly can satisfy this constraint as the contribution of baryons $\tau_0 \simeq 3.5 \times 10^{13} E_{54} B_{-2} R_8^{-1} l_8^{-1}$.

We obtained both time integrated and instantaneous spectra of accelerating photon thick outflow which are close to thermal one with small deviations in the Rayleigh-Jeans part, in agreement with [85].

Time integrated observed spectrum of coasting photon thick outflow is broader than thermal one, and deviates from it both in low- and high-energy parts. This broadening is also found by [24] using Monte-Carlo simulations, and our results agree for a model of isotropic scattering, giving spectral index of the low energy part as $\alpha = 0$. We reproduced this result in our own Monte-Carlo code [126]. Taking further into account final radial extension of the outflow in the code we confirm main emission properties found in [89] and presented in this Chapter by an independent method.

As discussed earlier in Sec. 3.8 each photon thick outflow always contains a photon thin layer with depth $\xi_{thin} = (R + l)B^2/2$ located near its outer boundary. Radiation diffused out from this part of the outflow arrives to observer first and modifies the initial part of the light curve and the corresponding spectrum of the outflow. The diffusion length $\xi_D = \left[(R + l)^3 B^2/(\tau_0 R_0)\right]^{1/2}$ remains always within this photon thin layer ξ_{thin} and our solution for photon thin outflow is applicable for description of this early emission. The photospheric emission from well developed photon thick outflow and its late time behavior occurring when the outflow crossed the photospheric radius may be described either by fuzzy or by sharp photosphere approximations.

When the outflow becomes transparent in the transition from photon thick to photon thin conditions, the observed time integrated spectrum will contain both Band component produced by the early emission from the photon thin layer and thermal-like component coming from the photon thick part superimposed. This may be the reason why in most GRBs analyzed by [119] there are both power

law and black body components.

We presented analytic expressions for the photon flux in the simple model of the finite wind (2.29). With more complex density, velocity and energy profiles of the outflow the light curve is expected to be variable and arbitrarily complex. The minimal time scale of variability is given by Eq. (4.26) and it may be very small for small baryon loading. It is necessary to emphasize that the decaying part of the light curve follows t_a^{-3} for photon thick outflows. Steeper decay of the light curve of photospheric emission is a clear signature of the photon thin outflow.

The photospheric emission should be additionally identified by the spectral analysis. In particular, power law spectra extending to high energies above 10 MeV cannot be produced by the photospheric emission unless additional mechanisms are involved. What we have shown here, though, is that the observed spectrum may not necessarily be close to the thermal one.

4.7 Conclusions

In summary, in this Chapter we proposed a unified treatment of photospheric emission of ultrarelativistic outflows, which originate in finite wind and thin shell models of GRBs. Instead of the traditional division into steady winds and thin shells we propose a new physically motivated classification, which in our opinion helps to understand in particular why geometrically thin shell may appear as thick wind with respect to the photospheric emission. For this reason we re-examined the existing scattered literature and pointed out the advantage of the proposed classification.

We studied geometry of photospheres in generic relativistic outflows. As we are interested in appearance of the photosphere to a distant observer, we introduced the notion of photospheric equitemporal surface and described its dynamics.

We computed both energy flux and observed spectra of photon thick outflows in two approximations, derived from the radiative transfer equation. In our fuzzy photosphere approximation the effect of simultaneous emission from entire volume of the outflow is taken into account. We also used a more crude, but computationally more simple sharp photosphere approximation which is shown to reproduces well both light curves and spectra. These results generalize the corresponding results in the literature for steady relativistic winds.

In photon thin outflows most of radiation is shown to originate not at its transparency radius, but at smaller radii due to radiation diffusion. Starting from the radiative transfer equation for time dependent outflows we derived the diffusion equation and obtained approximate analytic solution for the energy flux. We present both instantaneous and time integrated observed spectra. The latter are well described by the Band function. For our simple density profile we find values for the low energy power law index $\alpha = 1$ and the high-energy power law index $\beta \simeq -3.5$.

Chapter 5

Semidegenerate self-gravitating system of fermions as a model for galactic dark matter and universality laws

Dark matter properties are constrained both from cosmology and astrophysics. Cosmological bounds are based on the assumptions on cross sections of interaction between the dark matter particles and usual matter plus interaction between dark matter particles themselves. Usually it appears that dark matter decouple from normal matter at thermal equilibrium and at the same time or earlier interaction between dark matter particles themselves come to a halt, so that they form collisionless dark matter. In this case mass density of the particles can be found and compared to the known dark matter cosmological density. This provides different limits on the mass of dark matter particles, two of them being Gershtein-Zeldovich limit for the sum of light neutrino masses [127]

$$\sum_i m_{\nu_i} < 94 \text{ eV/c}^2, \tag{5.1}$$

and Gunn-Tremaine lower bound on the neutrino mass if neutrinos make up the dark matter in galaxy halos is [128]

$$m_\nu > k(Gh^3 v_{rms} r^2)^{-1/4}, \tag{5.2}$$

where k is a factor of order unity, G is the Newton gravitational constant, h is the Planck constant, v_{rms} is the root mean square velocity, and r is the radius of the halo, respectively. Application of the Gunn-Tremain limit to dwarf spheroidal satellites of the Milky Way gives [129]

$$m_\nu \gtrsim 300 \text{ eV/c}^2. \tag{5.3}$$

Different approach to the study of properties of dark matter is coming from cosmology and specially from theories of galaxy formation and evolution. While studies of CMB allow to constrain number and masses of light neutrinos representing hot dark matter [130], properties and masses of warm and cold dark matter are constrained by the total mass density of the Universe [131] and galactic halos structure [128] and substructure [132]. The Lee-Weinberg bound [131] limits the mass of dark matter particles with given coupling constant from above implying that particle was in thermal equilibrium in early Universe. For typical weak interaction coupling G_F mass is constrained to be more than ~ 2 GeV/c^2 and such particles is referred to as Weakly Interacting Massive Particles, WIMPs. Bound by [128] and its improvement by many authors [133, 134] are based on assumption of fermionic nature of dark matter and nondegeneracy of galactic haloes of dwarf galaxies, that leads to lower limit on mass ~ 0.41 keV/c^2.

The problem of dark matter distribution in galactic halos has traditionally been treated in the realm of newtonian physics in view of the low velocities of the stars in the galaxies, like the simulations from [135]. In the meantime, phenomenological profiles of dark matter have been advanced by [136, 137], and universal properties of the dark matter distribution have been inferred from dwarf galaxies and probably globular clusters all the way to very massive galaxies [42, 43, 45, 138]. However, a problem arises: while simulations like those from NFW point to a cusped halo, observations from various types of galaxies seem to show cored halos [139]. This discrepancy between theory and observations is not yet fully understood, but could show a problem with the simulations done so far.

In a completely unrelated field (as of yet), the physics of Active Galactic Nuclei (AGN) and quasars has been recognized for more than 50 years as dominated by relativistic gravitational effects of a black hole. The formation of these black holes is not yet fully understood, although different black holes mass estimates for AGNs and quasars show masses up to $10^{10}\ M_\odot$ all the way to $z \approx 6.4$

[140–143]. Due to the lack of understanding on the energetics of AGNs and quasars and on the formation of the black holes, the possibility of an extended object in the core of galaxies has been advanced by [144].

The aim of this Chapter is to present a unified approach to the dark matter distribution in the galactic halos and also in the galactic center following [145]. In order to do that, some assumptions have been made:

1. The treatment must be general relativistic from the beginning, in order to explain both the galactic nuclei and galactic haloes.

2. The matter particles are assumed to be semi-degenerated fermions and so obey the Fermi-Dirac statistics.

3. Configurations are in relativistic thermal equilibrium $\sqrt{g_{00}}T = \text{const}$ or sufficiently close to it.

5.1 Model of halo

The equilibrium configurations of a self-gravitating semi-degenerate system of fermions were studied by [39] in Newtonian gravity and by [40] in general relativity. It is shown that in any such system the density at large radii scales as r^{-2} quite independently of the values of the central density, providing flat rotation curve. Then solution was extended to an energy cutoff in the distribution function [41].

Following [40] we are considering spherical symmetry, the line element is written in standard Schwarzschild coordinates as

$$ds^2 = -e^{\nu(r)}dt^2 + e^{\lambda(r)}dr^2 + r^2(d\theta^2 + \sin^2\theta d\phi^2). \tag{5.4}$$

The equilibrium equations are given by

$$\frac{dP}{dr} = -\frac{G}{c^2}\frac{(P+\rho c^2)(M(r)+4\pi\rho r^3)}{r(rc^2-2GM(r))} \tag{5.5}$$

$$\frac{dM}{dr} = 4\pi\rho r^2, \tag{5.6}$$

with M the mass within a radius r, ρ and P the energy density and the pressure

respectively, given by

$$\rho = m\frac{g}{h^3}\int_0^{\epsilon_c}\left(1+\frac{\epsilon}{mc^2}\right)\frac{1-e^{(\epsilon-\epsilon_c)/kT}}{e^{(\epsilon-\mu)/kT}+1}d^3p \tag{5.7}$$

$$P = \frac{2g}{3h^3}\int_0^{\epsilon_c}\left(1+\frac{\epsilon}{2mc^2}\right)\left(1+\frac{\epsilon}{mc^2}\right)^{-1}\frac{(1-e^{(\epsilon-\epsilon_c)/kT})\epsilon}{e^{(\epsilon-\mu)/KT}+1}d^3p, \tag{5.8}$$

with ϵ_c being the cutoff energy, $g = 2s+1$ being the spin weights, m being the mass of the particle, and T being the temperature and μ the chemical potential. The volume element in momentum space can be expressed in terms of the kinetic energy ϵ of the particles as

$$d^3p = 4\pi p^2dp = 4\sqrt{2}m^3c^3\sqrt{1+\frac{\epsilon}{2mc^2}}\left(1+\frac{\epsilon}{mc^2}\right)\sqrt{\frac{\epsilon}{mc^2}}\,d\frac{\epsilon}{mc^2}. \tag{5.9}$$

The particle energy is a constant of motion, so

$$(\epsilon + mc^2)e^{\nu/2} = const, \tag{5.10}$$

while thermodynamical equilibrium (Tolman condition and Klein integral [146]) implies

$$(\mu + mc^2)e^{\nu/2} = (\mu_R + mc^2)e^{\nu_R/2} \tag{5.11}$$

$$Te^{\nu/2} = T_Re^{\nu_R/2}, \tag{5.12}$$

where the quantities with subscript "R" refer to the boundary of the configuration. For the cutoff energy we have

$$(\epsilon_c + mc^2)e^{\nu/2} = mc^2e^{\nu_R/2}, \tag{5.13}$$

since $\epsilon_c(R) = 0$.

Introducing the function $W = \epsilon_c/kT$ and the temperature parameter at the boundary $\beta_R = kT_R/mc^2$, and using eqs. (5.12) and (5.13) we can find that

$$\frac{mc^2}{kT} = \frac{1-\beta_RW}{\beta_R}. \tag{5.14}$$

Note that the condition $0 \leq \beta_RW < 1$ has to be fulfilled. Using eq. (5.12) to

substitute the temperature in eq. (5.11) we get the relation between the metric function ν and W:

$$e^{\nu} = e^{\nu_R}(1 - \beta_R W)^2 \tag{5.15}$$

so now the spacetime metric is completely determined:

$$e^{\nu} = e^{\nu_R}[1 - \beta_R W]^2, \qquad e^{\lambda} = \left(1 - \frac{2GM}{rc^2}\right)^{-1} \tag{5.16}$$

with $\nu_R + \lambda_R = 0$.

Differentiating Eq. (5.15) and using the conservation of the energy momentum tensor

$$\frac{dP}{dr} = -\frac{1}{2}(P + \rho c^2)\frac{d\nu}{dr} \tag{5.17}$$

gives

$$\frac{dP}{dr} = \frac{\beta_R(P + \rho c^2)}{1 - \beta_R W}\frac{dW}{dr} \tag{5.18}$$

and we can write Eq. (5.5) as

$$\frac{dW}{dr} = -\frac{G}{c^2}\left[\frac{1 - \beta_R W}{\beta_R}\right]\frac{Mc^2 + 4\pi P r^3}{r(rc^2 - 2GM)} \tag{5.19}$$

In order to numerically integrate the final set of equations (5.6) and (5.19) with initial conditions $W(0) = W_0$ and $M(0) = 0$, it is useful to transform all of our physical variables into dimensionless ones:

$$\rho = \frac{c^2}{G\chi^2}\hat{\rho} \tag{5.20}$$

$$P = \frac{c^4}{G\chi^2}\hat{P} \tag{5.21}$$

$$M = \frac{c^2\chi}{G}\hat{M} \tag{5.22}$$

$$r = \chi\hat{r}, \tag{5.23}$$

where

$$\chi = \frac{\hbar}{mc}\left(\frac{m_p}{m}\right)\left(\frac{8\pi^3}{g}\right)^{1/2} \tag{5.24}$$

has dimension of length and $m_p = (\hbar c/G)^{1/2}$ is the Planck mass.

It is instructive to write down characteristic length χ, that is inversely proportional to square of the mass of the particle, in conventional units

$$\chi = 0.870 m^{-2} \text{ pc}, \tag{5.25}$$

where m is measured in keV/c^2, and unit of mass is

$$\frac{c^2\chi}{G} = 1.820 \times 10^{13} m^{-2} M_\odot, \tag{5.26}$$

where $M_\odot = 1.989 \cdot 10^{33}$ g is mass of the Sun.

We then obtain the dimensionless equations

$$\begin{aligned} \frac{dW}{d\hat{r}} &= -\left[\frac{1-\beta_R W}{\beta_R}\right]\frac{\hat{M}(r)+4\pi\hat{P}\hat{r}^3}{\hat{r}(\hat{r}-2\hat{M}(r))} \\ \frac{dM(r)}{dr} &= 4\pi\hat{\rho}\hat{r}^2, \end{aligned} \tag{5.27}$$

where

$$\begin{aligned} \hat{\rho} &= 4\sqrt{2}\pi\left[\frac{\beta_R}{1-\beta_R W}\right]^{3/2} \\ &\quad \times \int_0^W \left[1+\frac{\beta_R x/2}{1-\beta_R W}\right]^{1/2}\left[1+\frac{\beta_R x}{1-\beta_R W}\right]^2 \frac{1-e^{x-W}}{e^{x-\theta}+1}x^{1/2}dx \\ \hat{P} &= \frac{8\sqrt{2}}{3}\pi\left[\frac{\beta_R}{1-\beta_R W}\right]^{5/2}\int_0^W \left[1+\frac{\beta_R x/2}{1-\beta_R W}\right]^{3/2}\frac{1-e^{w-W}}{e^{x-\theta}+1}x^{3/2}dx, \end{aligned} \tag{5.28}$$

where $\theta = \mu/kT$ is the degeneracy parameter and we introduced the variable $x = \epsilon/kT$. We have for this variable

$$\frac{\epsilon}{mc^2} = \frac{\beta_R x}{1-\beta_R W}. \tag{5.29}$$

The relation between the degeneracy parameter θ and W is

$$W = \theta - \theta_R, \tag{5.30}$$

so that $W(R) = 0$, where θ_R is the value of the degeneracy parameter at the boundary. We can relate the parameters in the boundary with those in the center

$$\theta_R = \theta_0 - W_0 \qquad \beta_R = \frac{\beta_0}{1 + \beta_0 W_0} \tag{5.31}$$

so that $\beta_R \approx \beta_0$ for $\beta_0 << 1$. Besides that we have

$$\frac{1 - \beta_R W}{\beta_r} = \frac{1 - \beta_0 (W - W_0)}{\beta_0}. \tag{5.32}$$

Now the system can be completely solved (numerically) by solving the Eqs. (5.27) together with

$$\theta = \theta_0 + W - W_0 \tag{5.33}$$

and using Eq. (5.28) with three independent parameters: W_0, θ_0 and β_0. The only remaining free parameter is the mass of the particle, which occurs only in the definition of β and the characteristic length χ.

5.1.1 Properties of the equilibrium configurations

We have solved numerically the system of integral-differential equations given by (5.19), the two equations corresponding to β and θ and (5.28), with a set of initial conditions M_0, W_0, β_0 and θ_0. Galactic dark matter halos have asymptotic rotation velocities of the order of ten to thousands km/s, i.e., they are not relativistic. As that velocities are of the same order as thermal velocities of fermionic particles forming the halo, this means that $\beta_R \ll 1$ and consequently $\beta_0 \ll 1$. For semidegenerate configurations $\theta_0 \gtrsim 20$, and in this case we have three regions of halo (fig. 5.1): a degenerate core of almost constant density, an inner halo also with almost constant density and a tail where density scales as r^{-2} until the cutoff.

On the velocity curve, we can see 4 characteristic regions (fig. 5.2):

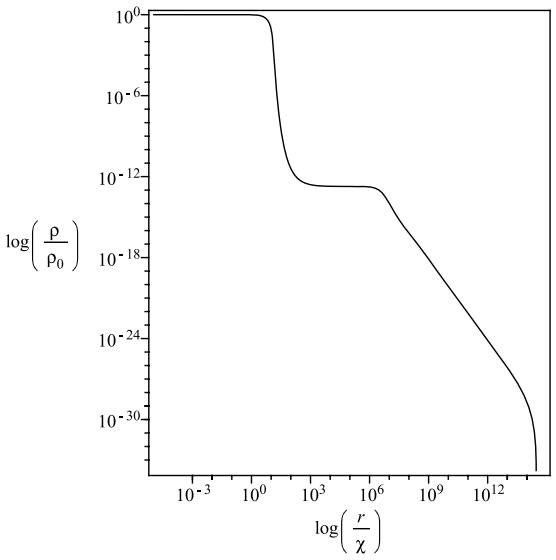

Figure 5.1: Density profile of the model for $\beta_0 = 10^{-8}$, $\theta_0 = 32$ and $W_0 = 92$.

- Part I: The core with constant density, where $v \propto r$;
- Part II: The first part of the inner halo, where the mass of the core prevails over the mass of the halo and $v \propto r^{-1/2}$;
- Part III: Second part of the inner halo, where now the mass of the halo prevails and again $v \propto r$;
- Part IV: The outer halo, where the velocity tends to a constant value v_0 after some oscillations of diminishing magnitude.

5.2 Comparison with other phenomenological and theoretical dark matter profiles

To compare results obtained with known Dark Matter properties we need to find out the correspondence between fits of circular velocity, much like it was suggested in [138]. There is some controversy in current literature about the undisturbed profile of dark matter in Galaxies and clusters. Cold dark matter simulations suggest the so-called Navarro-Frenk-White profile [135]

$$\rho = \frac{\rho_{NFW}}{r/r_{NFW}(1 + r/r_{NFW})^2} \tag{5.34}$$

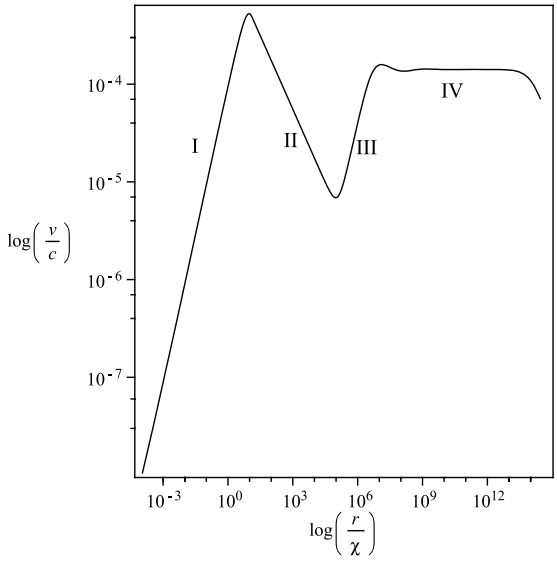

Figure 5.2: Velocity curve for the same parameter values as before

and Einasto profile [147] introduced by J. Einasto for modeling of matter distribution in Milky Way [136]

$$\rho = \rho_E \exp\left(-\frac{2}{\alpha}\left[(r/r_E)^\alpha - 1\right]\right) \tag{5.35}$$

while phenomenological pseudoisothermal sphere

$$\rho = \frac{\rho_{iso}}{1 + (r/r_{iso})^2} \tag{5.36}$$

and Burkert profile [137]

$$\rho = \frac{\rho_B}{(1 + r/r_B)(1 + (r/r_B)^2)}. \tag{5.37}$$

are commonly used for fitting. Comparing profiles of circular velocity for all these profiles with the one of the semidegenerate solution, we came to conclusion that NFW and Burkert profiles, having wrong asymptotics as $r \to \infty$, better reproduce the characteristic "bump" in the circular velocity near the edge of inner halo (fig. 5.3). The best reproduction is obtained for Burkert profile. As most of papers dealing with rotational curve fitting find out that Burkert or other cored profiles are the best fits for dark matter distribution, and that characteristic scale r_B of the fitted profile is comparable to the full length of fitting range

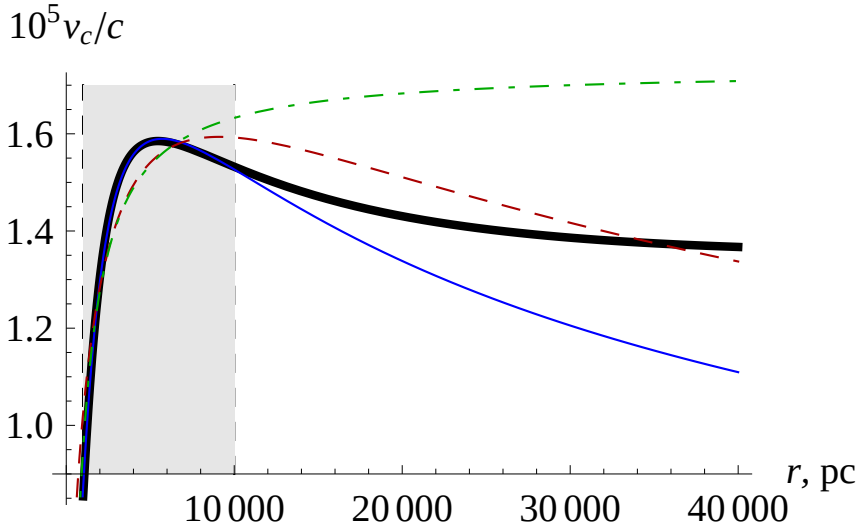

Figure 5.3: Dependence of v_c/c on radius r (black thick line) for $\beta = 10^{-10}$, $\theta_0 = 20$, $m = 9.3$ keV/c^2 near the edge of the inner halo and its fits by NFW (red dashed line), Burkert (blue thin line) and pseudoisothermal sphere (green dot-dashed line) profiles. The radius range used for fitting is shown by grey shading ($r = 10^3$ to $r = 10^4$ pc).

(see, e.g., [148]), that means that semidegenerate fermion halo can provide the same quality of fits for that galaxies.

As we move outside from the border of inner/outer halo, the fits by pseudoisothermal sphere became better than that of other profiles (fig. 5.4). The fits by other profiles suffer due to their different outer slope, so constant circular velocity can be only approximated in a finite range of radii by a decreasing function. As a result we have systematic deviations from the real flat curve in the beginning and the end of fitting range.

The result obtained means that all fits of rotational curves by Burkert, NFW and pseudoisothermal sphere profiles could be fitted as well by semidegenerate fermion halo.

5.3 Scaling laws of dark matter distribution

The solutions obtained show remarkable self-similarity properties. The characteristics of solutions obey five scaling laws against the free parameters of the model β_0, θ_0, W_0 and m_f. These are laws for the asymptotic velocity of the rotation curves, for the core mass, for the core radius, for the halo mass and for the

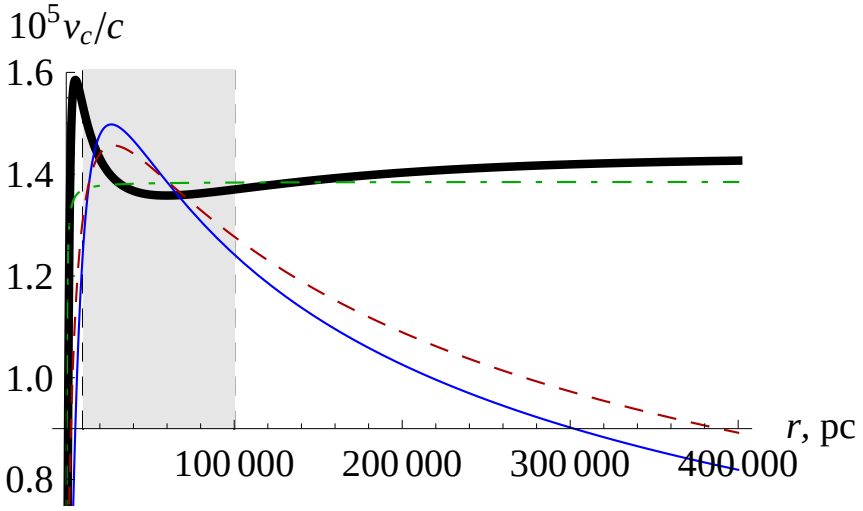

Figure 5.4: Dependence of v_c/c on radius r (black thick line) for $\beta = 10^{-10}$, $\theta_0 = 20$, $m = 9.3$ keV/c^2 in the outer halo and its fits by NFW (red dashed line), Burkert (blue thin line) and pseudoisothermal sphere (green dot-dashed line) profiles. The radius range used for fitting is shown by grey shading ($r = 10^4$ to $r = 10^5$ pc).

halo radius.

Asymptotic rotation velocity scaling law

$$v_0 = 4.07 \times 10^5 \sqrt{\beta_0}\ \mathrm{km/s} \tag{5.38}$$

show dependence on the temperature of the configuration only. This is essentially the same scaling law that appears in the case of isothermal sphere [149].

Core is defined as region from the center of the system till the first maximum of the rotation velocity curve, position of which will be referred to as core radius r_c (region I in fig. 5.2). Near that point the density of fermions decreases fast, and rotational curve become Keplerian

$$v_{rot} = \sqrt{\frac{GM_c}{r}}. \tag{5.39}$$

Core mass was found by fitting of rotational curve in the inner halo region by Eq. (5.39). Radial range adopted for fitting is chosen to be $r \in [r_c^{3/4} r_m^{1/4}, r_c^{1/4} r_m^{3/4}]$, where r_m is the position of minimum of rotational curve. Scalings of mass and

radius of the core are

$$M_c = 4.30 \times 10^{12}\, \beta_0^{0.750} \theta_0^{0.737} m_f^{-2}\ M_\odot \quad \simeq 4.07 \times 10^{12} (\beta_0 \theta_0)^{3/4} m_f^{-2}\ M_\odot, \tag{5.40}$$

$$r_c = 0.1972\, \beta_0^{-0.250} \theta_0^{-0.252} m_f^{-2}\ \mathrm{pc} \qquad \simeq 0.1954 (\beta_0 \theta_0)^{-1/4} m_f^{-2}\ \mathrm{pc}, \tag{5.41}$$

where m_f is in units of keV/c^2. Characteristics of core are dependent almost solely on the product $\beta_0\theta_0$, i.e. on the chemical potential μ at the semidegenerate center of configuration, in accordance with results of [150]. From the laws an important relation could be obtained, involving only M_c, r_c and m

$$M_c r_c^3 = 3.04 \times 10^{10} m_f^4\ M_\odot \mathrm{pc}^3. \tag{5.42}$$

Halo radius r_h is defined as the position of the second maximum on the rotational curve (transition form region III to region IV in fig. 5.2). Mass of the halo M_h is taken at the same point. Scaling laws of halo properties are

$$M_h = 4.42 \times 10^{13} {\beta_0}^{0.750} 10^{0.1597\,\theta_0} m_f^{-2}\ M_\odot, \tag{5.43}$$

$$r_h = 0.830 {\beta_0}^{-0.250} 10^{0.1598\,\theta_0} m_f^{-2}\ \mathrm{pc}. \tag{5.44}$$

Notice that instead of power-law dependence on θ_0 in core properties, halo properties depend on central degeneracy of configuration exponentially.

The equations above are exact in m_f and hold in the following physical range of the other parameters: $\log_{10}\beta_0 \in [-10, -5]$, $\theta_0 \in [20, 200]$, $W_0 \in [110, 200]$. Note that W_0 does not appear in the scaling laws, so that its value does not change inner structure of configuration.

5.3.1 Application to the Milky Way

In order to find out the order of semidegenerate halo parameters corresponding to observed ones, we adopted the four most reliable observed characteristics of the Milky Way, i.e. its asymptotic rotational velocity $v_0 \approx 220$ km/s, mass of the central object in the Galactic center $M_c \approx 4 \times 10^6\ M_\odot$, radius of Galactic halo $r_h \equiv r_0 \approx 14 \times 10^3$ pc, (r_0: one dark halo scale length) and its mass $M_h \approx$

$2 \times 10^{11}\ M_\odot$.

We take three equations corresponding to the number of three unknown parameters, namely (5.38), (5.43), and (5.40). Then solving the system using the data presented above we arrive to

$$\beta_0 = 10^{-6.6}, \tag{5.45}$$

$$\theta_0 = 32.4\ (W_0 = 130), \tag{5.46}$$

$$m_f = 12.6\ \text{KeV}. \tag{5.47}$$

Finally we can take the law (5.41) to obtain $r_c = 2.2 \times 10^{-2}$ pc. Although this value is quite far from the size of very compact region known as SgrA*, it is still in the very inner region of the bulge, in accordance with the observations of [151] and [152] made for orbits of S2(blue) stars, where can be seen that at a radius of around 1×10^{-2} pc the enclosed mass for the orbit must be around $4 \times 10^6\ M_\odot$.

5.3.2 Observational universality laws of dark matter distribution

Dark matter distributions in galaxies shows a number of relations between parameters of halos. One set of relations is especially interesting in the context of fermionic semidegenerate dark matter halos studied here—the set of recently discovered mass-radius relations. First relation was found in the works [42, 43]. Authors of the works analyzed dark matter halos of 28 galaxies: a sample of dwarf spheroidal galaxies (dSphs), two dwarf irregular galaxies, and two samples of spiral galaxies of various Hubble types, and found that parameters of Burkert DM profile used for fitting are correlated in such a way that dark matter surface density within one core radius is constant throughout the sample:

$$\rho_B r_B = \text{const} = 141^{+82}_{-52} M_\odot\ \text{pc}^{-2}. \tag{5.48}$$

As it was noted by the authors, this universality is equivalent to the constancy of gravitational acceleration by DM at r_B: $a_{DM}(r_B) = 3.2^{+1.8}_{-1.2} \cdot 10^{-9}$ cm·s^{-2}. This leads to the constancy of maximal acceleration by DM a_{max}, which is for Burkert DM profile is equal to $a_{DM}(r_B)$ to the accuracy better than 10^{-3}. Corresponding radius of a_{max} for Burkert DM profile $r_{max} = 0.963 r_B$ is very close to r_B. In globular clusters the similar behavior was found (see [153]), however the acceleration

is higher $a_{max} \sim 2 \cdot 10^{-8}$ cm·s^{-2}.

Scaling laws for a_{max} and r_{max} in the interval of parameters investigated are

$$a_{max} = 1.200 \times 10^3 \beta_0^{1.216} 10^{0.1612\theta_0} m_f^2 \text{ cm/s}^2, \tag{5.49}$$

and

$$r_{max} = 0.358 \beta_0^{-0.221} 10^{0.1612\theta_0} m_f^{-2} \text{ pc}. \tag{5.50}$$

Taken the number from [43], we arrive to the relation between temperature and central degeneracy parameters of the configuration

$$1.216 \lg \beta - 0.1612\theta_0 + 2 \lg m_f = -11.57. \tag{5.51}$$

While β is dependent on limit of circular velocity only (5.38), this relation allows us to find the second parameter θ_0 from observed surface densities

$$\theta_0 = -13.1(-18.0) + 12.4 \lg m_f + 15.1 \lg \frac{v_\infty}{\text{km/s}}, \tag{5.52}$$

where the number in parenthesis is for globular clusters and outside number is for galaxies.

For rotation curves v_∞ is in the range of $10 - 1000$ km/s and for 17 keV particle we have $\theta_0 \in [17, 47]$. In globular clusters the rotation curve is flattened at lower velocities, down to 3 km/s, but still the central degeneracy is high $\theta_0 \gtrsim 5$.

5.4 Conclusions

The equilibrium configurations of semidegenerate fermions with degenerate cores and nondegenerate halos provide natural explanation for both central concentration of mass in galaxies and extended halos probed by rotational curves. Observed discrepancy between radius and mass of the central object of our Galaxy and predictions of the model can be, in principle, accounted for by interaction of the particles and is the subject of the further work.

Conclusion

In Chapter 1 we considered thermalization of nonequilibrium optically thick pair plasma with energy density, relevant to the plasma in the GRB sources. We followed the evolution of plasma by integrating numerically relativistic Boltzmann equations with exact quantum electrodynamics two-particle and three-particle collision integrals. Quantum nature of particle statistics was accounted for in collision integrals by the corresponding Bose enhancement and Pauli blocking factors. We pointed out that unlike classical Boltzmann equation for binary interactions, more general interactions are typically described by four terms in collision integrals for each particle that appears both among incoming and outgoing particles. Our numerical results indicated that the rates of three-particle interactions become comparable to those of two-particle ones for temperatures exceeding the electron rest-mass energy. Thus three-particle interactions such as relativistic bremsstrahlung, double Compton scattering, and radiative pair creation become essential not only for establishment of thermal equilibrium, but also for correct estimation of interaction rates, energy losses etc.

In Chapter 2 we presented a brief overview of relativistic hydrodynamics of GRB paying special attention to the formulation of initial and boundary conditions. We also considered two mechanisms of spreading of relativistically expanding shell. Firstly, following the proposal of [33], we estimated hydrodynamical spreading of relativistically expanding shell. Secondly, we considered thermal spreading. Assuming relativistic Maxwellian distribution function for electrons and baryons we determined the velocity dispersion depending on the temperature and the Lorentz factor of the bulk motion. We then applied these results to GRBs and showed that thermal mechanism provides negligible spreading for realistic parameters of GRBs.

In Chapter 3 we computed the optical depth of relativistically moving medium and applied the results to GRB outflows. Starting from 4-dimensional invariant form of optical depth along the light ray, we showed by means of several

simple examples the appearance of different asymptotics in the optical depth of ultrarelativistically expanding outflows and introduced the notion of photon thick and photon thin outflows with different characteristic behavior of optical depth. This classification emerged from consideration of time evolution of ultrarelativistic outflow as it expands during the time, needed for a light ray to cross the outflow. Due to relativistic motion of the outflow this time is $2\Gamma^2$ times longer than crossing time for static shell of the same width. If the evolution of the outflow during this time is negligible, we referred the outflow to as photon thin, if it is substantial, we referred the outflow to as photon thick. It should be stressed that as a result of relativistic motion outflows are effectively "thickened", as crossing time is increasing.

Then we applied our results to GRB outflows and clarified the source of discrepancies existing in the literature about optical depth and transparency in GRBs. We showed that the association of “instantaneous energy release” with “thin shell” (e.g. [32, 33]) and “continuous energy release” with “thick wind” (e.g. [11, 27]) generally adopted in the literature is incomplete: at transparency shells can be “wind-like”, i.e. photon thick, and winds can be “shell-like”, i.e. photon thin. We found that all four asymptotics of optical depth and transparency radius derived in Sec. 3.8 are relevant for typical parameters of GRB both in shell and wind models, see Sections 3.9 and 3.10.

Based on these results, we proceeded in Chapter 4 to determine the observed characteristics of relativistically expanding initially optically thick plasma. We explore three levels of description of transparency. Firstly, determination of transparency radius (diffusion radius) of entire outflow characterizes the radius of emission of majority of photons. It also estimates the observed duration of photospheric emission in the photon thin case. Secondly, dynamics of transparency surface which crosses the outflow during its expansion, characterizes the instantaneous spectrum of the photospheric emission. Analysis of this dynamics is the basis of our sharp photosphere approximation. Thirdly, the probabilistic nature of the radiate transfer is accounted for by the probability of photon emission as function of radial position, angle and time. It also characterizes observed instantaneous spectrum of photospheric emission and it is the basis of our fuzzy photosphere approximation.

In Chapter 4 we proposed a unified treatment for transparency of ultrarelativistic outflows, which originate from finite wind and thin shell models of GRBs. We considered geometry of photospheres of ultrarelativistic outflows. As

we were interested in appearance of the photosphere to a distant observer, we introduced the notion of photospheric equitemporal surface and described its dynamics. We studied radiative diffusion in the relativistic outflows and found out that it is the main factor in photon decoupling from outflows, that are photon thin at transparency. We computed both energy flux and observed spectra of photon thick outflows in two approximations, derived from the radiative transfer equation. In our fuzzy photosphere approximation the effect of simultaneous emission from entire volume of the outflow is taken into account. We also used a simplier, but computationally less demanding sharp photosphere approximation which is shown to reproduces quite well both light curves and spectra. These results generalize the corresponding results in the literature for steady relativistic winds.

In photon thin outflows most of radiation was shown to originate not at its transparency radius, but at smaller radii due to radiation diffusion. Starting from the radiative transfer equation for time dependent outflows we derived the diffusion equation and obtained approximate analytic solution for the energy flux. We presented both instantaneous and time integrated observed spectra, the latter being well described by the Band function.

In Chapter 5 the equilibrium configurations of semidegenerate fermions with degenerate cores and nondegenerate halos were studied in General Relativity. Density and circular velocity profiles were obtained for these configurations and it was shown that they provide natural explanation for both central concentration of mass in galaxies and extended halos probed by rotational curves. It was found that in different ranges of radius the profiles of circular velocity coincide with phenomenological profiles of Dark Matter distributions, especially Einasto and Burkert ones.

Based on this analysis we conclude that DM distributions found in different galaxies and described by these phenomenological profiles can originate from semidegenerate fermion configurations as well. Observed discrepancy between radius and mass of the central object of our Galaxy and predictions of the model can be, in principle, accounted for by interaction of the particles and it is a subject of the future work.

Bibliography

[1] A. Cucchiara, A. J. Levan, D. B. Fox, N. R. Tanvir, T. N. Ukwatta, E. Berger, T. Krühler, A. Küpcü Yoldaş, X. F. Wu, K. Toma, J. Greiner, F. E. Olivares, A. Rowlinson, L. Amati, T. Sakamoto, K. Roth, A. Stephens, A. Fritz, J. P. U. Fynbo, J. Hjorth, D. Malesani, P. Jakobsson, K. Wiersema, P. T. O'Brien, A. M. Soderberg, R. J. Foley, A. S. Fruchter, J. Rhoads, R. E. Rutledge, B. P. Schmidt, M. A. Dopita, P. Podsiadlowski, R. Willingale, C. Wolf, S. R. Kulkarni, and P. D'Avanzo. A Photometric Redshift of $z \sim 9.4$ for GRB 090429B. *ApJ*, 736:7, July 2011.

[2] D. Christodoulou and R. Ruffini. Reversible Transformations of a Charged Black Hole. *Phys. Rev. D*, 4:3552–3555, December 1971.

[3] P. Meszaros. Gamma-ray bursts. *Reports of Progress in Physics*, 69:2259–2322, 2006.

[4] G.S. Bisnovatyi-Kogan. Cosmic gamma-ray bursts: Observations and modeling. *Physics of Particles and Nuclei*, 37:647–676, 2006.

[5] R. Ruffini, G.V. Vereshchagin, and S.-S. Xue. Electron-positron pairs in physics and astrophysics. *Physics Reports*, 487:1–140, 2010.

[6] M. Lyutikov. The electromagnetic model of gamma-ray bursts. *New Journal of Physics*, 8:119, July 2006.

[7] T. Piran. Gamma-ray bursts and the fireball model. *Phys. Rep.*, 314:575–667, June 1999.

[8] T. Piran. The physics of gamma-ray bursts. *Reviews of Modern Physics*, 76:1143–1210, October 2004.

[9] R. Ruffini, A. Aksenov, M. G. Bernardini, C. L. Bianco, L. Caito, M. G. Dainotti, G. de Barros, R. Guida, G. Vereshchagin, and S.-S. Xue. The canonical

Gamma-Ray Bursts: long, "fake"-"disguised" and "genuine" short bursts. In G. Giobbi, A. Tornambe, G. Raimondo, M. Limongi, L. A. Antonelli, N. Menci, & E. Brocato, editor, *American Institute of Physics Conference Series*, volume 1111 of *American Institute of Physics Conference Series*, pages 325–332, May 2009.

[10] J. Goodman. Are gamma-ray bursts optically thick? *ApJ*, 308:L47–L50, September 1986.

[11] B. Paczynski. Gamma-ray bursters at cosmological distances. *ApJ*, 308:L43–L46, September 1986.

[12] P. Mészáros, E. Ramirez-Ruiz, M. J. Rees, and B. Zhang. X-Ray-rich Gamma-Ray Bursts, Photospheres, and Variability. *ApJ*, 578:812–817, October 2002.

[13] R. Ruffini, C. L. Bianco, P. Chardonnet, F. Fraschetti, L. Vitagliano, and S. Xue. New perspectives in physics and astrophysics from the theoretical understanding of Gamma-Ray Bursts. In *AIP Conf. Proc. 668: Cosmology and Gravitation*, pages 16–107, June 2003.

[14] R. Ruffini, C. L. Bianco, S.-S. Xue, P. Chardonnet, F. Fraschetti, and V. Gurzadyan. On the Instantaneous Spectrum of Gamma-Ray Bursts. *International Journal of Modern Physics D*, 13:843–851, 2004.

[15] F. Ryde, M. Axelsson, B. B. Zhang, S. McGlynn, A. Pe'er, C. Lundman, S. Larsson, M. Battelino, B. Zhang, E. Bissaldi, J. Bregeon, M. S. Briggs, J. Chiang, F. de Palma, S. Guiriec, J. Larsson, F. Longo, S. McBreen, N. Omodei, V. Petrosian, R. Preece, and A. J. van der Horst. Identification and Properties of the Photospheric Emission in GRB090902B. *ApJ*, 709:L172–L177, February 2010.

[16] S. Guiriec, V. Connaughton, M. S. Briggs, M. Burgess, F. Ryde, F. Daigne, P. Mészáros, A. Goldstein, J. McEnery, N. Omodei, P. N. Bhat, E. Bissaldi, A. Camero-Arranz, V. Chaplin, R. Diehl, G. Fishman, S. Foley, M. Gibby, M. M. Giles, J. Greiner, D. Gruber, A. von Kienlin, M. Kippen, C. Kouveliotou, S. McBreen, C. A. Meegan, W. Paciesas, R. Preece, A. Rau, D. Tierney, A. J. van der Horst, and C. Wilson-Hodge. Detection of a Thermal Spectral Component in the Prompt Emission of GRB 100724B. *ApJ*, 727:L33, February 2011.

[17] J. Larsson, F. Ryde, C. Lundman, S. McGlynn, S. Larsson, M. Ohno, and K. Yamaoka. Spectral components in the bright, long GRB 061007: properties of the photosphere and the nature of the outflow. *MNRAS*, 414:2642–2649, July 2011.

[18] M. Axelsson, L. Baldini, G. Barbiellini, M. G. Baring, R. Bellazzini, J. Bregeon, M. Brigida, P. Bruel, R. Buehler, G. A. Caliandro, R. A. Cameron, P. A. Caraveo, C. Cecchi, R. C. G. Chaves, A. Chekhtman, J. Chiang, R. Claus, J. Conrad, S. Cutini, F. D'Ammando, F. de Palma, C. D. Dermer, E. d. C. e. Silva, P. S. Drell, C. Favuzzi, S. J. Fegan, E. C. Ferrara, W. B. Focke, Y. Fukazawa, P. Fusco, F. Gargano, D. Gasparrini, N. Gehrels, S. Germani, N. Giglietto, M. Giroletti, G. Godfrey, S. Guiriec, D. Hadasch, Y. Hanabata, M. Hayashida, X. Hou, S. Iyyani, M. S. Jackson, D. Kocevski, M. Kuss, J. Larsson, S. Larsson, F. Longo, F. Loparco, C. Lundman, M. N. Mazziotta, J. E. McEnery, T. Mizuno, M. E. Monzani, E. Moretti, A. Morselli, S. Murgia, E. Nuss, T. Nymark, M. Ohno, N. Omodei, M. Pesce-Rollins, F. Piron, G. Pivato, J. L. Racusin, S. Rainò, M. Razzano, S. Razzaque, A. Reimer, M. Roth, F. Ryde, D. A. Sanchez, C. Sgrò, E. J. Siskind, G. Spandre, P. Spinelli, M. Stamatikos, L. Tibaldo, M. Tinivella, T. L. Usher, J. Vandenbroucke, V. Vasileiou, G. Vianello, V. Vitale, A. P. Waite, B. L. Winer, K. S. Wood, J. M. Burgess, P. N. Bhat, E. Bissaldi, M. S. Briggs, V. Connaughton, G. Fishman, G. Fitzpatrick, S. Foley, D. Gruber, R. M. Kippen, C. Kouveliotou, P. Jenke, S. McBreen, S. McGlynn, C. Meegan, W. S. Paciesas, V. Pelassa, R. Preece, D. Tierney, A. von Kienlin, C. Wilson-Hodge, S. Xiong, and A. Pe'er. GRB110721A: An Extreme Peak Energy and Signatures of the Photosphere. *ApJ*, 757:L31, October 2012.

[19] S. Guiriec, F. Daigne, R. Hascoët, G. Vianello, F. Ryde, R. Mochkovitch, C. Kouveliotou, S. Xiong, P. N. Bhat, S. Foley, D. Gruber, J. M. Burgess, S. McGlynn, J. McEnery, and N. Gehrels. Evidence for a Photospheric Component in the Prompt Emission of the Short GRB 120323A and Its Effects on the GRB Hardness-Luminosity Relation. *ApJ*, 770:32, June 2013.

[20] P. Mészáros and M. J. Rees. Steep Slopes and Preferred Breaks in Gamma-Ray Burst Spectra: The Role of Photospheres and Comptonization. *ApJ*, 530:292–298, February 2000.

[21] M. J. Rees and P. Mészáros. Dissipative Photosphere Models of Gamma-Ray Bursts and X-Ray Flashes. *ApJ*, 628:847–852, August 2005.

[22] D. Giannios. Prompt emission spectra from the photosphere of a GRB. *A&A*, 457:763–770, October 2006.

[23] A. Pe'er. Temporal Evolution of Thermal Emission from Relativistically Expanding Plasma. *ApJ*, 682:463–473, July 2008.

[24] A. M. Beloborodov. Collisional mechanism for gamma-ray burst emission. *MNRAS*, 407:1033–1047, September 2010.

[25] A. M. Beloborodov. Radiative Transfer in Ultrarelativistic Outflows. *ApJ*, 737:68, August 2011.

[26] A. Pe'er and F. Ryde. A Theory of Multicolor Blackbody Emission from Relativistically Expanding Plasmas. *ApJ*, 732:49, May 2011.

[27] B. Paczynski. Super-Eddington winds from neutron stars. *ApJ*, 363:218–226, November 1990.

[28] A. G. Aksenov, R. Ruffini, and G. V. Vereshchagin. Thermalization of Nonequilibrium Electron-Positron-Photon Plasmas. *Phys. Rev. Lett.*, 99(12):125003, September 2007.

[29] A. G. Aksenov, R. Ruffini, and G. V. Vereshchagin. Thermalization of Electron-Positron-Photon Plasmas with an application to GRB. In *American Institute of Physics Conference Series*, volume 966 of *American Institute of Physics Conference Series*, pages 191–196, January 2008.

[30] A. G. Aksenov, R. Ruffini, and G. V. Vereshchagin. Thermalization of the mildly relativistic plasma. *Phys. Rev. D*, 79(4):043008, February 2009.

[31] A. G. Aksenov, R. Ruffini, and G. V. Vereshchagin. Pair plasma relaxation time scales. *Phys. Rev. E*, 81:046401, 2010.

[32] P. Mészáros, P. Laguna, and M. J. Rees. Gasdynamics of relativistically expanding gamma-ray burst sources - Kinematics, energetics, magnetic fields, and efficiency. *ApJ*, 415:181–190, September 1993.

[33] T. Piran, A. Shemi, and R. Narayan. Hydrodynamics of Relativistic Fireballs. *MNRAS*, 263:861–867, August 1993.

[34] F. Zwicky. Die Rotverschiebung von extragalaktischen Nebeln. *Helvetica Physica Acta*, 6:110–127, 1933.

[35] F. Zwicky. On the Masses of Nebulae and of Clusters of Nebulae. *ApJ*, 86:217, October 1937.

[36] G. S. Shostak. Aperture Synthesis Stady of Neutral Hydrogen in NGC 2403 and NGC 4236. II. Discussion. *A&A*, 24:411, May 1973.

[37] V. C. Rubin, W. K. J. Ford, and N. . Thonnard. Rotational properties of 21 SC galaxies with a large range of luminosities and radii, from NGC 4605 /R = 4kpc/ to UGC 2885 /R = 122 kpc/. *ApJ*, 238:471–487, June 1980.

[38] S. Dodelson. *Modern cosmology*. Amsterdam (Netherlands): Academic Press, 2003.

[39] R. Ruffini and L. Stella. On semi-degenerate equilibrium configurations of a collisionless self-gravitating Fermi gas. *A&A*, 119:35–41, March 1983.

[40] J. G. Gao, M. Merafina, and R. Ruffini. The semidegenerate configurations of a selfgravitating system of fermions. *A&A*, 235:1–7, August 1990.

[41] G. Ingrosso, M. Merafina, R. Ruffini, and F. Strafella. System of self-gravitating semidegenerate fermions with a cutoff of energy and angular momentum in their distribution function. *A&A*, 258:223–233, May 1992.

[42] F. Donato, G. Gentile, P. Salucci, C. Frigerio Martins, M. I. Wilkinson, G. Gilmore, E. K. Grebel, A. Koch, and R. Wyse. A constant dark matter halo surface density in galaxies. *MNRAS*, 397:1169–1176, August 2009.

[43] G. Gentile, B. Famaey, H. Zhao, and P. Salucci. Universality of galactic surface densities within one dark halo scale-length. *Nature*, 461:627–628, October 2009.

[44] Matthew G. Walker et al. A Universal Mass Profile for Dwarf Spheroidal Galaxies. *Astrophys. J.*, 704:1274–1287, 2009.

[45] M. G. Walker, S. S. McGaugh, M. Mateo, E. W. Olszewski, and R. Kuzio de Naray. Comparing the Dark Matter Halos of Spiral, Low Surface Brightness, and Dwarf Spheroidal Galaxies. *ApJ*, 717:L87–L91, July 2010.

[46] S. Weinberg. *Cosmology*. Oxford University Press, April 2008., April 2008.

[47] E. Gerstner. Laser physics: Lasing at the limit. *Nature Physics*, 6:638, September 2010.

[48] H. Chen, S. C. Wilks, J. D. Bonlie, E. P. Liang, J. Myatt, D. F. Price, D. D. Meyerhofer, and P. Beiersdorfer. Relativistic Positron Creation Using Ultraintense Short Pulse Lasers. *Phys. Rev. Lett.*, 102(10):105001, March 2009.

[49] J. Schwinger. On Gauge Invariance and Vacuum Polarization. *Phys. Rev.*, 82:664–679, June 1951.

[50] M. G. Mustafa and B. Kämpfer. Gamma flashes from relativistic electron-positron plasma droplets. *Phys. Rev. A*, 79(2):020103, February 2009.

[51] T. Damour and R. Ruffini. Quantum electrodynamical effects in Kerr-Newman geometries. *Phys. Rev. Lett.*, 35:463–466, August 1975.

[52] C. Alcock, E. Farhi, and A. Olinto. Strange stars. *ApJ*, 310:261–272, November 1986.

[53] V. V. Usov. Bare Quark Matter Surfaces of Strange Stars and e^+e^- Emission. *Phys. Rev. Lett.*, 80:230–233, January 1998.

[54] R. Belvedere, D. Pugliese, J. A. Rueda, R. Ruffini, and S.-S. Xue. Neutron star equilibrium configurations within a fully relativistic theory with strong, weak, electromagnetic, and gravitational interactions. *Nuclear Physics A*, 883:1–24, June 2012.

[55] R. P. Pilla and J. Shaham. Kinetics of Electron-Positron Pair Plasmas Using an Adaptive Monte Carlo Method. *ApJ*, 486:903, September 1997.

[56] R. J. Gould. Kinetic theory of relativistic plasmas. *Physics of Fluids*, 24:102–107, January 1981.

[57] S. Stepney. Two-body relaxation in relativistic thermal plasmas. *MNRAS*, 202:467–481, February 1983.

[58] E. A. Uehling and G. E. Uhlenbeck. Transport Phenomena in Einstein-Bose and Fermi-Dirac Gases. I. *Physical Review*, 43:552–561, April 1933.

[59] E. A. Uehling. Transport Phenomena in Einstein-Bose and Fermi-Dirac Gases. II. *Physical Review*, 46:917–929, November 1934.

[60] S.R. Groot, W.A. Leeuwen, and C.G. Weert. *Relativistic kinetic theory: principles and applications*. North-Holland Pub. Co., 1980.

[61] G. B. Rybicki and A. P. Lightman. *Radiative processes in astrophysics*. New York: Wiley-Interscience, 1979.

[62] R. Khatri, R. A. Sunyaev, and J. Chluba. Does Bose-Einstein condensation of CMB photons cancel μ distortions created by dissipation of sound waves in the early Universe? *A&A*, 540:A124, April 2012.

[63] L. D. Landau and E. M. Lifshitz. *Physical Kinetics*. Elsevier, 1st edition, 1981.

[64] V. B. Berestetskii, E. M. Lifshitz, and V. B. Pitaevskii. *Quantum Electrodynamics*. Elsevier, 2nd edition, 1982.

[65] J. Ehlers. Survey of general relativity theory. In *Relativity, Astrophysics and Cosmology*, pages 1–125, 1973.

[66] Jens Chluba. *Spectral Distortions of the Cosmic Microwave Background*. PhD thesis, Ludwig-Maximilians-Universität München, 2005.

[67] A. P. Lightman. Double Compton emission in radiation dominated thermal plasmas. *ApJ*, 244:392–405, March 1981.

[68] K. S. Thorne. Relativistic radiative transfer - Moment formalisms. *MNRAS*, 194:439–473, February 1981.

[69] L. D. Landau and E. M. Lifshits. *The Classical Theory of Fields*. Butterworth-Heinemann, 4th edition, 1994.

[70] J. M. Jauch and F. Rohrlich. *The theory of photons and electrons. The relativistic quantum field theory of charged particles with spin one-half*. Springer, New York, 1976.

[71] F. Mandl and T. H. R. Skyrme. The Theory of the Double Compton Effect. *Royal Society of London Proceedings Series A*, 215:497–507, December 1952.

[72] E. Haug and W. Nakel. *The Elementary Process of Bremsstrahlung*. World Scientific Publishing Co., Singapore, 2004.

[73] G. Hall and J. M. Watt. *Modern Numerical Methods for Ordinary Differential Equations*. New York, Oxford University Press, 1976.

[74] E. Costa, F. Frontera, J. Heise, M. Feroci, J. in't Zand, F. Fiore, M. N. Cinti, D. Dal Fiume, L. Nicastro, M. Orlandini, E. Palazzi, M. Rapisarda#, G. Zavattini, R. Jager, A. Parmar, A. Owens, S. Molendi, G. Cusumano, M. C. Maccarone, S. Giarrusso, A. Coletta, L. A. Antonelli, P. Giommi, J. M. Muller, L. Piro, and R. C. Butler. Discovery of an X-ray afterglow associated with the γ-ray burst of 28 February 1997. *Nature*, 387:783–785, June 1997.

[75] R. Ruffini, A. G. Aksenov, M. G. Bernardini, C. L. Bianco, L. Caito, P. Chardonnet, M. G. Dainotti, G. de Barros, R. Guida, L. Izzo, B. Patricelli, L. J. R. Lemos, M. Rotondo, J. A. R. Hernandez, G. Vereshchagin, and S.-S. Xue. The Blackholic energy and the canonical Gamma-Ray Burst IV: the "long," "genuine short" and "fake-disguised short" GRBs. In M. Novello and S. Perez, editors, *American Institute of Physics Conference Series*, volume 1132 of *American Institute of Physics Conference Series*, pages 199–266, May 2009.

[76] A. Pe'er, F. Ryde, R. A. M. J. Wijers, P. Mészáros, and M. J. Rees. A New Method of Determining the Initial Size and Lorentz Factor of Gamma-Ray Burst Fireballs Using a Thermal Emission Component. *ApJ*, 664:L1–L4, July 2007.

[77] R. Ruffini, L. Vitagliano, and S.-S. Xue. On a separatrix in the gravitational collapse to an overcritical electromagnetic black hole. *Physics Letters B*, 573:33–38, October 2003.

[78] R. Ruffini, J. D. Salmonson, J. R. Wilson, and S.-S. Xue. On the pair electromagnetic pulse of a black hole with electromagnetic structure. *A&A*, 350:334–343, October 1999.

[79] R. Ruffini, J. D. Salmonson, J. R. Wilson, and S.-S. Xue. On the pair-electromagnetic pulse from an electromagnetic black hole surrounded by a baryonic remnant. *A&A*, 359:855–864, July 2000.

[80] A. Shemi and T. Piran. The appearance of cosmic fireballs. *ApJ*, 365:L55–L58, December 1990.

[81] M. J. Rees and P. Meszaros. Unsteady outflow models for cosmological gamma-ray bursts. *ApJ*, 430:L93–L96, August 1994.

[82] R. Ruffini and G. Vereshchagin. Electron-positron plasma in GRBs and in cosmology. *Nuovo Cimento C*, 36:255, 2013.

[83] E. W. Kolb and M. S. Turner. *The Early Universe*. Frontiers in Physics, Reading, MA: Addison-Wesley, 1990.

[84] G. S. Bisnovatyi-Kogan and M. V. A. Murzina. Early stages of relativistic fireball expansion. *Phys. Rev. D*, 52:4380–4392, October 1995.

[85] O. M. Grimsrud and I. Wasserman. Non-equilibrium effects in steady relativistic $e^+ + e^-$-gamma winds. *MNRAS*, 300:1158–1180, November 1998.

[86] G. V. Vereshchagin. *Pair Plasma and Gamma Ray Bursts*. PhD thesis, Universitá di Roma "La Sapienza", 2008.

[87] F. Jüttner. Das Maxwellsche Gesetz der Geschwindigkeitsverteilung in der Relativtheorie. *Annalen der Physik*, 339:856–882, 1911.

[88] D. Mihalas and B. W. Mihalas. *Foundations of Radiation Hydrodynamics*. New York, Oxford University Press, 1984.

[89] R. Ruffini, I. A. Siutsou, and G. V. Vereshchagin. A Theory of Photospheric Emission from Relativistic Outflows. *ApJ*, 772:11, July 2013.

[90] W. Rindler. *Relativity: special, general, and cosmological*. Oxford, UK: Oxford University Press, 2001.

[91] R. Ruffini, I.A. Siutsou, and G.V. Vereshchagin. Spreading of ultrarelativistically expanding shell: an application to {GRBs}. *New Astronomy*, 2013.

[92] C. Li and R. Sari. Analytical Solutions for Expanding Fireballs. *ApJ*, 677:425–431, April 2008.

[93] K. Toma, X.-F. Wu, and P. Mészáros. Photosphere-internal shock model of gamma-ray bursts: case studies of Fermi/LAT bursts. *MNRAS*, 415:1663–1680, August 2011.

[94] M. A. Abramowicz, I. D. Novikov, and B. Paczynski. The appearance of highly relativistic, spherically symmetric stellar winds. *ApJ*, 369:175–178, March 1991.

[95] C. Thompson. A Model of Gamma-Ray Bursts. *MNRAS*, 270:480, October 1994.

[96] F. Daigne and R. Mochkovitch. The expected thermal precursors of gamma-ray bursts in the internal shock model. *MNRAS*, 336:1271–1280, November 2002.

[97] S. Iwamoto and F. Takahara. Relativistic Outflow of Electron-Positron Pair Plasma from a Wien Equilibrium State. *ApJ*, 565:163–173, January 2002.

[98] E. Nakar, T. Piran, and R. Sari. Pure and Loaded Fireballs in Soft Gamma-Ray Repeater Giant Flares. *ApJ*, 635:516–521, December 2005.

[99] M. G. Bernardini, C. L. Bianco, L. Caito, M. G. Dainotti, R. Guida, and R. Ruffini. GRB 970228 and a class of GRBs with an initial spikelike emission. *A&A*, 474:L13–L16, October 2007.

[100] R. Ruffini, C. L. Bianco, F. Fraschetti, S.-S. Xue, and P. Chardonnet. On the Interpretation of the Burst Structure of Gamma-Ray Bursts. *ApJ*, 555:L113–L116, July 2001.

[101] R. Ruffini, M. G. Bernardini, C. L. Bianco, P. Chardonnet, F. Fraschetti, R. Guida, and S.-S. Xue. GRB 050315: A Step toward Understanding the Uniqueness of the Overall Gamma-Ray Burst Structure. *ApJ*, 645:L109–L112, July 2006.

[102] M. G. Bernardini, C. L. Bianco, L. Caito, L. Izzo, B. Patricelli, and R. Ruffini. The X-Ray Flares of GRB 060607A within the Fireshell Model. In *Twelfth Marcel Grossmann Meeting on General Relativity*, page 1600, 2012.

[103] L. Izzo, R. Ruffini, A. V. Penacchioni, C. L. Bianco, L. Caito, S. K. Chakrabarti, J. A. Rueda, A. Nandi, and B. Patricelli. A double component in GRB 090618: a proto-black hole and a genuinely long gamma-ray burst. *A&A*, 543:A10, July 2012.

[104] M. G. Dainotti, M. G. Bernardini, C. L. Bianco, L. Caito, R. Guida, and R. Ruffini. GRB 060218 and GRBs associated with supernovae Ib/c. *A&A*, 471:L29–L32, August 2007.

[105] M. G. Bernardini, C. L. Bianco, P. Chardonnet, F. Fraschetti, R. Ruffini, and S.-S. Xue. Theoretical Interpretation of the Luminosity and Spectral Properties of GRB 031203. *ApJ*, 634:L29–L32, November 2005.

[106] L. Caito, M. G. Bernardini, C. L. Bianco, M. G. Dainotti, R. Guida, and R. Ruffini. GRB060614: a "fake" short GRB from a merging binary system. *A&A*, 498:501–507, May 2009.

[107] L. Izzo, M. Grazia Bernardini, C. Luciano Bianco, L. Caito, B. Patricelli, and R. Ruffini. GRB 090423 at Redshift 8.1: a Theoretical Interpretation. *Journal of Korean Physical Society*, 57:551, September 2010.

[108] L. Izzo, M. G. Bernardini, C. L. Bianco, L. Caito, B. Patricelli, and R. Ruffini. GRB 090423 in the Fireshell Scenario: A Canonical GRB at Redshift 8.2. In *Twelfth Marcel Grossmann Meeting on General Relativity*, page 1610, 2012.

[109] G. de Barros, L. Amati, M. G. Bernardini, C. L. Bianco, L. Caito, L. Izzo, B. Patricelli, and R. Ruffini. On the nature of GRB 050509b: a disguised short GRB. *A&A*, 529:A130, May 2011.

[110] L. Caito, L. Amati, M. G. Bernardini, C. L. Bianco, G. de Barros, L. Izzo, B. Patricelli, and R. Ruffini. GRB 071227: an additional case of a disguised short burst. *A&A*, 521:A80, October 2010.

[111] L. Caito, M. G. Bernardini, C. L. Bianco, L. Izzo, B. Patricelli, and R. Ruffini. GRB 071227:. another Disguised Short Burst. *International Journal of Modern Physics D*, 20:1931–1935, 2011.

[112] B. Patricelli, M. G. Bernardini, C. L. Bianco, L. Caito, G. de Barros, L. Izzo, R. Ruffini, and G. V. Vereshchagin. Analysis of GRB 080319B and GRB 050904 within the Fireshell Model: Evidence for a Broader Spectral Energy Distribution. *ApJ*, 756:16, September 2012.

[113] A. V. Penacchioni, R. Ruffini, L. Izzo, M. Muccino, C. L. Bianco, L. Caito, B. Patricelli, and L. Amati. Evidence for a proto-black hole and a double astrophysical component in GRB 101023. *A&A*, 538:A58, February 2012.

[114] C. L. Bianco, R. Ruffini, and S.-S. Xue. The elementary spike produced by a pure e^+e^- pair-electromagnetic pulse from a Black Hole: The PEM Pulse. *A&A*, 368:377–390, March 2001.

[115] G. Preparata, R. Ruffini, and S.-S. Xue. The role of the screen factor in GRBs. *Nuovo Cimento B Serie*, 115:915, July 2000.

[116] R. Ruffini, F. Fraschetti, L. Vitagliano, and S.-S. Xue. Observational Signatures of An Electromagnetic Overcritical Gravitational Collapse. *International Journal of Modern Physics D*, 14:131–141, 2005.

[117] F. Fraschetti, R. Ruffini, L. Vitagliano, and S. S. Xue. Theoretical predictions of spectral evolution of short GRBs. *Nuovo Cimento B Serie*, 121:1477–1478, December 2006.

[118] F. Ryde. The Cooling Behavior of Thermal Pulses in Gamma-Ray Bursts. *ApJ*, 614:827–846, October 2004.

[119] F. Ryde and A. Pe'er. Quasi-blackbody Component and Radiative Efficiency of the Prompt Emission of Gamma-ray Bursts. *ApJ*, 702:1211–1229, September 2009.

[120] P. Couderc. Les aureoles lumineuses des Novaelig. *Annales d'Astrophysique*, 2:271, January 1939.

[121] M. J. Rees. Appearance of Relativistically Expanding Radio Sources. *Nature*, 211:468–470, July 1966.

[122] M. J. Rees. Studies in radio source structure-I. A relativistically expanding model for variable quasi-stellar radio sources. *MNRAS*, 135:345, 1967.

[123] R. C. Haskell, L. O. Svaasand, T.-T. Tsay, T.-C. Feng, M. S. McAdams, and B. J. Tromberg. Boundary conditions for the diffusion equation in radiative transfer. *Journal of the Optical Society of America A*, 11:2727–2741, October 1994.

[124] S. I. Blinnikov, A. V. Kozyreva, and I. E. Panchenko. Gamma-ray bursts: When does a blackbody spectrum look non-thermal? *Astronomy Reports*, 43:739–747, November 1999.

[125] F. Ryde, A. Pe'Er, T. Nymark, M. Axelsson, E. Moretti, C. Lundman, M. Battelino, E. Bissaldi, J. Chiang, M. S. Jackson, S. Larsson, F. Longo, S. McGlynn, and N. Omodei. Observational evidence of dissipative photospheres in gamma-ray bursts. *MNRAS*, 415:3693–3705, August 2011.

[126] D. Bégué, I. A. Siutsou, and G. V. Vereshchagin. Monte Carlo Simulations of the Photospheric Emission in Gamma-Ray Bursts. *ApJ*, 767:139, April 2013.

[127] S. S. Gershtein and Y. B. Zel'Dovich. Rest Mass of Muonic Neutrino and Cosmology. *Soviet Journal of Experimental and Theoretical Physics Letters*, 4:120, September 1966.

[128] S. Tremaine and J. E. Gunn. Dynamical role of light neutral leptons in cosmology. *Phys. Rev. Lett.*, 42:407–410, February 1979.

[129] G. W. Angus. A lower limit on the dark particle mass from dSphs. *J. Cosmology Astropart. Phys.*, 3:26, March 2010.

[130] E. Giusarma, M. Corsi, M. Archidiacono, R. de Putter, A. Melchiorri, O. Mena, and S. Pandolfi. Constraints on massive sterile neutrino species from current and future cosmological data. *Phys. Rev. D*, 83(11):115023, June 2011.

[131] B. W. Lee and S. Weinberg. Cosmological lower bound on heavy-neutrino masses. *Phys. Rev. Lett.*, 39:165–168, July 1977.

[132] E. Polisensky and M. Ricotti. Constraints on the dark matter particle mass from the number of Milky Way satellites. *Phys. Rev. D*, 83(4):043506, February 2011.

[133] C. J. Hogan and J. J. Dalcanton. New dark matter physics: Clues from halo structure. *Phys. Rev. D*, 62(6):063511, September 2000.

[134] H. J. de Vega and N. G. Sanchez. Model-independent analysis of dark matter points to a particle mass at the keV scale. *MNRAS*, 404:885–894, May 2010.

[135] J. F. Navarro, C. S. Frenk, and S. D. M. White. A Universal Density Profile from Hierarchical Clustering. *ApJ*, 490:493, December 1997.

[136] J. Einasto. Kinematics and dynamics of stellar systems. In *Trudy Inst. Astrofiz.*, volume 5, page 87. Alma-Ata, 1965.

[137] A. Burkert. The Structure of Dark Matter Halos in Dwarf Galaxies. *ApJ*, 447:L25, July 1995.

[138] A. Boyarsky, O. Ruchayskiy, D. Iakubovskyi, A. V. Maccio', and D. Malyshev. New evidence for dark matter. *ArXiv e-prints, astro-ph.CO/0911.1774*, November 2009.

[139] P. Salucci, C. Frigerio Martins, and A. Lapi. DMAW 2010 LEGACY the Presentation Review: Dark Matter in Galaxies with its Explanatory Notes. *ArXiv e-prints, astro-ph.CO/1102.1184*, February 2011.

[140] B. M. Peterson. Toward Precision Measurement of Central Black Hole Masses. In *IAU Symposium*, volume 267 of *IAU Symposium*, pages 151–160, May 2010.

[141] M. Vestergaard. Determining Central Black Hole Masses in Distant Active Galaxies. *ApJ*, 571:733–752, June 2002.

[142] M. Vestergaard and B. M. Peterson. Determining Central Black Hole Masses in Distant Active Galaxies and Quasars. II. Improved Optical and UV Scaling Relationships. *ApJ*, 641:689–709, April 2006.

[143] T. A. Targett, J. S. Dunlop, and R. J. McLure. The host galaxies and black hole-to-galaxy mass ratios of luminous quasars at $z \sim 4$. *MNRAS*, 420:3621–3631, March 2012.

[144] R. D. Viollier, D. Trautmann, and G. B. Tupper. Supermassive neutrino stars and galactic nuclei. *Physics Letters B*, 306:79–85, May 1993.

[145] C. Argüelles, I. Siutsou, R. Ruffini, J. Rueda, and B. Machado. On the core-halo constituents of a semi-degenerate gas of massive fermions. In *Probes of Dark Matter on Galaxy Scales*, page 30204, July 2013.

[146] J. A. Rueda, R. Ruffini, and S.-S. Xue. The Klein first integrals in an equilibrium system with electromagnetic, weak, strong and gravitational interactions. *Nuclear Physics A*, 872:286–295, December 2011.

[147] J. F. Navarro, A. Ludlow, V. Springel, J. Wang, M. Vogelsberger, S. D. M. White, A. Jenkins, C. S. Frenk, and A. Helmi. The diversity and similarity of simulated cold dark matter haloes. *MNRAS*, 402:21–34, February 2010.

[148] G. Gentile, P. Salucci, U. Klein, D. Vergani, and P. Kalberla. The cored distribution of dark matter in spiral galaxies. *MNRAS*, 351:903–922, July 2004.

[149] J. Binney and S. Tremaine. *Galactic dynamics*. Princeton, NJ, Princeton University Press, 1987.

[150] G. Narain, J. Schaffner-Bielich, and I. N. Mishustin. Compact stars made of fermionic dark matter. *Phys. Rev. D*, 74(6):063003, September 2006.

[151] A. M. Ghez, S. Salim, N. N. Weinberg, J. R. Lu, T. Do, J. K. Dunn, K. Matthews, M. R. Morris, S. Yelda, E. E. Becklin, T. Kremenek, M. Milosavljevic, and J. Naiman. Measuring Distance and Properties of the Milky Way's Central Supermassive Black Hole with Stellar Orbits. *ApJ*, 689:1044–1062, December 2008.

[152] S. Gillessen, F. Eisenhauer, T. K. Fritz, H. Bartko, K. Dodds-Eden, O. Pfuhl, T. Ott, and R. Genzel. The Orbit of the Star S2 Around SGR A* from Very Large Telescope and Keck Data. *ApJ*, 707:L114–L117, December 2009.

[153] R. Scarpa, G. Marconi, G. Carraro, R. Falomo, and S. Villanova. Testing Newtonian gravity with distant globular clusters: NGC 1851 and NGC 1904. *A&A*, 525:A148, January 2011.